2015

Chemically Patterned Surfaces as Test Platforms to Study Magnetic and Solvent-Responsive Properties at the Nanoscale: Investigations Using Scanning Probe Microscopy

Shalaka Kulkarni
Louisiana State University and Agricultural and Mechanical College, shalskulz@gmail.com

CHEMICALLY PATTERNED SURFACES AS TEST PLATFORMS TO STUDY MAGNETIC AND SOLVENT-RESPONSIVE PROPERTIES AT THE NANOSCALE: INVESTIGATIONS USING SCANNING PROBE MICROSCOPY

A Dissertation

Submitted to the Graduate Faculty of the
Louisiana State University and
Agricultural and Mechanical College
in partial fulfillment of the
requirements for the degree of
Doctor of Philosophy

in

The Department of Chemistry

by
Shalaka Amit Kulkarni
B.S., University of Mumbai, 1999
M.S., University of Mumbai, 2001
December 2015

ACKNOWLEDGMENTS

First, I would like to thank my advisor, Dr. Jayne C. Garno, for her unstinting support throughout my life here at LSU. Her constant support, guidance, very calm and caring nature has helped me overcome all the difficulties we face as a naïve researcher. She has helped me sail smoothly through the rough waters of graduate student life. I would also sincerely like to thank Dr. Graca Vicente, Dr. Donghui Zhang and Dr. Brent Christner for their willingness to serve on my committee. I would like to thank both past and present colleagues in the Garno research group. I sincerely cherish all the moments we shared together as colleagues and friends be it group lunches, achievement parties, baby showers, grad walks, and constructive group meetings.

I'm also grateful to all my friends who made my life at LSU a very memorable one. I can never forget the weekend potlucks enjoying different cuisines, playing carrom, cards, going out for canoeing, celebrating birthdays, festivals, individual achievements etc.

Special thanks to Dr. Sreelatha Balamurugan and Dr. Bala Subramanian, without their motivation and support, I would never have stepped into LSU Chemistry program. I thank them both from the bottom of my heart.

Last but not the least, I am immensely indebted to my family for their rock solid support in all my endeavors. My dad, mom, brother, sister-in-law, my 'two' mother-in laws, and my beloved husband gave me confidence and encouragement in every hurdle and struggle I faced, to keep my spirits high. It was my dad's dream that his daughter should gain education in this wonderful land of opportunities. Your love and support have led me to where I am today. Mom, you are the strongest woman I have ever met. I always look up to you as my role model and thank you for always standing behind me. You've always been there for me, and I can't tell you how much I love you. Dad and now bro, you both have always inspired me to never give up, believe

in my abilities and keep walking. Your invaluable words of wisdom give me strength to overcome all the difficulties. My strong and caring husband, (aka problem solver) who has always taken the brunt of my troubles and helped me come out of them with his unwavering support. I also thank my wonderful princess who has learnt to stay happy and adjust in all the situations. All of your sacrifices have not gone unnoticed, and I want to acknowledge and thank you for allowing me to achieve my dreams. Love them all.

TABLE OF CONTENTS

LIST OF TABLES

LIST OF FIGURES

LIST OF ABBREVIATIONS

ABBREVIATION	NAME
AFM	Atomic force microscopy
AC-AFM	Alternating contact atomic force microscopy
MAC mode	Magnetic AC mode
MSM-AFM	Magnetic sample modulation atomic force microscopy
MRAM	Magnetic random access memory
NSL	Nanosphere lithography
OTS	Octadecyltrichlorosilane
PEG	2-[Methoxy-(polyethyleneoxy)propyl] trichlorosilane
SAM	Self-assembled monolayer
SEM	Scanning electron microscopy
SPM	Scanning probe microscopy
STM	Scanning tunneling microscopy
TEM	Transmission electron microscopy
TM-AFM	Tapping mode Atomic force microscopy
UTS	10-Undecenyltrichlorosilane
XRD	X-ray diffraction

ABSTRACT

Chemically patterned surfaces were fabricated using a combination of molecular self-assembly and particle lithography to generate billions of nanostructures of organosilane self-assembled monolayers (SAMs). Monodisperse mesospheres were used as surface masks to prepare nanostructures on flat surfaces using the simple benchtop chemistry steps of mixing, centrifuging, evaporation, and drying. Periodic arrays of well-defined organosilane nanostructures serve as discrete surface sites for the selective deposition of polymers and magnetic nanoparticles.

In this dissertation, particle lithography approaches for surface patterning provide new directions for studying surface chemistry at the molecular-level using high resolution investigations with scanning probe microscopy (SPM). Atomic force microscopy (AFM) can be used to analyze samples in ambient and liquid environments. The solvent responsive nature of OTS nanostructures were investigated using *in-situ* liquid imaging with AFM. AFM provides unique capabilities for molecular visualization and ultrasensitive measurements of changes in heights, widths and surface coverage of the swollen OTS nanostructures with nanoscale resolution. Ring nanostructures of OTS presented a 3D interface for studying the interaction of solvents at the molecular level.

The vibrational response of patterned magnetic Fe_3O_4 nanoparticles in response to an applied external magnetic field was detected using magnetic sample modulation AFM (MSM-AFM). The vibration of Fe_3O_4 nanoparticles can be detected with a nonmagnetic AFM tip operated in continuous contact mode. In MSM-AFM, an AC current applied to the wire coil solenoid within the special sample plate drives the actuation of magnetic nanomaterials that are attached to surfaces. The magnetic Fe_3O_4 nanoparticles were induced to vibrate in the presence of externally applied electromagnetic field. Parameters such as frequency and magnetic field strength can be

tuned *in-situ* to study dynamic changes in the vibrational response of samples. The AFM tip serves as a force and motion sensor for mapping the vibrational response of magnetic nanomaterials. The information acquired from MSM images includes the distribution of individual magnetic domains as well as spectra of the characteristic resonance frequencies of the vibrating magnetic nanomaterials.

CHAPTER 1: INTRODUCTION

The drive for miniaturization of devices has resulted in focused efforts for developing technologies for manufacturing at the nanoscale.[1,2] In addition, unique phenomena have been revealed at the nanoscale for certain materials which are distinct from the bulk properties. Properties at the nanometer scale often cannot be described with the laws of classical mechanics, but instead, follow the rules of quantum mechanics. A fundamental challenge for nanofabrication is to engineer surfaces with specific surface chemistry in addition to controlling the distribution of chemical functional groups.[3, 4 ,5]

Particle lithography, also known as nanosphere lithography (NSL), or colloidal lithography can be applied to manufacture one, two and three dimensional nanostructures. Particle lithography offers advantages of being inexpensive, easy to implement, requires relatively simple bench chemistry protocols, with high throughput. The fabrication of nanostructures on planar surfaces also provides possibilities for the investigation of size-dependent properties of nanomaterials.[6,7,8] Nanostructures have potential applications in sensors,[9,10] catalysis,[11] molecular separation,[12] and electronic devices.[13] This dissertation describes nanoscale fabrication methods that combine particle lithography with molecular self-assembly to prepare spatially selective surface structures. With particle lithography, the density, surface coverage, sizes and spacing between the nanopatterns can be controlled by selecting the diameter of mesospheres used as surface masks. The arrays of nanopatterns serve as well-defined test platforms for fundamental investigations of changes in properties at the molecular level using advanced imaging modes of atomic force microscopy (AFM).

1.1 Nanoscale Studies Using Scanning Probe Microscopy (SPM)

The main application of AFM is for high resolution imaging of nanomaterials and surfaces including metals,[14] polymers,[15] biomolecules such as DNA,[16,17] RNA,[18] proteins,[19] and cells.[20] Studies with AFM span over a range of interdisciplinary fields such as biophysics,[21] chemistry,[22,23] biology,[24,25] life sciences, polymer science,[26] material science,[27] biomedical engineering, nanotechnology, biotechnology, molecular electronics.[28] Chapter 2 includes a brief history of SPM as well as the operating principles of the measurement modes used in this dissertation. The sample preparation of surface test platforms using particle lithography for AFM studies is also summarized in Chapter 2.

1.2 Solvent Responsive Behavior of Octadecyltrichlorosilane (OTS) Multilayers

An emerging challenge for nanoscale measurements is to capture and quantify the magnitude of structural changes in response to environmental changes. Certain environmental parameters can affect the nanoscale morphology of samples, such as changing the pH, solvent polarity, ionic strength, and temperature. We prepared test platforms of *n*-octadecyltrichlorosilane (OTS) ring nanostructures to study surface morphology changes at the nanoscale in selected liquid media compared to dry conditions in air. Particle lithography combined with organosilane vapor deposition was used to fabricate nanostructures of regular dimensions. Multilayer nanostructures of OTS were used as a test platform for scanning probe studies of solvent-responsive properties where the sides of designed ring structures expose a 3D interface for studying the interaction of solvents with molecular side groups. In dry, ambient conditions, nanostructures of OTS were first imaged using contact mode atomic force microscopy (AFM). Next, ethanol or buffer was introduced to the sample cell, and images were acquired using the same probe. We observed substantial changes in the lateral and vertical dimensions of the ring nanostructures in AFM

topography frames; the sizes of the rings were observed to swell by tens of nanometers. Even after heat treatment of samples to promote cross-linking, the samples still evidenced swelling in liquid media. This research will have consequences for studies of the properties of nanomaterials, such as solvent-responsive organic films and polymers.

In Chapter 3, ring nanostructures of octadecyltrichlorosilane (OTS) were prepared on Si(111) surfaces using designed protocols of particle lithography combined with vapor deposition. Liquid imaging with AFM enabled *in-situ* investigations of the solvent responsive nature of OTS nanostructures. The OTS nanorings furnish a robust surface platform that can sustain multiple successive measurements with scanning probe microscopy. Ring nanostructures of OTS presented a 3D interface for studying the interaction of solvents at the molecular level. Nanoscale details of the swollen structures were quantified for the first time, with respect to differences in height, width and surface coverage under confined dimensions of OTS ring nanopatterns.

1.3 Dynamic Studies of the Vibrational Response of Iron Oxide Nanoparticles Using Magnetic Sample Modulation (MSM-AFM)

Properties and size-dependent effects of magnetic nanoparticles can be studied using magnetic measurement modes of atomic force microscopy (AFM). Particle lithography was used to produce arrays of nanostructures on flat surfaces using a few basic steps. Monodisperse mesospheres were used as a surface mask to guide the deposition of magnetic nanoparticles. With a mixture approach of "two-particle" lithography, 2D arrays of nanopatterns were generated yielding control over the surface coverage, size, and periodicity of samples. Magnetic sample modulation (MSM-AFM) was used to detect the vibration of patterned Fe_3O_4 nanoparticles in response to an applied external electromagnetic field. The vibration of Fe_3O_4 nanoparticles was detected by a nonmagnetic AFM tip to map changes in the frequency and amplitude of the vibrating

samples. The nonmagnetic AFM tip serves as a motion sensor for mapping the vibrational response of magnetic nanomaterials at the level of individual Fe_3O_4 clusters and nanoparticles.

Experimental results for magnetic mapping of the iron oxide nanoparticle clusters using magnetic sample modulation AFM (MSM-AFM) will be presented in Chapter 4. The hybrid imaging and measurement mode of MSM-AFM uses a MAC-mode sample plate to actuate the magnetic nanoparticles. An AC current is applied to the wire coil solenoid within the MAC-mode sample plate to drive the actuation of magnetic nanomaterials that are attached to surfaces. The AFM tip is used to detect the sample vibration. Instead of using a magnetically coated AFM probe as a magnetic sensor, MSM requires a non-magnetic probe for contact mode AFM to characterize the vibration of ferromagnetic nanoparticles responding to the flux of an AC electromagnetic field. The feedback for MSM-AFM is configured for contact mode imaging, and the probe is scanned slowly across the vibrating samples. Parameters such as frequency and magnetic field strength can be tuned *in-situ* to study dynamic changes in the vibrational response of samples.

Studies with the MSM mode reveal how the composition and size of nanoparticles affects the vibration in response to a magnetic field. The MSM imaging mode provides characterizations at the level of individual nanoparticles for detecting changes in vibrational resonance signatures in response to an AC electromagnetic flux, as well as revealing differences in vibration amplitude versus the strength of magnetic field.

1.4 Synopsis

Particle lithography combined with the self-assembly of organosilanes was used to generate nanostructures with designed interfaces and sizes. The surface arrays demonstrated in this dissertation include nanopatterned surfaces of OTS multilayer assemblies and nanoscale arrays of

magnetic iron oxide nanoparticle clusters. A conclusion summary and future prospectus for the research experiments of this dissertation are presented in Chapter 5.

CHAPTER 2: EXPERIMENTAL APPROACH WITH ATOMIC FORCE MICROSCOPY

2.1 History of Atomic Force Microscopy

During the 1980s the field of surface science was revolutionized by the invention of the scanning tunneling microscope,[29] (STM) and the atomic force microscope (AFM).[30] The AFM was invented in 1986 by Gerd Binnig, Calvin Quate, and Christopher Gerber.[30] Since then it has become a powerful, widely used and versatile tool for the nanoscale imaging of surfaces[15, 31, 32, 33, 34] and for the measurement of intermolecular and surface forces.[35,36,37,38,39,40,41] The visualization of individual atoms and atomic vacancies within an atomic lattice was achieved with STM for the first time by Binnig and Rohrer.[29, 42] Today, STM is used routinely to image surfaces with atomic and molecular resolution,[43, 44] however, STM has the inherent limitation of the requirement of surfaces to be atomically flat and conductive. The development of AFM overcomes the limitation of requiring that surfaces be conductive and has contributed to the study of diverse samples such as imaging non-conductive or insulating materials, in addition to chemical and biological systems. Experiments with AFM can be accomplished under ambient conditions and in liquids.

An advantage of AFM is that the samples can be probed in air, vacuum and liquid with capabilities for dynamic studies to monitor changes in surface morphology that evolve over time using time-lapse AFM. The resolution achieved with AFM is 0.1 nm for the x and y directions (depending on tip radius), and 0.01 nm in the z direction.[24, 45] AFM images contain 3D information about the sample surface, whereas SEM and TEM provide 2D maps of sample surface morphology. Thus, AFM has become a valuable tool for interdisciplinary research efforts, in chemistry, physics, engineering,[46] life sciences,[47] materials science, electrochemistry, polymer science,[48] biophysics, nanotechnology and biotechnology.[24]

2.2 Imaging Principle of Atomic Force Microscopy

Achieving high resolution images with AFM requires an ultrasharp tip attached to a flexible V-shaped or rectangular cantilever. The cantilevers typically have lengths ranging from 10-200 μm and widths of 20-40 μm. Probes for AFM measurements are usually made of silicon (Si) or silicon nitride (Si_3N_4) and typically have a diameter less than 30 nm.[49] The geometries of the apex of the tips are usually square-based pyramids or cylindrical cones. Tips may be composed of diamond and other conducting or semi-conducting materials depending on the operating mode of AFM to be used. For high resolution imaging of individual proteins, tips made up of carbon nanotubes with diameters around 2 nm are used for tapping mode.[50] Tips are chosen based on the type of sample and the nature of the tip-sample interaction under investigation. Tips for AFM have specific shapes, spring constants, and composition depending on the selected measurement mode.

The AFM tip is used to record and map the interaction between the probe and sample surface as it is scanned over the surface. The main forces contributing to the cantilever deflection include (Coulomb) electrostatic repulsive forces and attractive and van der Waals forces between the atoms within the tip and the atoms of the sample surface. In conventional AFM operational modes, a tip located at the end of a cantilever is either scanned over the surface in permanent contact, non-contact, or is driven to vibrate to gently tap the sample. Key components for an AFM are a microfabricated tip and a tube shaped piezoelectric scanner. High resolution images are attained when an ultrasharp AFM tip attached to a flexible cantilever and accurate ceramic piezoelements enable the sample to be scanned in the x-y direction with sub-nanometer precision. Piezoelectric materials used to fabricate AFM piezoscanners include barium titanate and lead zirconate titanate which expand and contract when a potential is applied. The scanner converts electric signals from AFM control electronics into mechanical scanning motion in the lateral

direction of the sample. AFM images are also affected by a number of nonlinear properties that are inherent to piezoelectric material, including hysteresis, creep, and drift.[51] The set-up for AFM is shown in Figure 2.1.

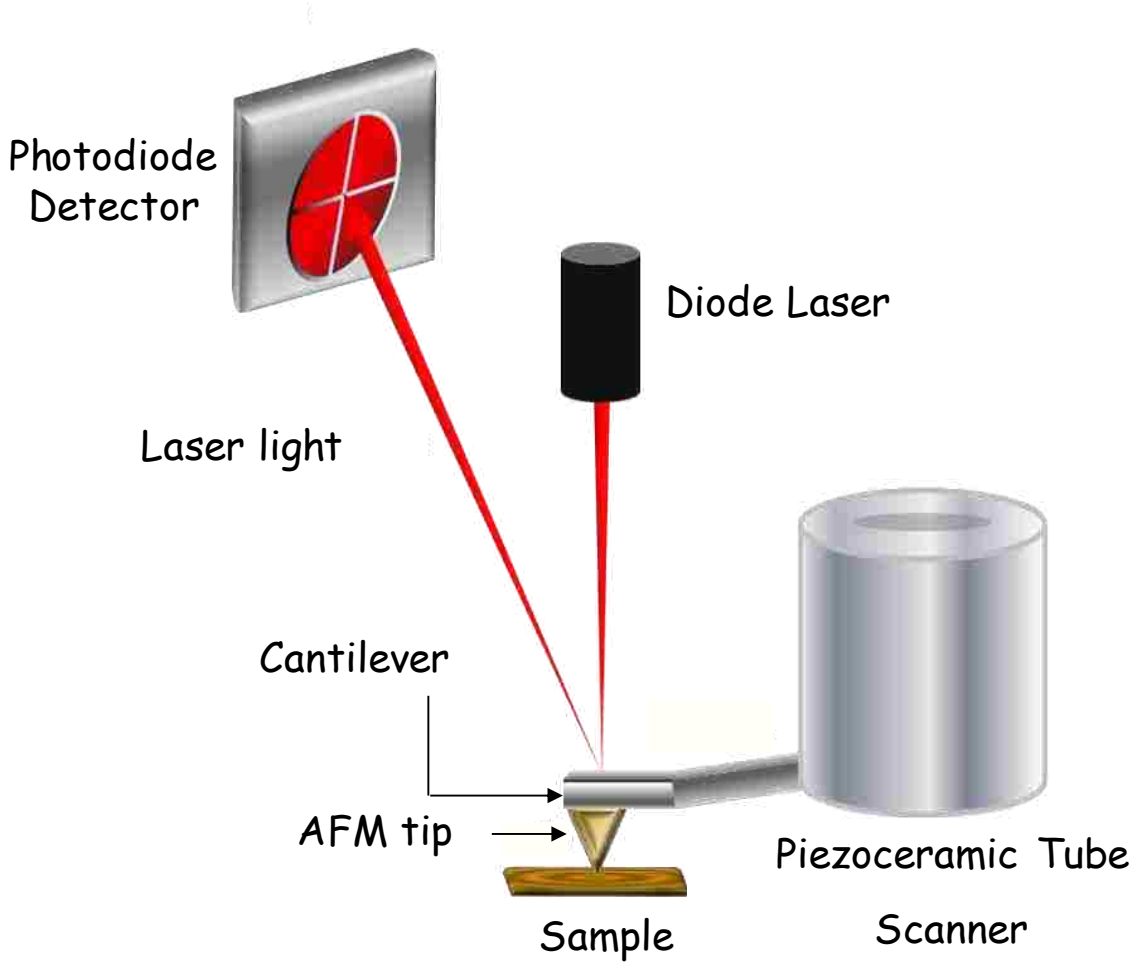

Figure 2.1 Instrumental set-up for an atomic force microscope

Piezoscanners should be regularly calibrated every few months for reliable spatial measurements with AFM. The piezoceramic tube scanner consists of several piezoelectric elements to move the probe along the x, y, and z directions.[52] To calibrate the scanner, a calibration grating NT-MDT TGQ1 with a 20-nm feature height and a 3-μm period was used as an imaging sample in contact mode AFM and the sample was scanned using the constant-force as the feedback

control. A regular contact mode AFM probe with a nominal spring constant of 0.2 N/m and resonance frequency of 13 kHz was used for raster scanning. A raster scan was attained by applying a triangular waveform to the x-axis (fast axis) and a very slow ramp signal to the y-axis (slow axis) of the scanner. In the z direction, a feedback loop is used to control the voltage applied to the z electrode. As the tip is scanned across the surface, feedback system feeds a voltage to the z electrode to maintain constant force between the tip and sample. The use of feedback controllers in damping and linearizing the piezoelectric tube scanner has been shown to be successful in attaining fairly faithful AFM images.

For imaging with AFM, a red diode laser (670 nm) beam focused on the back of the cantilever is reflected to the four quadrant position sensitive photodiode detector. As the tip is scanned in a raster pattern across the sample in a line-by-line fashion, changes in deflection or oscillation amplitude of the tip are monitored and detected in the position sensitive photodetector. Digital AFM images are a convolution of the geometry of the sample and tip. Lateral resolution of the AFM image depends on the dimensions of the tip, wider probes produce broader features.[53, 54] The effects of tip-sample convolution can be minimized by using a sharp AFM probe or by using deconvolution algorithms.[55, 54]

Depending on the instrument configuration and AFM imaging mode, surface properties that can be measured include magnetism,[56] friction,[57] elastic compliance,[58] conductance,[59] morphology,[60] piezoresponsive properties,[61] electrostatics,[62] and spectroscopic properties.[63, 23, 64, 65] There are three most general imaging modes of AFM based on the position of AFM tip with respect to the sample surface: contact, non-contact and intermittent-contact. In contact mode AFM, the AFM tip remains in constant contact with the sample surface during imaging, whereas in non-contact mode, the tip is maintained at a certain distance from the sample. For intermittent-contact

modes, the tip is driven to oscillate at or near its resonance frequency and gently "taps" the sample during scanning; intermittent-contact mode is frequently referred to as tapping-mode AFM.

2.3 Contact Mode and Lateral Force Imaging in Air

Contact mode is routinely used to image hard and stable samples which are unaffected by the tip-sample frictional force interactions. Typical forces applied in constant force mode are in the order of nN depending on the type of the tips chosen with different spring constants. As the name suggest, in contact mode, the AFM tip is in constant contact with the surface during the raster scanning motion. As the tip is scanned in contact with the sample, the bending of the cantilever will produce a change in the deflection of the laser spot focused on the photodetector. Due to surface features, small changes in cantilever deflection lead to vertical displacements of the laser spot on the position sensitive photodiode. Also, torsional twisting of the AFM tip due to frictional forces influences the lateral motion of the laser spot on the detector. The lateral force mode of imaging is sensitive to differences in chemical composition and mechanical (friction) properties of the sample.[66] Lateral force images map the changes in frictional force between the tip and the sample as it is scanned in contact with the surface.[57] The piezoelement move in z-direction to maintain a constant force between the tip and sample via an electronic feedback loop. As the tip is scanned across the surface, a voltage is applied to the z-electrode to maintain constant force between the tip and sample. Thus topography images are generated by using a calibrated sensitivity value to convert piezo voltage to real height data, while lateral force images are formed due to torsional twisting of the cantilever caused by the frictional force between the tip and sample. For contact mode AFM, topography, deflection and lateral force images are acquired simultaneously. Deflection image shows the error signal associated with the feedback loop. The deflection signal (error signal) is small when the parameters during imaging are optimized.

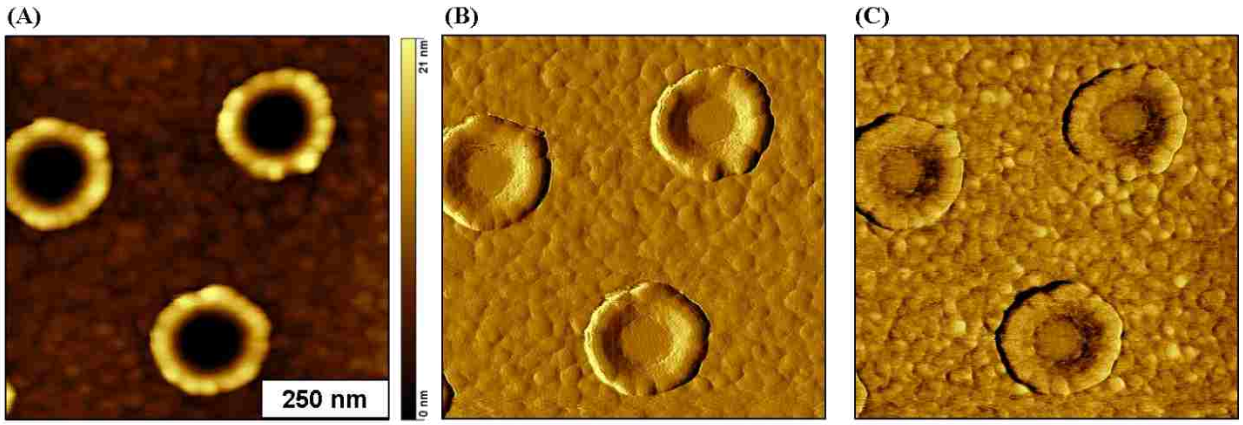

Figure 2.2 Ring nanostructures of OTS on Si(111) acquired using contact mode AFM (A) zoom in topography, (B) deflection or error signal, and (C) lateral force images

Figure 2.2 represent ring shaped OTS nanostructures on Si(111) acquired using contact mode in air. Three types of images can be acquired simultaneously with contact mode AFM: topography, deflection, and lateral force as shown in Figure 2.2. The topography image in Figure 2.2 (A) reveal brighter and taller ring shaped multilayers of OTS nanostructures while the dark area around each ring is a monolayer of OTS. The AFM deflection image in Figure 2.2 (B) represents the error signal associated with the AFM feedback loop. The deflection signal (error signal) is small when the parameters during imaging are optimized. Therefore, the deflection images are usually not reported in the literature. Lateral force images in Figure 2.2 (C) are used to distinguish differences of chemical functionalities at the interface. Quantitative nanoscale measurements of friction can be derived from lateral force images.[57, 67] Contact mode can achieve true atomic resolution at 0.01 nm vertically and 0.1 nm laterally.[68, 69, 70]

2.4 Contact Mode Imaging in Liquid

The high shear forces acting on the scanning tip in contact mode can damage delicate and soft samples. To overcome this problem, either soft cantilevers with small spring constants can be used to reduce the amount of force exerted on the sample or alternatively, one can perform contact mode in liquid media. Liquid media enables the use of smaller forces as well as reducing the stick-

slip adhesion forces, to provide higher resolution images.[70] Liquid imaging in contact mode is accomplished using a liquid cell as shown in Figure 2.3. Experiments in the liquid media are usually carried out with solvents that are optically transparent, and have a relatively slow rate of evaporation, e.g. water, ethanol, butanol or buffer solutions. The chosen solvents must be compatible and nondestructive for the sample material. Imaging in liquid media can be less destructive for soft and sticky biological samples, and provides a means to study *in-situ*, the dynamic changes at the molecular-level dimensions. Samples can be imaged using pH buffered conditions at ambient temperatures. The highest resolution reported for biological imaging with liquid AFM is on the order of 7 Å laterally, and ~1 Å for vertical resolution.[71, 72]

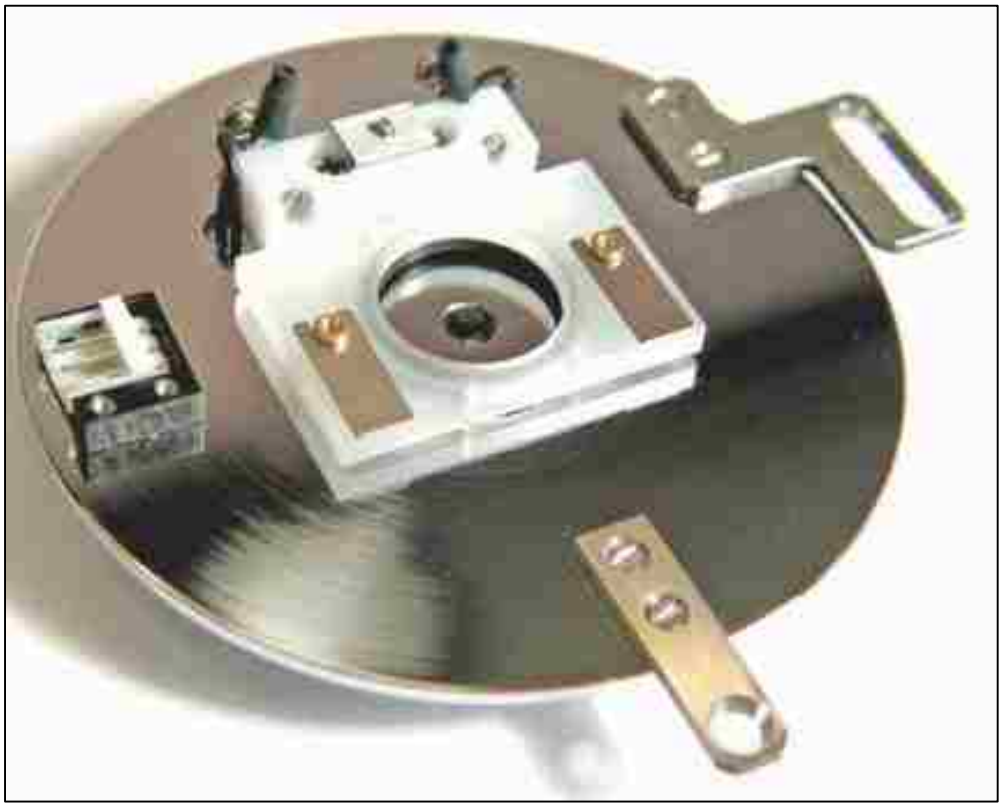

Figure 2.3 Photograph of AFM liquid cell sample plate

The pH and ionic strength of the liquid media influences adhesive interactions between the tip and sample which affects the resolution. To balance the van der Waals and electrostatic interactions between the tip and the sample, the pH and ionic strength of the imaging media can be adjusted in the buffered solutions.[71]

2.5 Force Spectroscopy Measurements with AFM in Air and in Liquid

The differences between contact mode imaging in air and liquid are apparent from force curves in respective media. Figure 2.4 represents the force distance curves obtained in air and liquid media in contact mode. For contact mode in air, as the tip approaches the sample it experiences attractive forces near the surface due to an adsorbed water layer present on all surfaces in ambient air. The water film produces stick-slip adhesion due to capillary and frictional forces in the range of 100 nN.[73] Surface attraction and capillary forces operating between the tip and sample leads to overall higher forces while imaging in air. High shear force can damage delicate samples. Force curves are a plot of cantilever deflection as a function of tip position along the z-axis.

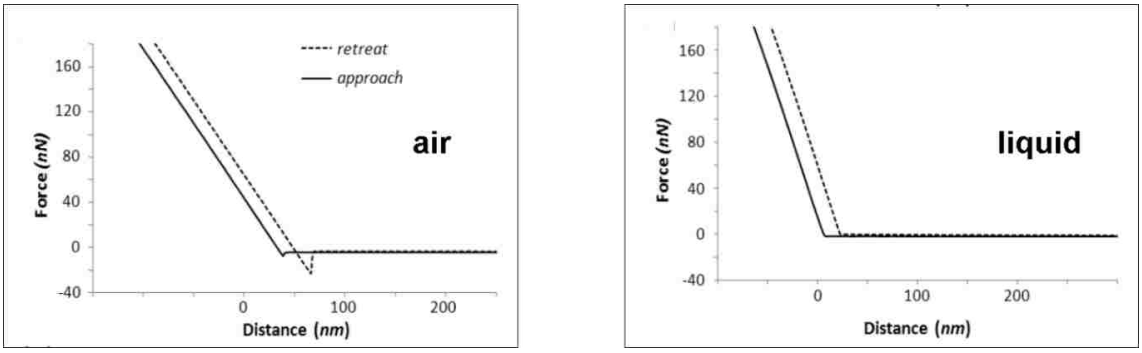

Figure 2.4 Force versus distance curves for contact mode AFM acquired in air and liquid

Capillary forces are greatly reduced by immersing both the tip and sample in liquid.[74] The capillary forces of attraction are substantially decreased when the tip is operated in liquid media as evident from Figure 2.4. In liquid media, the force between the tip and sample are greatly reduced to minimize sample perturbation, dampen vibrations, leading to reduced acoustic noise, and also to prevent damage to the sample.[75] Typical force settings used for operating in air can

range from 1 to 10 nN, whereas force settings less than 1 nN can be applied for imaging in liquid environments**.** Forces are measured using the stiffness of the cantilever according to the Hooke's law relationship to derive values from the measured deflection of the lever. The force exerted by the tip is calculated from Hooke's law as

$$F = - kz$$

where F is equal to the force applied to the tip from the sample, k is the spring constant of the probe's cantilever and z is the cantilever deflection in the z-direction perpendicular to the surface. According to the Hooke's law, the force of the AFM tip will change proportionally with tip displacement.

2.6 Tapping-Mode and Phase Imaging

Tapping mode (TM-AFM) is useful for gentle and nondestructive imaging of soft and easily deformable samples such as biologically relevant surfaces[76, 33, 77] and soft polymer interfaces.[78] In tapping mode, the tip intermittently taps the sample as it is scanned across the surface. The tip is driven to oscillate near its resonance frequency to achieve this tapping motion. The tip is driven to oscillate by a piezoceramic actuator [79] or by an external AC electromagnetic field, as with magnetic acoustic AFM or MAC-mode.[80] A stiff cantilever (higher force constant) is most commonly used for tapping-mode with the typical resonant frequency range from 160 to 300 kHz. Frictional and shearing forces which are acting on the tip in contact mode are eliminated in tapping mode, due to the oscillation of the AFM tip, thus preventing the damage of the delicate sample features on the surface.[81]

Two distinct mechanisms have been developed to drive the actuation of the AFM tip for tapping-mode. For acoustically driven vibration (AAC AFM) the tip is attached to a small piezoceramic actuator to cause mechanical vibration of the AFM tip. This setup can be problematic

when imaging in liquids. Vibration of both the liquid and the liquid cell assembly make it difficult to locate and select a resonance frequency for imaging. Selective vibration of the tip can be achieved by applying an AC magnetic field to a magnetic lever (MAC AFM). If the cantilever is coated with a magnetic material, the tip will be driven to vibrate to minimize problems for imaging in liquids.

The feedback signal for controlling the probe position with TM-AFM is obtained by maintaining a constant amplitude setting for tip deflection, rather than using a force setpoint.[82, 83, 84] The measured amplitude (output signal) is compared to the amplitude setpoint value, which is the driving AC input signal. Simultaneously acquired information with tapping-mode include topography and phase images.[85, 86] Digital images of the sample topography are obtained by recording the changes in the voltages applied by the feedback loop to maintain a constant amplitude signal at the photodiode detector. Amplitude images in tapping-mode are not recorded, because amplitude is used for positional feedback. Phase images are obtained from mapping the phase lag between the AC input signal which drives the oscillation with reference to the output signal detected due to cantilever oscillation. The phase lag of the oscillation relative to the driving AC input signal is used to generate phase images that are measured sensitively with a lock-in amplifier within the AFM controller. Material properties such as viscoelasticity, adhesion and softness are mapped by recording the difference between the phase angle of the signal that drives the tip oscillation relative to changes resulting from tip interactions with the sample.[87, 88] Thus AFM phase imaging is a useful tool for nanoscale chemistry studies for mapping compositional differences of polymer blends,[89] and organic thin films.[90, 91]

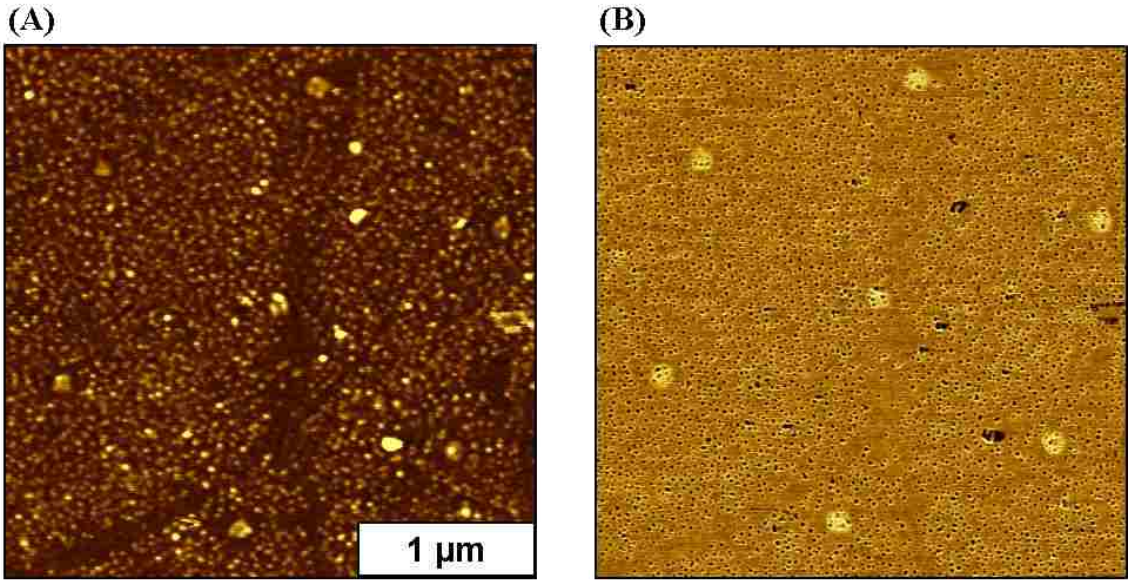

Figure 2.5 Nanopores within OTS filled with UTS on Si(111) imaged with tapping mode AFM. (A) UTS filled OTS nanopores are not clearly resolved in the topography image; (B) phase images distinctly reveal the hexagonal arrangement of seven nanopores filled with UTS

Simultaneously acquired tapping mode images of topography and phase for UTS filled OTS nanopores are shown in Figure 2.5. Using immersion particle lithography, OTS nanopores were backfilled with UTS. The differences in height between UTS and OTS areas are not clearly resolved in the topography frame of Figure 2.5 (A), due to the similarity in the molecular lengths. The hexagonal arrangement of seven nanopores were clearly resolved in the phase images of Figure 2.5 (B). The tip interacts differently with the OTS matrix and UTS nanopores, which present different terminal functional group chemistries. Changes in the phase of tip oscillation between the methyl terminated OTS and vinyl terminated UTS, with respect to the driving signal are plotted as a phase image. This change in the phase of oscillation arises from changes in the energy dissipation between the sample and the probe.

2.7 Magnetic Sample Modulation AFM (MSM-AFM)

Magnetic sample modulation, MSM-AFM is a hybrid of contact mode AFM combined with selective actuation of magnetic samples.[92] For MSM-AFM, the instrument is operated in contact mode and a nonmagnetic tip is used to map the locations and motion of magnetic nanomaterials that are driven to vibrate on surfaces. A special sample plate is used for MSM called the MAC-mode sample plate. A photograph of the underside of the sample plate is shown in Figure 2.6.

Figure 2.6 Photograph of MAC-mode sample plate

For operating the MAC-mode sample stage an AC current is applied to a wire coil solenoid to generate an oscillating magnetic field. The parameters of the AC current generates a magnetic field which alternates in polarity and strength. The strength of the magnetic field increases proportionately as the current is increased. This increase or decrease in field strength can be adjusted according to the frequency and amplitude parameters of the driving current.

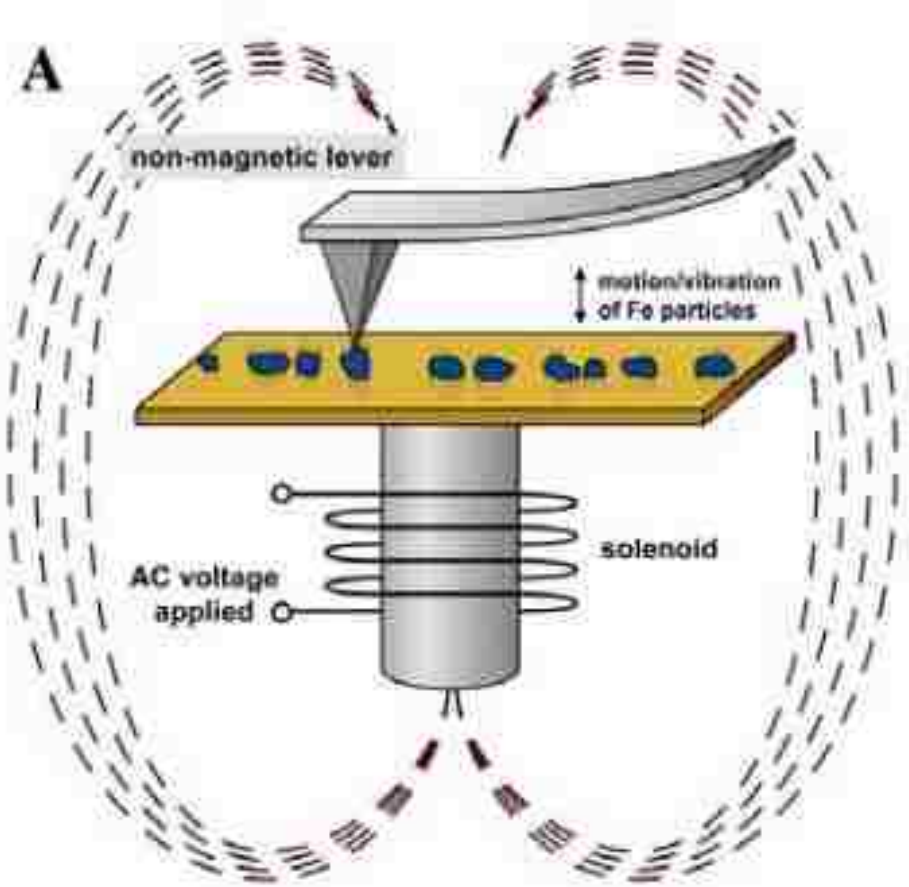

Figure 2.7 Instrument set-up for magnetic sample modulation (MSM-AFM). A non-magnetic AFM tip, scanned across the sample surface, tracks the physical vibration of the nanoparticles as they are induced to vibrate due to the flux of the magnetic field

Samples are placed on the upper side of the MAC-mode stage close to one end of the solenoid to experience the strongest flux of the AC electromagnetic field as illustrated in Figure 2.7. The oscillating electromagnetic field causes magnetic nanomaterials to vibrate. With MSM-AFM the size and location of magnetic domains can be detected, as well as information of the magnetic response and mechanical resonances of sample vibration. The image channels obtained are topography, MSM amplitude and MSM phase. When an AC current is applied to the solenoid, the frequency of the AC field causes a switching of the north and south poles of the magnetic field produced by the solenoid to create a flux. Magnetic nanomaterials on the surface are driven to

align with the flux of the switching magnetic field to induce vibration. Thus, the periodic motion of the sample vibration can be tracked by changes in the deflection of the tip. The changes in phase angle and amplitude as the tip interacts with the vibrating sample are plotted as a function of tip position to generate MSM-phase and MSM-amplitude images. The amplitude and phase components of the tip motion are tracked during the scan by a lock-in amplifier to generate spatial maps of the magnetic domains. As an AC current is applied to the solenoid, magnetic nanomaterials are driven to vibrate in response to the magnetic flux and are detected using a soft non-magnetic probe.

For an MSM-AFM experiment, typically, the surface is first scanned in conventional contact mode to acquire topography and lateral force images. The same area of the surface is then scanned again while applying an oscillating electromagnetic field. The change in polarity drives magnetic nanoparticles to selectively vibrate in response to the flux of the oscillating magnetic field. When an electromagnetic field is applied to samples, only the magnetic domains vibrate, providing selective contrast for areas that are in motion. The differences for images with and without an applied magnetic field are used to map the response of magnetic samples. Changes in the phase and amplitude of vibrating nanomaterials are mapped relative to the driving AC signal. Since a lock-in amplifier is used to acquire the amplitude and phase components of the deflection signals, slight changes in tip movement are sensitively detected. Dynamic studies of single nanoparticles can be accomplished by parking the probe on nanostructures and sweeping the field strength and frequency parameters. In comparison to conventional macroscopic magnetic measurement approaches, the field strength for MSM-AFM is on the order of 0.05 to 0.6 Tesla. Nanomaterials that have been investigated using MSM-AFM include iron oxide and intermetallic nanoparticles,[93] magnetic nanostructures patterned on surfaces,[92] and ferroproteins.[94]

Table 2.1 AFM imaging modes used for dissertation research

	Imaging mode	Feedback	Information obtained	Probe type
Chapter 3	contact mode and liquid imaging	cantilever deflection	topography and lateral force	Si or Si_3N_4
Chapter 4	contact mode and magnetic sample modulation (MSM-AFM)	cantilever deflection	topography and MSM amplitude and MSM phase (of magnetic nanoparticles)	non-magnetic soft commercial tip

2.8 Self-Assembled Monolayers of Organothiols and Organosilanes

Complex living organisms found in nature are produced by self-organization and self-construction for billions of years. Inspired by nature, scientists started developing ways to design complex structures using molecular building blocks through self-assemblies. To date, to produce nanostructures approaches such as photolithography and electron-beam lithography have been used. However, the complexity of the process combined with high equipment costs makes the conventional lithographic techniques unfavorable for many researchers. Nanofabrication using molecular self-assembly on surfaces typically occurs with a liquid phase on a smooth surface to produce nanostructures with long-range order. Molecular level self-assembly involves noncovalent or weak covalent interaction, typically van der Waals, electrostatic, and hydrophobic interactions or interfacial hydrogen bonding.[95, 96] Self-assembly is a versatile nanofabrication technique and may become the future technology for generating nanostructures such as nano-wires, nanotubes, gels, meshes, spheres, and nanoporous materials on a large scale through cost-competitive and relatively fast processes.[97] Examples of self-assembled nanostructures are monolayers of liposomes and micelles,[98] crystallized proteins,[99] colloidal particles,[100] and block copolymers.[101, 102] Thiols and silanes are the most commonly used molecules in self-assembly,[103]

although other molecules such as proteins,[99] collagen peptides,[104] and block copolymers[105] have also been widely used. This phenomenon of self-organization has developed into a subject of interdisciplinary research with overlapping areas as observed in physical, chemical and biological systems.

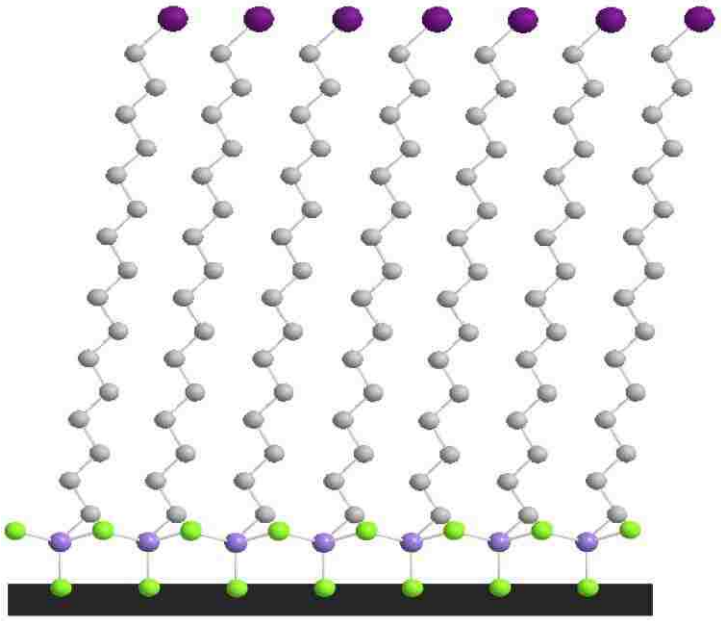

Figure 2.8 General structure of self-assembled monolayer

Self-assembled monolayers (SAMs) of thiols and silanes are used as model systems for fundamental surface studies and has led to numerous practical applications.[106, 107] Surface films of SAMs are made up of molecules that spontaneously form ordered molecular assemblies at a surface.[103] Monolayers that are single molecule thick are formed by spontaneous adsorption of long-chain amphiphilic molecules that have both hydrophilic and hydrophobic functionalities at surfaces.[108] Figure 2.8 represents the general structure of SAMs. Common to all SAM systems is a surface-active head group (green dots) that attaches to its corresponding substrate through specific chemical interactions, the second molecular part is the alkyl chain with its inter-chain van der Waals interactions which are the main forces in the simple alkyl chains, third is the tunable

terminal functional group (purple dots). The spontaneous assembly is driven by the affinity of a reactive headgroup for the surface while interactions between neighboring molecules drives the organization of the assembly in the lateral directions. The tunable terminal functional moieties such as methyl, amine, glycol, vinyl, mercapto, etc., provide numerous possibilities for generating SAM nanostructures with designed selectivity and reactivity. The result of the adsorption process is an ultrathin monolayer with a thickness that is dictated by the length of the alkyl chain. Many self-assembled monolayer (SAM) systems have been studied over the years.[103, 109, 110]

Organothiol SAMs adsorbed on gold surfaces are made up of long-chain alkanethiolates with SH headgroup at the end of an alkane chain.[111] The formation of SAMs on gold is a relatively simple, self-assembly process which is primarily driven by the attachment of the sulfur atom to the gold surface. Once the thiol molecules are chemisorbed on the gold surface, the alkyl chains of the molecules organize themselves laterally through van der Waals interactions to form a stable, densely packed monolayer. Organothiol SAMs form a commensurate $(\sqrt{3}\times\sqrt{3})R30°$ lattice on Au(111) with backbones tilted approximately 30° from surface normal.[112] Thiol SAMs on gold have been used to selectively attach proteins,[113] metals,[114] and cells.[115] The advantages that the thiol-gold combination offers, has led to the incorporation of molecules as electronic components for molecular electronics.[116, 117, 118]

Organosilane SAMs are generated by covalent bonding of alkyltrichlorosilanes $RSiX_3$ (where R is an alkyl chain and X is chloride) to hydroxylated silica surfaces. Films of OTS are chemically robust, resist oxidation, and thermal degradation due to the covalent nature of the siloxane network which links the molecules to the substrate and to neighboring molecules.[119] Organosilane SAMs can be prepared from solution[120, 121] or vapor phase[122, 123] to form densely packed monolayers. The experimental parameters such as the amount of water,[119, 121, 124

temperature,[125, 126, 127] the choice of solvent,[125, 128] adsorption time, the type of organosilane molecule chosen,[129, 130] and the chemical nature of the surface,[120, 129] greatly affect the molecular density and the quality of silane monolayer. Organosilane SAMs were formed on flat substrates such as silicon oxide, metal oxides, quartz, glass, gold and mica.[103] Organosilane SAMs are used for sensors,[131, 108] molecular electronic devices,[132] lubricants,[133] and semiconductor coatings.[134]

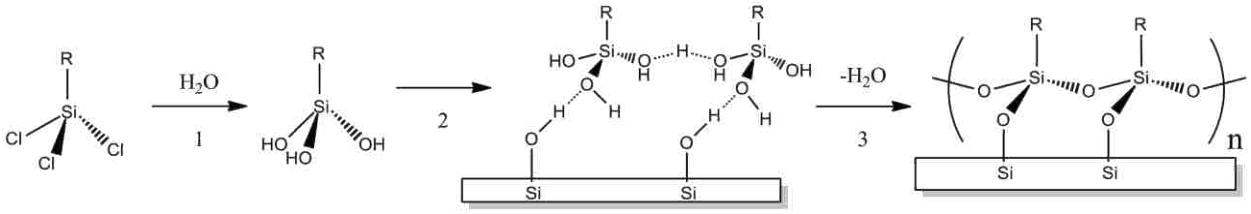

Figure 2.9 Mechanism of surface self-assembly of trichlorosilanes

The general steps of the hydrolysis of trichlorosilanes to form SAMs on surfaces is depicted in Figure 2.9.[119, 135] The role of trace amounts of water during surface self-assembly of trichlorosilanes to form a uniform monolayer was first studied by Jacob Sagiv in 1980. First, trichlorosilane molecules react with a trace amount of water on the surface to form silanol molecules. Subsequently, silanol molecules adsorb to surface reactive sites and then undergo a condensation reaction with free hydroxyl groups on the surface. Next, each hydrolyzed silane molecule forms siloxane bonds to anchor to the surface and also connect to neighboring molecules to form a network of Si - O - Si bridges. The alkyl chains adopt an all-trans configuration with tilt angle values reported that range from 0 to 15°.[103] The thickness of the OTS monolayer ranged from to 2.25 to 2.81 nm.[136] Trichlorosilanes are highly reactive in the presence of water and can form multilayers through self-polymerization either on the surface or in solution, depending on experimental conditions.[137, 138] In this dissertation, patterned OTS monolayer and multilayer assemblies were prepared using particle lithography. The next section gives an overview of colloidal self-assembly for nanofabrication of patterned surfaces.

2.9 Nanofabrication of Patterned Surfaces Using Particle Lithography

Nanofabrication technology employs techniques like photolithography,[139] interference lithography,[140] (IL) electron beam lithography,[141] (EBL) focused ion beam lithography,[142], [143] (FIB) where the tools are used to mould, pattern, erode or etch base materials to produce nanostructures with the desired geometry. Considerable research efforts have also been invested over the years to develop new techniques like self-assembly, nanosphere lithography,[144] (NSL) soft lithography,[145] to build organized arrays of nanostructures from smaller elements and base materials. Since 1995, nanosphere lithography has been applied to manufacture one-, two-, or three-dimensional nanostructures as shown by literature reports in Figure 2.10.

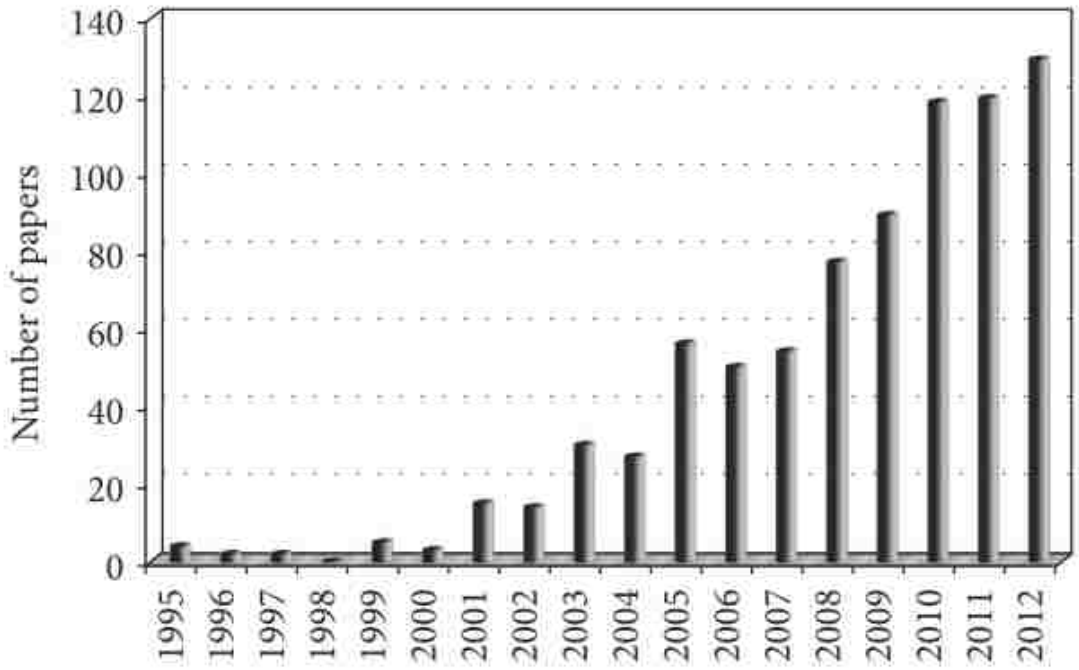

Figure 2.10 Number of papers/year related to NSL, as retrieved by Scifinder Scholar (July 2013)

Nanolithography based on colloidal particles is inexpensive, easy to implement, has high throughput involving simple bench top chemistry protocols.[146] Particle lithography also known as

colloidal lithography,[147] nanosphere lithography,[148] or natural lithography[149] is an inexpensive fabrication method for producing regular and well-ordered surface patterns. Particle lithography provides a number of advantages such as uniform geometry, high throughput, and reproducibility. The process of particle lithography is divided into two steps, the first of which is the preparation of surface mask. A suspension of monodisperse mesospheres made up of either polystyrene latex or silica is deposited on a flat surface. Upon drying, the mesospheres naturally self-assemble into a close-packed arrangement on flat surfaces. In the second step, desired materials are deposited thorough the interstices of the mesosphere surface masks to produce nanostructures with precise spatial positioning. The surface mask is subsequently removed by steps of rinsing and sonication in a suitable solvent to generate an array of nanostructures on the substrate. The surface nanopatterns generated with particle lithography correspond to the diameter and periodicity of the mesospheres used for the mask. Therefore, the spacing and size between the nanopatterns can be selected by choosing the diameters of mesospheres. The tunable terminal functional moieties provide possibilities for generating SAM nanostructures with designed selectivity and reactivity. Particle lithography has been used to pattern nanomaterials such as nanoparticles,[150] proteins,[151] organosilanes,[152, 153] and metals.[154, 155]

In this dissertation, organosilane SAMs composed of octadecyltrichlorosilane (OTS) were prepared by a combination of particle lithography along with self-assembly. Particle lithography approaches were used to prepare organosilane nanoring and nanopore geometries using procedures with vapor deposition or immersion steps. Examples of the two types of nanostructures generated after each process are shown in Figure 2.11. An AFM image of a surface mask of latex mesospheres is shown in Figure 2.11a. After the removal of latex mask, OTS nanorings were formed with vapor deposition (Figure 2.11b) and OTS nanopores were formed with immersion

particle lithography (Figure 2.11c). The ring nanostructures were used as 3D test platforms to study the solvent responsive properties of OTS multilayers. The OTS nanopores were functionalized further with specific chemical groups to attach nanoparticles. The properties of surfaces coated with SAMs can be tailored by the selection of molecular endgroups to provide spatially selective sites for further adsorption of nanomaterials.

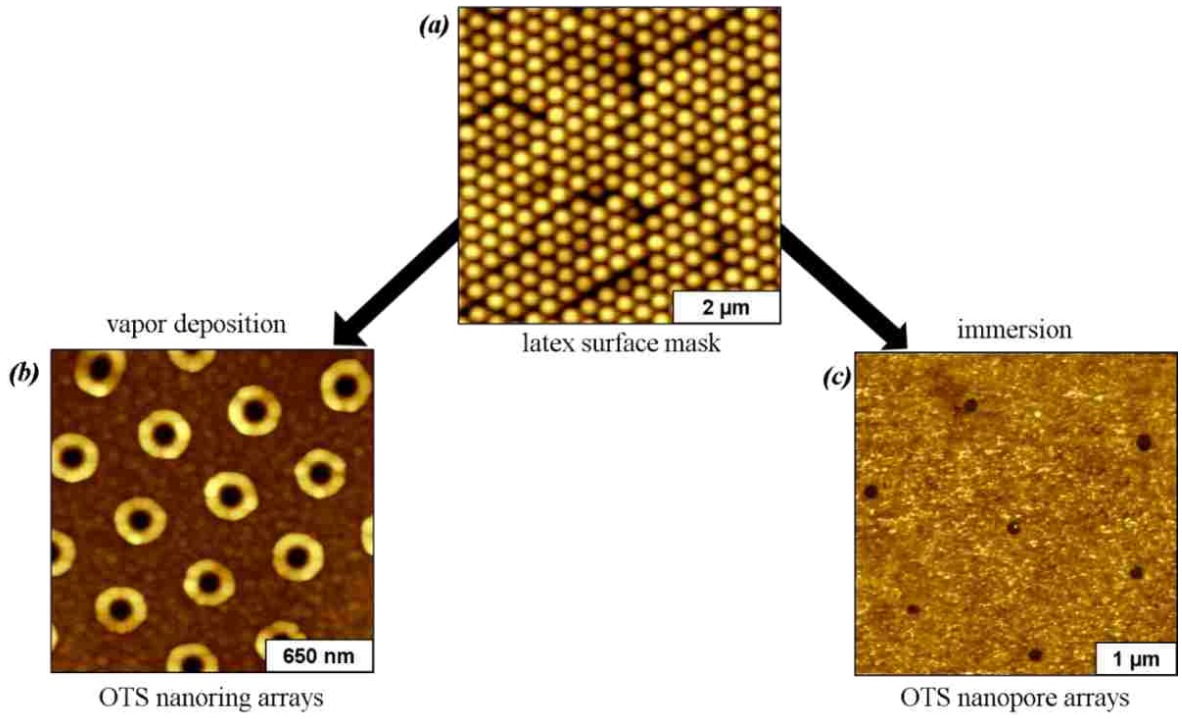

Figure 2.11 Nanostructure geometries formed using particle lithography with OTS. (a) Surface mask of 200 nm mesospheres; (b) OTS ring nanostructures formed after vapor deposition; (c) OTS nanopore structures formed with steps of immersion particle lithography

CHAPTER 3: SOLVENT-RESPONSIVE PROPERTIES OF OCTADECYLTRICHLOROSILOXANE NANOSTRUCTURES INVESTIGATED USING ATOMIC FORCE MICROSCOPY IN LIQUID*

3.1 Introduction

An important direction for nanoscale studies is to investigate structural changes for materials in response to environmental parameters, such as with effects of light, heat, pH changes, or in different solvents. Liquid atomic force microscopy (AFM) has been applied for nanoscale studies of biological samples in their native environment,[15,156,157] *in situ* studies of the effects of different liquid media such as with changes in pH or ion concentration,[158,159,160] for *in situ* studies of electrochemical reactions,[161,162,163] and for observing time-lapse images of progressive surface changes caused by chemical reactions.[164,165,166] Wettability studies of the interaction of liquids with self-assembled monolayers have been fundamental for understanding the properties of organic thin films.[167,168,169,170,171] However, the actual physical changes of surfaces coated with organic films and nanostructures have not been well documented regarding solvent-responsive properties.

Applications are being developed for stimuli-responsive materials which respond to changes in environment, particularly for polymer samples.[172,173,174,175] As an example application, encapsulation and release of a fluorescent dye was accomplished by changes in swelling of polymer nanocapsules induced by altering the solvent.[176] A surface sensing platform was developed based on actuation of nanoparticles coupled to polymer brushes which respond to changes in the solution pH or solvent.[177,178] Solvent-responsive changes in friction coefficients were reported for patterned polymer brushes comprised of polystyrene.[179]

* Chapter 3 previously appeared as Kulkarni, S. A.; Lyles, V. D.; Serem, W. K.; Lu, Lu.; Kumar, R.; Garno, J. C. Solvent-responsive properties of octadecyltrichlorosiloxane nanostructures investigated using atomic force microscopy in liquid, 2014. It is reprinted by permission of American Chemical Society Publications (see page 81).

The swelling and collapse of poly(methyacrylic acid) polymer brushes was detected with AFM in response to changes in solution pH.[180] Samples that respond to changes in pH include poly(2(tert-butylamino)ethyl methacrylate polymer brushes,[181] polyampholyte polymer brushes of diblock copolymers,[182] poly(*N*,*N*-dimethylaminoethyl methacrylate) grafted polythiophene,[183] amphiphilic block copolymers of poly(styrene-*b*-acrylic acid),[184] poly(allylamine hydrochloride)-containing polyelectrolyte multilayer films,[185] polystyrene-b-poly(4-vinylpyridine) block copolymers,[186] and poly(methacrylic acid) brushes.[187] The swelling of polymer brushes consisting of poly(N-isopropyl acrylamide) and poly(acrylic acid) was evaluated in response to changes in pH and temperature.[188] Photografted films of poly(acrylic acid) were reported to swell in response to changes in pH when characterized with Fourier transform infrared spectroscopy.[189] Hydrophobic and electrostatic interaction forces were mapped using chemical force microscopy for a film of stimuli-responsive copolymers in response to changes in salt concentration.[190]

Solvent-induced swelling of alkoxysilane thin films on silicon has been detected using techniques such as neutron and X-ray reflectivity.[191] For organosilane films or polymers, the reactivity of side groups for further reaction steps is greatly influenced by the choice of solvents. The solvent responsiveness of structures assembled with Au nanoparticles and CdTe nanowires with a poly(ethylene glycol) bridge were reported to change conformation in different solvents, which altered the distance between the nanoparticles and nanowires.[192] The swelling of PEG linkers caused by interactions with solvents were shown to affect the distance of the gap between the nanoparticles and nanowires to influence measurements of the plasmon-exciton interactions.

It has been difficult to directly visualize subsurface changes for organic films using AFM studies, because only the upper surface can be examined locally with probe-based techniques. Changes below the surface of a film that are caused by solvent penetration typically cannot be

detected with AFM. In this report, we have designed a 3D interface to study the effects of solvent penetration within multilayer nanostructures of octadecyltrichlorosiloxane (OTS). Samples were compared in air and liquid media using AFM studies with the same probe and sample. At the nanoscale, substantial changes were observed for the physical shapes and heights of OTS nanostructures that depend on the solvent and intervals of immersion.

3.2 Materials and methods

3.2.1 Materials and reagents

Particle lithography with vapor deposition was used to generate organosilane nanopatterns on surfaces, as previously reported.[193,153] Pre-cut single sided, boron-doped polished Si(111) wafers (Ted Pella, Redding, CA) were used as substrates. Pieces of Si(111) were cleaned by immersion in a 3:1 (v/v) piranha solution for 2 h. Piranha solution consists of sulfuric acid and hydrogen peroxide (Sigma-Aldrich, St. Louis, PA) which is highly corrosive, and should be handled carefully. After acid cleaning, the substrates were rinsed with deionized water and dried in air. Monodisperse latex mesospheres, 200 nm diameter (Thermo Scientific, Waltham, MA) were used as surface masks for patterning. Octadecyltrichlorosilane (OTS) was purchased from Gelest (Morrisville, PA) and used without further purification.

3.2.2 Atomic Force Microscopy

Samples were characterized using a model 5500 scanning probe microscope (Agilent Technologies, Chandler, AZ). Images were acquired by contact mode AFM using V-shaped cantilevers with oxide-sharpened silicon nitride probes which had an average force constant of 0.5 N/m (Model MSCT, Veeco Probes, Santa Barbara, CA). Images were processed using Gwyddion open source software, which is freely available on the Internet and supported by the Czech Metrology Institute.[194] Analysis of surface coverage was accomplished with multiple images by manually selecting a threshold value to convert images to black and white frames, and counting

pixels using the UTHSCSA *ImageTool* program, developed at the University of Texas Health Science Center, San Antonio, Texas and available from the Internet (http://compdent.uthscsa.edu/dig/itdesc.html).

3.3 Results and Discussion

Nanopatterns of OTS were prepared to furnish reproducible 3D surface geometries as a reference shape for quantitatively evaluating molecular-level changes in selected liquid environments. To prepare the nanorings, monodisperse latex spheres were used as a surface mask (Figure 3.1A) for subsequent deposition of OTS from the vapor phase. After removal of the mask of latex particles, organosilanes persist on the surface to form a periodic array of ring-shaped nanostructures with periodicity corresponding to the initial diameter of the latex spheres (Figure 3.1B). Circular sites of a liquid meniscus surround the base of each bead, which provides sites for growth of OTS.[153]

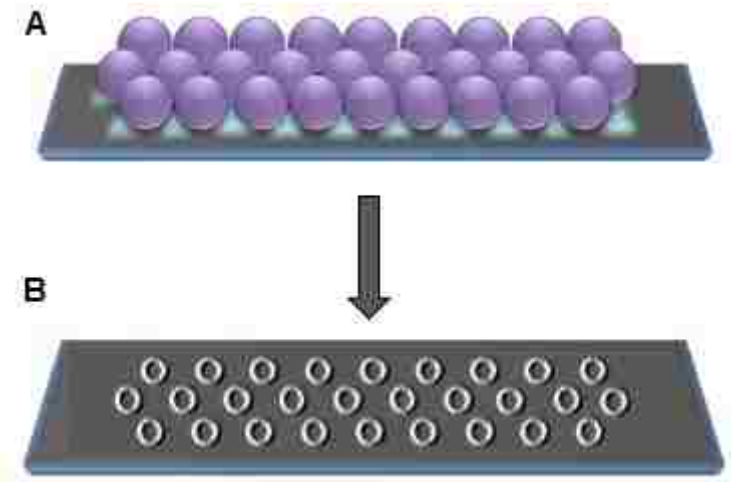

Figure 3.1 Basic steps for preparing OTS ring nanostructures using particle lithography. (A) A surface mask of latex particles was prepared. (B) After vapor deposition of OTS, the mask was removed by solvent rinses to reveal a periodic arrangement of ring-shaped nanostructures.

Views of as-prepared nanostructures of OTS are shown in Figure 3.2, comparing images side-by-side that were acquired in air and ethanolic media. The same sample and AFM probe were used for the data panels of Figure 3.2, before and after the sample was immersed in ethanol. Although the images were collected sequentially, there were no prominent defects evident to use as landmarks for *in situ* imaging. The top row shows representative images acquired in ambient air. There are 278 nanorings packed closely within the 4×4 um^2 topography frame in Figure 3.2A, which would scale to an approximate surface density of 10^9 nanostructures/cm^2.

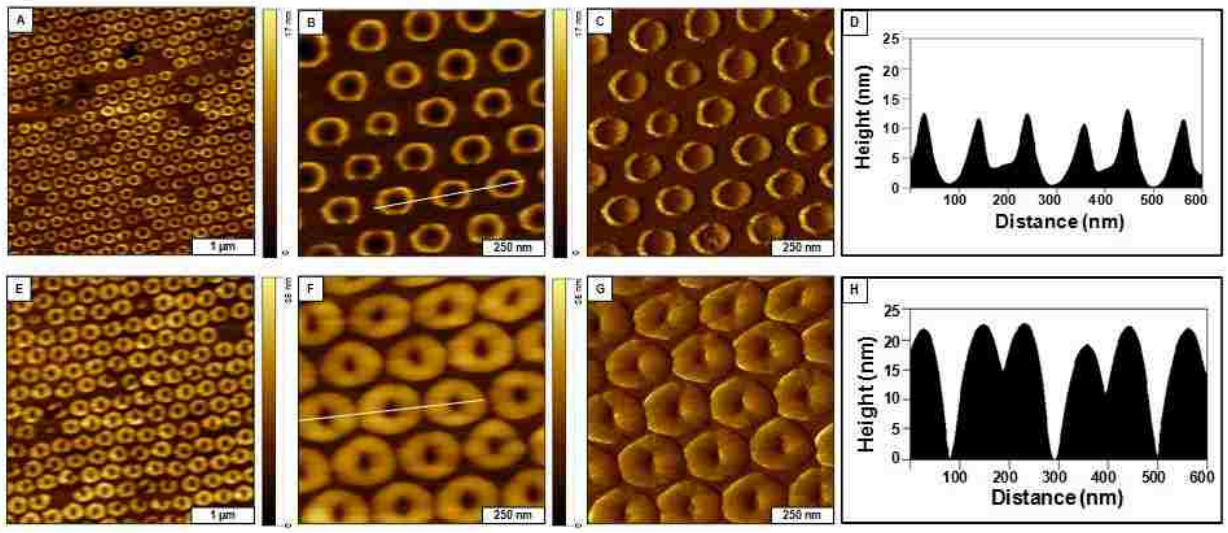

Figure 3.2 . Side-by-side comparison of OTS nanostructures prepared with 200 nm latex spheres imaged in air (top row) and with immersion in liquid media (bottom row). (A) Topograph in air; (B) Zoom-in topography frame; (C) simultaneously-acquired lateral force image; (D) Height profile for the white line shown in B. (E) Topography frame of the same sample subsequently acquired in ethanol using the same AFM probe; (F) Zoom in topograph; (G) corresponding lateral force image; (H) Line profile for F.

There are a few areas that are missing nanostructures where the close-packed spheres of the latex mask were not perfectly pressed against the surface; approximately 9% of the surface has missing nanostructures. Zooming in for a closer view of the shapes of the nanostructures (Figures 3.2B - 3.2C) the edges of the ring nanostructures are quite distinct for both the topography and

corresponding lateral force frames acquired in air. The shapes of the rings conform to the sites of the water meniscus formed between the latex beads and the substrate where multiple layers of OTS were produced by self-polymerization. The areas in the center of the rings pinpoint the locations where the latex beads made direct contact with the surface, whereas the areas between the rings have a vapor deposited monolayer of OTS. Multilayers formed only in the circular areas of the meniscus between the latex spheres and the surface. The differences in height for the center of the rings compared to the areas between the rings are apparent in the representative line profile of Figure 3.2D. The spacing between the nanorings (center-to-center) measures 202 ± 4 nm, closely matching the diameter of the latex spheres used as a surface mask. The areas in the center of the rings reach the baseline of the substrate, whereas between the rings the film thickness measures about 3 ± 1 nm, which is in general agreement with the expected value of 2.26-2.76 nm reported previously for a densely-packed monolayer of OTS which depend on conditions of sample preparation.[195,196,197,136] The average height of the nanorings when imaged in air measured 10 ± 2 nm, which corresponds to at least 4-5 molecular layers of OTS. However, depending on the amount of crosslinking there may be as many as 20 layers if the molecules are arranged in a compressed, side-on packing arrangement.

When the same sample was immersed in ethanol the dimensions of the OTS nanorings were observed to change considerably in height, width and surface coverage, as shown in Figures 3.2E - 3.2G. The swelling of the OTS nanorings is readily apparent, particularly when comparing images in Figure 3.2B (air) versus 3.2F (ethanol). The gaps between the rings have become narrower in Figure 3.2F, such that some of the rings are touching. The same effect was observed for experiments with multiple samples and probes, and therefore the changes cannot be simply ascribed to imaging artifacts; particularly since the same AFM tip was used for all of the frames

shown in Figure 3.2. To evaluate the surface changes quantitatively, the surface coverage of the brighter areas was estimated using pixel counting. For the sample imaged in air ~53% of the sample was covered with the taller regions of OTS nanorings. When the sample was immersed in ethanol the surface coverage increased to 77% for the thicker regions. The swelling of the rings is also evident in the lateral force images comparing Figures 3.2C (air) with 3.2G (ethanol). Although the changes may not be discernible at the macroscopic level with more commonly used approaches for characterizations of thin film materials, changes of a few nanometers are quite prominent when investigated with AFM. The height of the areas of the nanorings has doubled, to measure 20 ± 2 nm as shown with a representative line profile in Figure 3.2H. Thus, the interaction of the solvent with the 3D surface of the OTS nanorings produced significant changes in the molecular conformation which expanded the overall height and lateral dimensions of the ring nanostructures.

Although the sample was prepared using only OTS, there are three distinct domains revealed in the lateral force images and cursor profiles of Figure 3.2: the uncovered Si(111) areas at the center of the nanorings which were protected by the latex masks, the OTS multilayers which form the nanorings, and the interstitial regions between the rings. The thickness of the interstitial areas between the nanorings corresponds to a monolayer. Within these areas, the molecules are densely arranged in a nearly upright orientation, presenting methyl groups at the interface. One would expect that for a monolayer of OTS the effects of the solvent would be negligible and changes in thickness would not be detected. However, for the taller areas of the nanorings the measured thickness indicates that a multilayer structure was formed. A different surface chemistry is presented at the interface of the nanorings than for the methyl-terminated areas in between, evidenced by the differences in color contrast with the lateral force images, Figures 3.2C and 3.2G. The crosslinked arrangement of layered molecules with Si-O-Si bridges is not close-packed so that

solvent molecules can penetrate between the layers. When the samples were dried and solvent is not present, the packing between layers of the nanorings is condensed and the nanostructures compress into structures with shorter heights. Swelling of the nanorings was observed regardless of the size of the nanostructures. A further control experiment was done for a sample prepared using a larger diameter surface mask of 300 nm mesospheres, results are shown in Supporting Information, Figure A1.

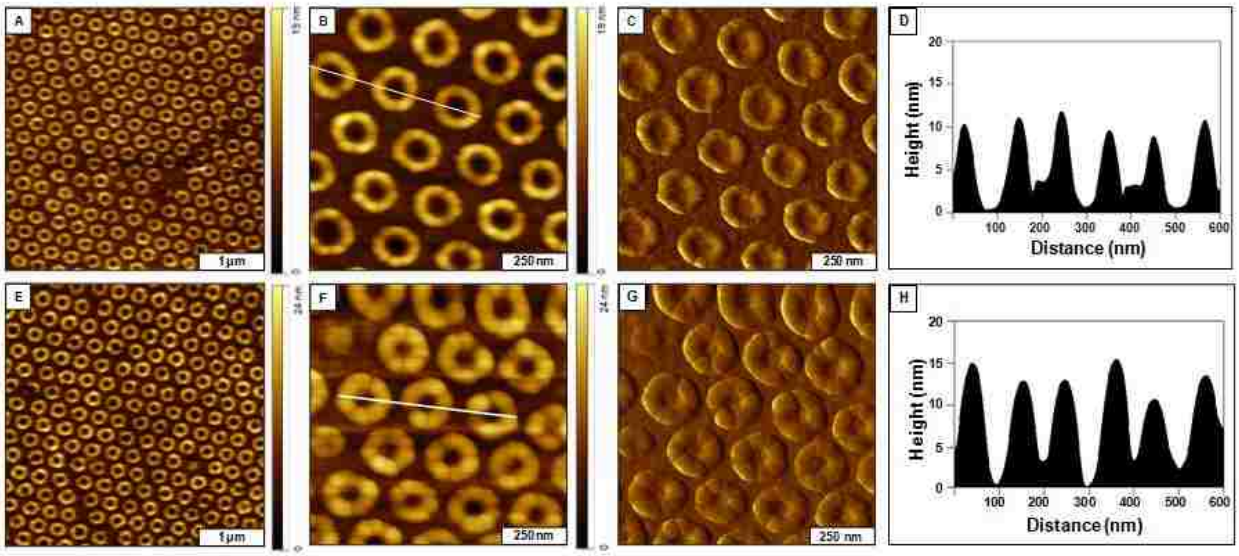

Figure 3.3 Comparison of annealed samples of OTS nanorings imaged in air (top row) and ethanol (bottom row). (A) OTS nanorings imaged in air after annealing; (B) zoom-in topography view; (C) corresponding lateral force image for B; (D) cursor profile for the line drawn in B. (E) Nanorings of OTS acquired in ethanol after an annealing step; (F) Zoom-in topography view in ethanol; (G) corresponding lateral force frame for F; (H) cursor profile for F.

The effects of annealing the OTS nanostructures were evaluated with AFM experiments to determine whether crosslinking between strands would take place. In previous reports, an annealing step has been applied with organosilane films to remove ethanol molecules at the surface and interface and to promote dehydration of trapped water molecules in between multilayers.[198,199,200] The nanostructures were annealed at 120 ^{o}C for 2 h, then imaged in air and ethanol (Figure 3.3). The results in the top row reveal the arrangement and shapes of the annealed

rings acquired in ambient conditions (Figures 3.3A - 3.3C). Within the close-up view (1×1 μm^2), 20 nanopatterns are aligned with well-defined periodicity (Figure 3.3B); and the corresponding lateral force image is shown in Figure 3.3C. A representative line profile (Figure 3D) reveals that the thickness of OTS in areas between the rings is taller than within the very center of the rings where the mesospheres made contact with the substrate. Thus, multilayers formed in the meniscus sites and the gaps between the rings appear to have a monolayer of OTS. The height of the rings in air measured 10 ± 1 nm, which is comparable to the measurements of the as-prepared sample. An annealing step thus did not produce a detectable change in the thickness of the nanostructures in air when evaluated with AFM studies. When the annealed sample was imaged in ethanol, (Figures 3.3E - 3.3G) swelling of the nanorings was still detected. For the wider view of Figure 3.3E, differences in the size of the rings are not easily detectable compared to the same size view of Figure 3.3A acquired in air. However, the changes become visible with a zoom-in view (Figure 3.3F). There are 20 nanopatterns shown within the 1×1 μm^2 area (Figures 3.3F - 3.3G) which are taller and wider than the same size area viewed in ambient air (Figures 3.3B - 3.3C). The height of the rings when imaged in ethanol increased to 12 ± 2 nm (Figure 3.3H).

Comparing the surface changes of nanostructures in ethanol for the annealed sample (Figure 3.3F) versus the as-prepared sample of Figure 3.2F indicates that there is less swelling for the annealed nanostructures. The annealing step removed residual traces of water and solvents from the surface, and provided a way to fully dry the sample. In ethanol, somewhat less swelling was observed because permeation of ethanol into the multilayers decreased, this is most likely attributable to further cross-linking of the film. The images shown in Figures 3.3E - 3.3G were acquired within a few hours of ethanol immersion. A longer immersion step was tested to evaluate whether the swelling of the nanostructures would increase with more time.

The annealed OTS nanostructures were immersed in ethanol for 40 h (Figure 3.4). The annealed sample of OTS nanorings imaged in air are shown in the top row of Figure 3.4, and the bottom row has images of the same sample after prolonged 40 h immersion in ethanol. The wide area (4×4 μm^2) frames (Figures 3.4A versus 3.4E) do not reveal detectable changes in the sizes and shapes of the OTS nanorings at this magnification. However, at higher magnification (1×1 μm^2) the zoom-in views disclose changes in the sizes of the rings caused by swelling (Figures 3.4B versus 3.4F).

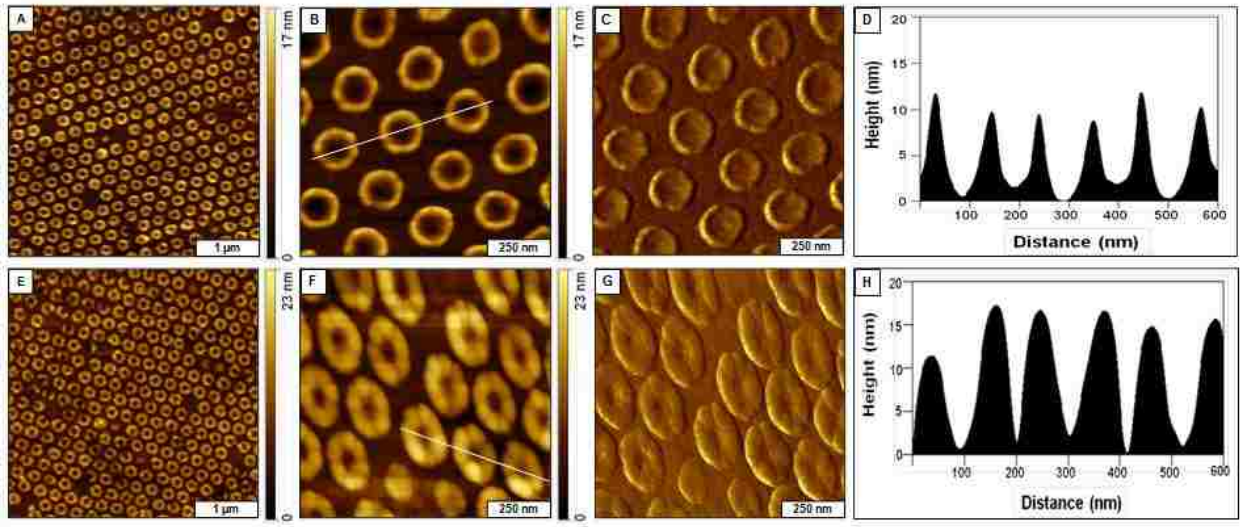

Figure 3.4 Changes of an annealed sample of OTS nanorings after prolonged soaking in ethanol for 40 h. (A) Nanorings of annealed OTS nanorings imaged in air; (B) zoom-in topography view; (C) lateral force image for B; (D) height profile for the line in B. (E) Nano structures of annealed OTS after 40 h immersion in ethanol; (F) zoom-in view; (G) lateral force image for F; (H) height profile for line in F.

The lateral force frames (Figures 3.4C versus 3.4G) more clearly reveal the changes in the shapes of the rings caused by swelling; the rings become wider and have a round appearance after prolonged soaking in ethanol. The height of the rings in air measured 10 ± 1 nm (Figure 3.4D) compared to 15 ± 3 nm (Figure 3.4H) after soaking in ethanol. A slight distortion of the circular ring shapes is observed in Figures 3.4F and 3.4G, however the swelling of the rings is still clearly

detectable compared to the dried sample shown in Figure 3.4B. The same tip and sample were used for the sequential experiments. The surface coverage of the annealed OTS nanorings after 40 h immersion in ethanol measured 59 ± 1 %.

Structural changes of OTS nanostructures for studies in ethanol are presented side-by-side in Figure 3.5. The swelling of OTS multilayers was found to be reversible; the same sample could be cycled by steps of drying and ethanol immersion to reveal compressed, compact nanostructures in air and swollen, enlarged rings in ethanolic media. The 3D representations provide a clear picture of the morphology changes in thickness and lateral dimensions.

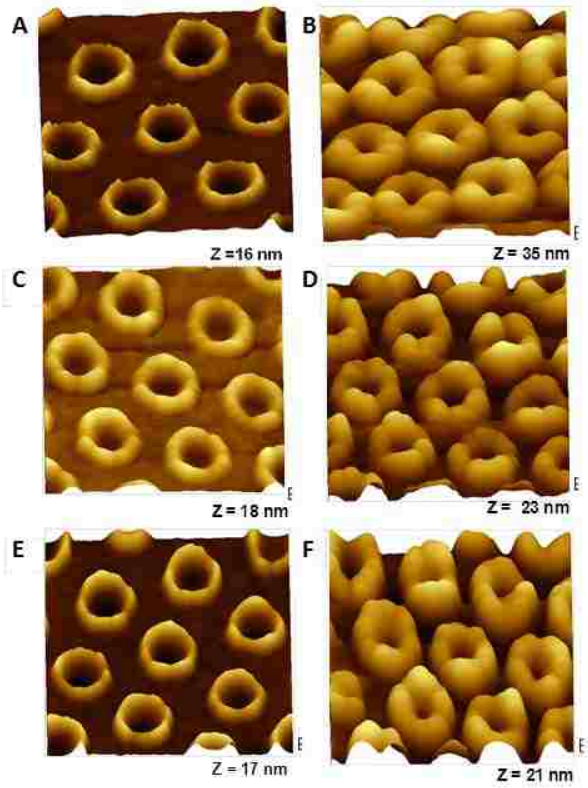

Figure 3.5 Structural changes of OTS nanorings imaged in air (left column) compared side-by-side with views in ethanol (right column). The images are 600 x 600 nm2 in dimension. (A) Freshly prepared sample in air; (B) same sample imaged in ethanol. (C) Annealed sample imaged in air; (D) annealed sample immersed briefly in ethanol. (E) Annealed sample before immersion; (F) Annealed sample after 40 h immersion in ethanol.

The topography views are shown in pairs, imaged using the same AFM probe to provide a systematic comparison. A freshly prepared sample imaged in air and ethanol is compared in Figures 3.5A and 3.5B. After annealing (120^{o}C for 2 h), the views in air and ethanol are shown in Figures 3.5C and 3.5D, respectively. With longer soaking in ethanol, an annealed sample is compared in air versus ethanol in Figures 3.5E and 3.5F.

A summary of the dimensions measured for OTS nanorings is presented in Table 3.1 for the tested sample conditions. Significant swelling of both the vertical and lateral dimensions of OTS nanostructures was detected in ethanolic media for the freshly prepared and annealed nanostructures. The changes were reversible, when the sample was removed from ethanol and dried the nanorings returned to the compressed state. The annealed nanorings were observed to increase in dimension in ethanolic media; however, the annealed samples did not expand and grow to be as large as the freshly-prepared nanostructures. The surface coverage of freshly prepared nanorings increased from 53% (air) to 77% in ethanol, compared to 59% for the annealed sample. The freshly prepared sample doubled in thickness, growing from 10 nm to 20 nm in height, whereas the annealed sample after 40 h immersion in ethanol measured 15 nm in height.

Table 3.1 Measurements of OTS nanorings imaged with AFM in air or ethanol

Sample description	Width of nanorings* (nm)	Height* (nm)	Surface coverage (%)
Freshly prepared sample in air	26 ± 4.5	10 ± 2	53 ± 1.1
Freshly prepared sample in ethanol	100 ± 9.3	20 ± 2	77 ± 0.3
Annealed sample in air	26 ± 4.5	10 ± 1	53 ± 0.9
Annealed sample in ethanol	85 ± 18	12 ± 2	64 ± 1.0
Annealed sample in air	28 ± 12	10 ± 1	53 ± 2.2
Annealed, soaked 40 h in ethanol	56 ± 16	15 ± 3	59 ± 1.0

* *Average of 100 measurements ± standard deviation.*

The solvent responsive properties of OTS nanostructures were further evaluated in aqueous media (Figure 3.6) in a phosphate-buffered saline solution (PBS). Imaging with liquid AFM requires a solvent that does not evaporate quickly, so aqueous solutions were used for our studies.

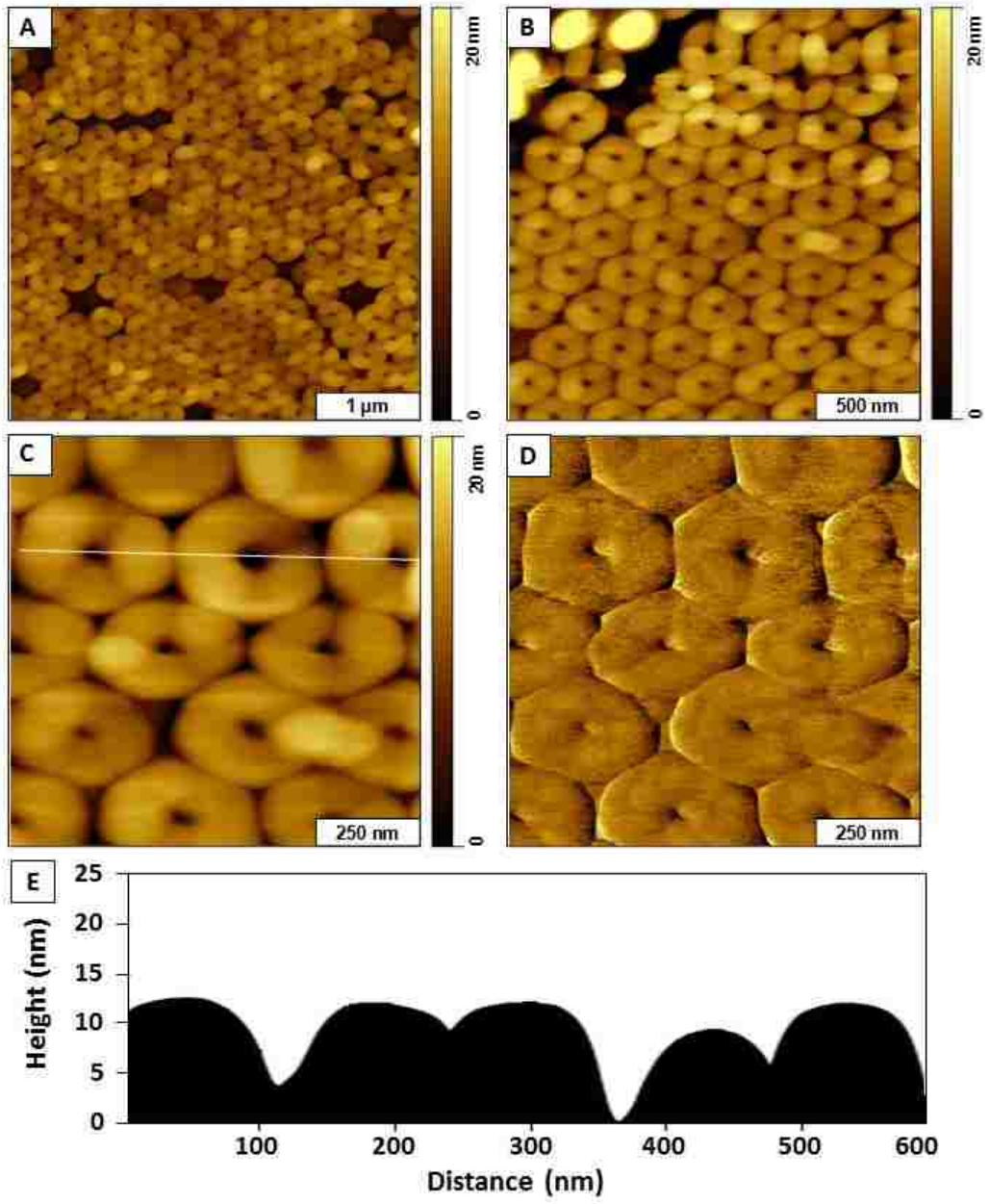

Figure 3.6 Nanorings of OTS imaged in PBS, pH 7. (A) Topography view, 4×4 µm2; (B) Zoom-in topograph, 2×2 µm2; (C) Close-up topography frame, 1×1 µm2; (D) Lateral force frame for C; (E) Cursor profile for the line in C.

The nanorings swelled to completely fill the areas in between to form expanded surface structures. The successive zoom-in topographs of Figure 3.6 reveal nearly hexagonal shapes as the multilayers of OTS expand to fill the spaces between the nanopores. A cursor line across three nanorings (Figure 3.6E) profiles the approximate shapes of the surface features, however it is likely that the AFM probe does not touch the bottom of the substrate at the centers of the nanopores. The thickness of the nanorings is greater than 10 nm; however an average measurement was not obtained for this sample because of the significant swelling at the centers of the rings.

For dried samples of OTS nanorings, the multilayer areas of the nanorings form compressed and compact structures. When the surfaces are wet, solvents intercalate between the polymer strands to generate larger structures, increasing as much as two-fold in overall dimensions. The expansion of the polymerized molecule into an extended upright configuration in 3D would fill a volume resembling a cone. A rough approximation of the structural changes in multilayer rings is represented in Figure 7. Calculations of changes in volume show an increase of greater than 700% comparing the dried sample in air versus ethanol (calculations are explained in Supporting Information, Figure A2). The samples which were annealed to induce cross-linking do not expand as much as the fresh sample, an increase in the volume of the nanorings measured 240% for the annealed sample, even after longer immersion in ethanol. Greater swelling of OTS rings in lateral dimensions was observed in water compared to ethanolic media. The monolayer areas of OTS between rings most likely do not change height when immersed in liquids, because it is already in a close-packed arrangement. It has previously been reported for surfactant films that there is little or no solvent penetration into a surface monolayer, which maintains its thickness and other physical properties after wetting.[201] Further directions for this research will be to evaluate the surface changes in solvents with different polarity, pH or ionic strength.

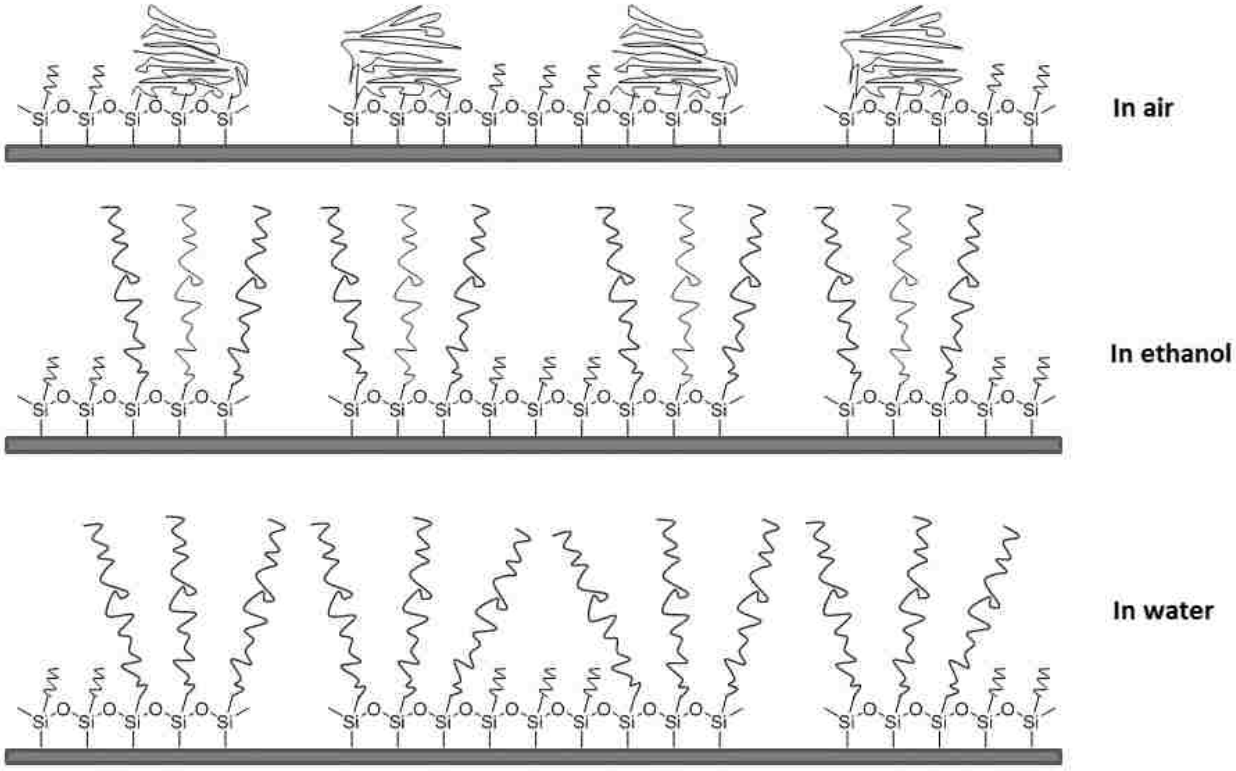

Figure 3.7 Approximate representation of molecular changes for solvent-responsive OTS nanostructures. In air, (top) the multilayers condensed into a compact structure. When immersed in ethanol (middle) the polymer strands stretched to form taller and wider structures. In aqueous media (bottom) the strands expand further in lateral directions.

3.4 Conclusion

Nanolithography enables molecular-level control of the spacing and composition of patterned elements for AFM studies in liquid media. Particle lithography combined with vapor deposition was used to fabricate ring-shaped nanopatterns of OTS with well-defined 3D geometries and periodicity. In liquid media, solvents or buffer penetrate between the polymer strands of OTS multilayers to change the physical sizes and shapes of nanostructures. The heights and widths of multilayer OTS nanostructures increased substantially when immersed in ethanol or buffer, compared to samples that were dried in air. Even after heating, swelling was evident for annealed OTS nanorings immersed in ethanolic media. Samples dried and imaged in air had relatively similar heights and sizes; whereas after immersion in ethanol the OTS nanostructures

swelled and increased in dimension. Future directions for this research will be to develop AFM-based protocols to evaluate stimuli-responsiveness of nanostructures in response to pH, light and temperature.

CHAPTER 4: INVESTIGATION OF THE VIBRATIONAL RESPONSE OF PATTERNED ARRAYS OF Fe_3O_4 NANOPARTICLE CLUSTERS USING MAGNETIC SAMPLE MODULATION AFM (MSM-AFM)

4.1 Introduction

Magnetic nanoparticles have promising potential for applications such as high-density data storage,[202,203] nanoscaled magnetic sensors,[204] nanoelectronics,[205] sensing,[206] magnetic information storage,[203] nonvolatile magnetic random access memory (MRAM) [207] and magnetic refrigeration systems.[208] Magnetic nanoparticles have been applied in biological and biomedical assays and devices.[209,210] Nanoparticles can be used as efficient diagnostic tools in magnetic resonance imaging, magnetic separation of biological targets,[211] and as therapeutic agents for hyperthermic tumor treatments,[212,213] drug, and gene delivery.[214, 215] The size, shape and properties of magnetic nanoparticles are critical characteristics for designing applications.

Several strategies have been used to prepare assemblies of magnetic nanoparticles onto planar substrates.[207,216,217] Forces such as hydrogen-bonding,[218] covalent bonding,[219] as well as electrostatic and van der Waals interactions[220] are used to direct the assembly of nanoparticles.[221] Chemical patterning or surface electrostatic interactions have been applied to create specifically patterned nanoparticle assemblies. Techniques that were used to deposit magnetic nanoparticles on substrates include gas phase deposition,[222] layer-by-layer assembly,[223] Langmuir-Blodgett techniques,[224, 225, 226] microcontact printing,[227] capillary filling,[227] drop-casting,[220] and self-assembly at the liquid-air interface.[228] Magnetic interactions were also used to assemble magnetic nanoparticles, in which an externally applied magnetic field was applied to control the local arrangement.[229, 230, 231] Structural patterns such as chains, columns and labyrinths have been observed using magnetic field assisted methods.[232] Nanolithography technologies, such as e-beam

lithography,[233, 234] X-ray lithography,[235] optical lithography[236, 237] and scanning probe-based lithography[238, 239] also have been used to pattern magnetic nanoparticles.

Particle lithography is based on simple steps of conventional bench chemistry procedures of mixing, centrifuging, evaporation and rinsing to produce arrays of Fe_3O_4 nanoparticles. For particle lithography, monodisperse, spherical particles are used either as a mask or a template to produce nanostructures. Particle lithography is a facile approach for patterning metal nanoparticles.[92,150] Particle lithography has been applied to generate arrays of nanostructures of polymers,[240, 241] proteins,[242,243] metals,[244, 245, 246, 247, 248] quantum dots,[249, 250, 150] and self-assembled monolayers.[251,252]

In our experiments with "two-particle" lithography our experimental strategy was to construct periodic arrays of Fe_3O_4 nanoparticle clusters as a well-defined test platform for scanning probe studies.[150] Characterizations were accomplished using magnetic sample modulation (MSM), a hybrid imaging mode of atomic force microscopy (AFM).[92] The instrument configuration for MSM-AFM has been applied for selective magnetic imaging of electrolessly deposited iron-oxide capped nanostructures formed on organosilane nanopatterns [92] and for imaging nanostructures of ferritin.[94] Relatively monodisperse, hydrophilic, and single-crystalline ferrite microspheres were prepared by a solvothermal reduction method. Magnetic Fe_3O_4 particles with a size range of 70-135 nm were synthesized via a solvothermal method by modified reduction reactions between $FeCl_3$ and ethylene glycol. The arrays of Fe_3O_4 nanoparticles on glass substrate exhibit periodicity spanning micrometer-sized areas. The density and surface coverage of the arrays can be controlled by selection of the diameters of the mesospheres. Structural latex masks with a diameter of 1 μm were used for patterning to pattern Fe_3O_4 nanoparticles on a glass substrate.

4.2 Experimental Details

4.2.1 Materials and Reagents.

Glass substrates were cleaned by immersion in piranha solution for 1 h. Piranha solution is a mixture of sulfuric acid (96%, EMD Chemical Inc., Gibbstown, NJ) and hydrogen peroxide (30%, Sigma-Aldrich) at a ratio of 3:1 (v/v). Piranha solution is highly corrosive and should be handled carefully. Monodisperse latex mesospheres, 1 μm in diameter (Thermo Scientific, Waltham, MA) were used as received.

4.2.2 Preparation of Fe_3O_4 Nanoparticles

Our modified recipe of the procedure reported by Deng *et al* [253] yielded spherical Fe_3O_4 nanoparticles with diameters of 100, 125, 135, nm. This involved charging a round bottom flask with iron chloride (1.4 g, $FeCl_3.6H_2O$) and sodium acetate (3.6 g) sequentially dissolved in 15 mL of ethylene glycol. Addition of sodium acetate rapidly turned the orange $FeCl_3.6H_2O$ solution to brown color. The solution was stirred for an additional 30 min and then injected at once into a round-bottomed flask containing a vigorously stirred solution of PVP (0.40 g) in 35 mL of ethylene glycol heated to 180 °C. The mixture was then vigorously stirred at 180 °C for 4–24 hours during which a black precipitate was obtained. The black precipitate was washed multiple times with ethanol, Milli-Q water and dried under vacuum at room temperature. Agitation (stirrer speed), temperature, and reaction time were the process parameters that were varied to obtain Fe_3O_4 nanospheres of desired diameters.

4.2.3 Procedure for "Two-particle" Lithography

The key steps for "two-particle" lithography are illustrated in Figure 4.1. First, an aqueous solution of monodisperse latex was centrifuged at17000 rpm for 10 min to remove surfactants or other stabilizers. The pellet was then re-suspended in deionized water for one rinsing cycle by

centrifugation. Next, the rinsed pellet of mesospheres was resuspended in the desired volume of an aqueous solution containing Fe_3O_4 nanoparticles. A small volume (20 µL) of the mixture of nanoparticles and mesospheres in a given ration were deposited onto the cleaned glass substrate. The droplet of sample was then dried in air at room temperature for 12 h. After the samples were dried, the larger mesospheres were removed by gently pressing a piece of scotch tape onto the glass substrate. In the tape removal step, the nanoparticles remained attached to the surface in patterned arrangements that conform to the periodicity of the latex surface mask.

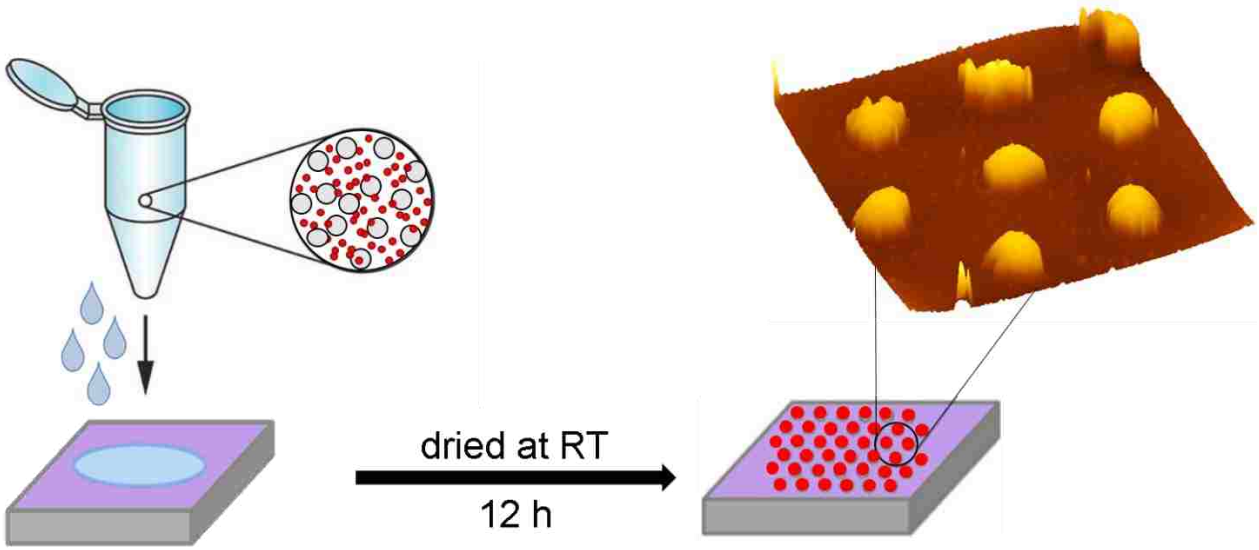

Figure 4.1 Basic steps for preparing Fe_3O_4 nanoparticles using "two-particle" lithography. A) A mixture of latex spheres and nanoparticles was deposited on the substrate; B) After drying the sample, the mask was removed with scotch tape to reveal a periodic arrangement of Fe_3O_4 nanoparticle clusters

4.2.4 Atomic Force Microscopy

Samples were characterized with a model 5500 scanning probe microscope (Keysight Technologies, Santa Rosa, CA). Nonconductive V-shaped cantilevers made of silicon nitride having low force constants ranging from 0.1 to 0.5 Nm^{-1} (Veeco Probes, Santa Barbara, CA) were used for imaging samples. A plastic nosecone assembly without metal components and the magnetic AC mode (MAC-mode) sample plate was used for mounting probes on the scanner for

MSM-AFM studies. Images were processed using Gwyddion, a freely available open source software supported by the Czech Metrology Institute.[194]

The MSM setup is a hybrid of contact-mode AFM combined with selective actuation of magnetic samples (Figure 4.2).[92] First, the sample surface is scanned in contact-mode without applying the electromagnetic field, for acquiring conventional topography and lateral force images. For the second pass on the same area, an alternating electromagnetic field was applied by the sample stage with average field strengths ranging between 0.01 to 0.2 T. Only the magnetic domains are driven to vibrate when an alternating electromagnetic field is applied to samples which provides selective contrast for areas that are in motion. The vibration of samples is detected with amplitude and phase signals, which are acquired simultaneously with MSM-topography.

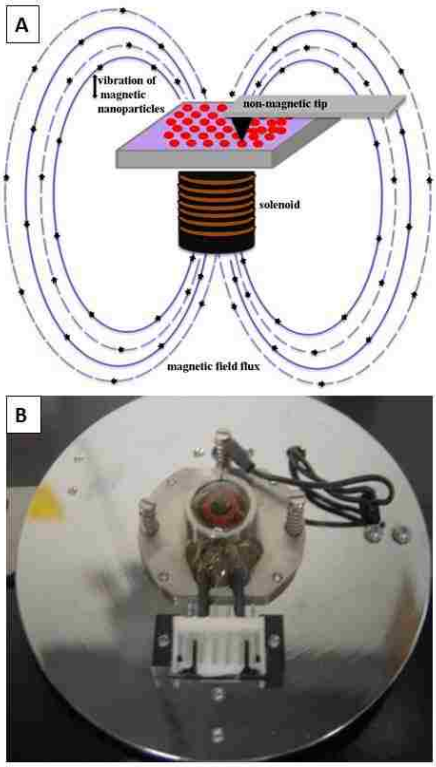

Figure 4.2 Instrument set-up for magnetic sample modulation AFM. [A] An AC magnetic field induces actuation of magnetic nanoparticles on a surface. A soft, nonmagnetic tip is operated in contact mode as a force and motion sensor. [B] Photo of solenoid embedded with the sample plate.

4.3 Results and Discussion

4.3.1 Nanopatterns of Fe_3O_4 Nanoparticles Visualized with Contact-Mode AFM

Initial characterizations of the array of Fe_3O_4 nanoparticle clusters were acquired using contact-mode AFM (Figure 4.3). Clusters of Fe_3O_4 nanoparticles as well as individual nanoparticles in a few areas between the clusters furnish a test sample for evaluating size effects (Figure 4.3A). Adventitiously, the shapes and locations of the clusters of Fe_3O_4 nanoparticles as well as smaller individual Fe_3O_4 nanoparticles are revealed in the simultaneously acquired lateral force image (Figure 4.3B). The presence of the smaller nanoparticles in areas between the clusters is more clearly viewed in the lateral force frames which distinctly reveal the edges and shapes of the smaller nanoparticles. The height of three nanoparticle clusters measured using the substrate as a baseline is plotted in Figure 4.3C, referencing white line in Figure 3A. The average height of the nanoparticle clusters measured 78 ± 2 nm from an average of 100 data points. Each Fe_3O_4nanoparticle cluster is spaced approximately 1 µm apart, corresponding to the size of the latex mesospheres used for patterning (1 µm diameter).

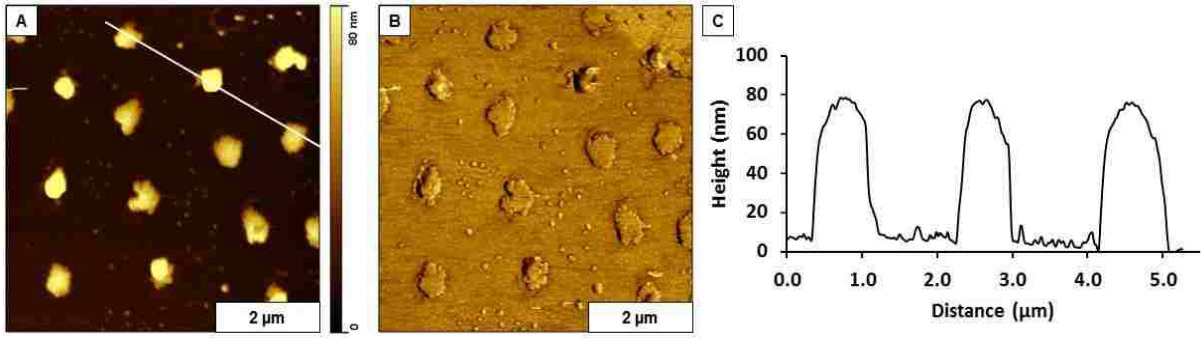

Figure 4.3 Clusters of magnetic Fe_3O_4 nanoparticles prepared on a glass substrate viewed with contact mode AFM images. A) Arrangement of clusters of nanoparticles viewed with the topography channel; B) corresponding lateral force image; C) Height profile for white line in A.

4.3.2 Selective Actuation of Magnetic Samples using MSM-AFM

The test sample of nanopatterned clusters and Fe_3O_4 nanoparticles were imaged with and without an applied electromagnetic field, as shown in Figure 4.4. Simultaneously acquired topography, MSM-amplitude and MSM-phase frames, respectively are presented for a 6 × 6 μm2 area of the surface (Figure 4.4). When the oscillating magnetic field was turned off there are no features or shapes evident in the amplitude or phase channels (top row, Figures 4.4A, 4.4B, 4.4C).

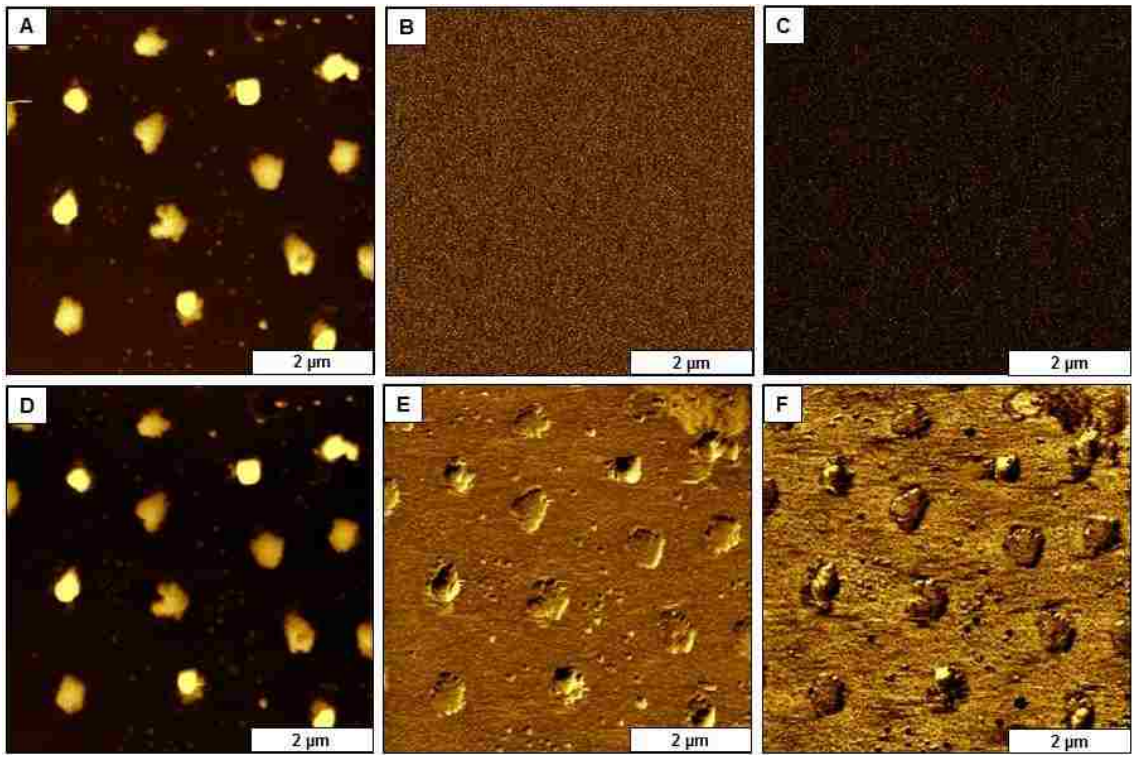

Figure 4.4 Clusters of Fe3O4 nanoparticles prepared on glass imaged with and without an applied electromagnetic field using MSM-AFM. The top row were acquired in the absence of magnetic field: [A] Topography image; simultaneously acquired [B] amplitude; and [C] phase image. The bottom row of frames were acquired with and applied AC electromagnetic field: [D] Topography image; [E] corresponding MSM-amplitude; and [F] MSM-phase channels.

In the absence of an external magnetic field the nanoparticles do not vibrate. During the scan when AC current is applied to the solenoid to generate the flux of a magnetic field, the magnetic areas on the sample are induced to vibrate. When the AFM tip comes into contact with a vibrating area

of the sample, the probe is driven to vibrate. The vibration of the tip is monitored using a lock-in amplifier to generate images of the changes in the amplitude and phase motion of the AFM probe. Topography images are acquired concurrently with MSM amplitude and phase images (Figures 4.4D, 4.4E, 4.4F). For this example, comparing the topography frames with (Figure 4.4A) and without (Figure 4.4D) an applied field does not reveal any discernable changes. The two frames are mostly identical.

4.3.3 Dynamic Changes in MSM-AFM Images with Frequency

A frequency sweep can be acquired with MSM-AFM by placing the AFM tip directly on a vibrating nanoparticle cluster and measuring the amplitude as the frequency is ramped (Figure 4.5). When the probe is placed on the substrate in areas where there is no magnetic sample, the frequency sweep is a flat line. The frequencies we selected include the prominent resonance peak at 60.04 kHz and the shoulder peak shown at 56.48 kHz. No prominent peaks were detected for the region of 100-600 kHz. The profile of a single resonance suggests that the nanocluster is vibrating as a solid block rather than having multiple vibrating domains.

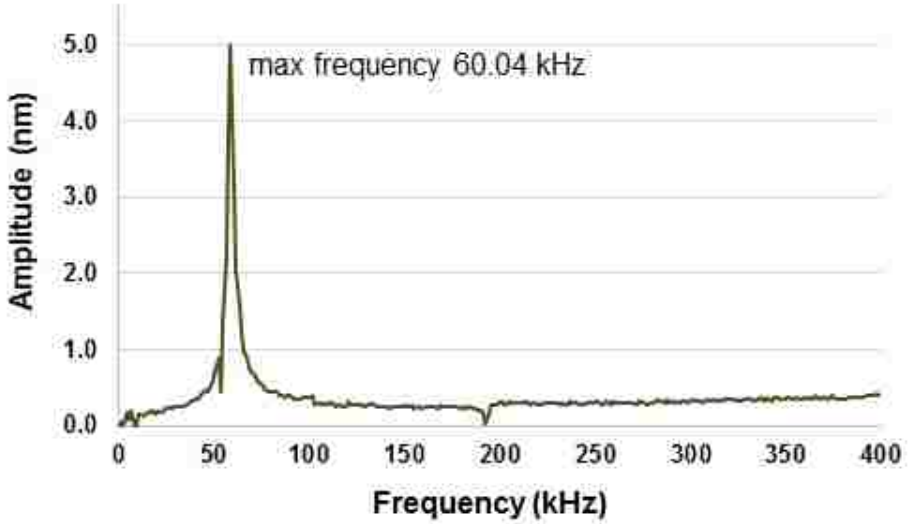

Figure 4.5 Frequency sweep acquired by placing the AFM probe on a vibrating Fe_3O_4 nanocluster.

Experimental parameters such as the driving frequency and applied field strength for MSM imaging can be optimized based on the information obtained from frequency sweeps. As the samples are scanned with MSM, parameters such as the field strength and driving frequency can be used to optimize image resolution.

Images acquired with MSM-AFM using two selected frequencies, with an applied magnetic field strength of ~0.12 T are shown in Figure 4.6. Changing the frequency at selected intervals during data acquisition of an MSM-AFM image enables a side-by-side comparison of the vibrating nanoparticle clusters with chosen parameters (Figure 4.6A). For the top row of images (Figure 4.6A) the frequencies were changed in situ without halting data acquisition. The topography frame of Figure 4.6A does not show any noticeable changes as the frequency parameter is changed in situ, however, the simultaneously acquired amplitude and phase channels reveal distinct differences as the frequency is increased to 56.48 and 60.04 kHz. At frequency 0 kHz there was no vibration of the Fe_3O_4 nanoparticle clusters, shown in the upper portion of the frames of Figure 4.6A. The upper part of the amplitude and phase frames do not display the shapes or locations of the nanoparticle clusters which are apparent in the corresponding topography image. Mapping of magnetic domains was initiated when the frequency was increased to 56.48 kHz, as evident in the middle portion of the MSM-amplitude and MSM-phase images of Figure 4.6A. As the frequency was changed incrementally during image acquisition with MSM-AFM, the vibrational amplitude of the sample changed accordingly. Interestingly, the much smaller individual nanoparticles also become visible at higher frequency in the MSM frames. For the frames acquired at 56.48 kHz improvements in the resolution of the phase image (right panel) are apparent with clearly defined edges and shapes. Thus, the resolution of phase images does not necessarily improve with higher amplitude response. At the resonance frequency of 60.04 kHz,

magnetic features are apparent for both the amplitude and phase frames shown in the lower portion of Figure 4.6A. In the frequency sweep of Figure 4.5, the maximum amplitude response was detected at 60.04 kHz. Correspondingly, the best resolution for the amplitude frames was detected at the resonance frequency. This indicates that at resonance, the probe detected a greater displacement attributable to stronger sample vibration.

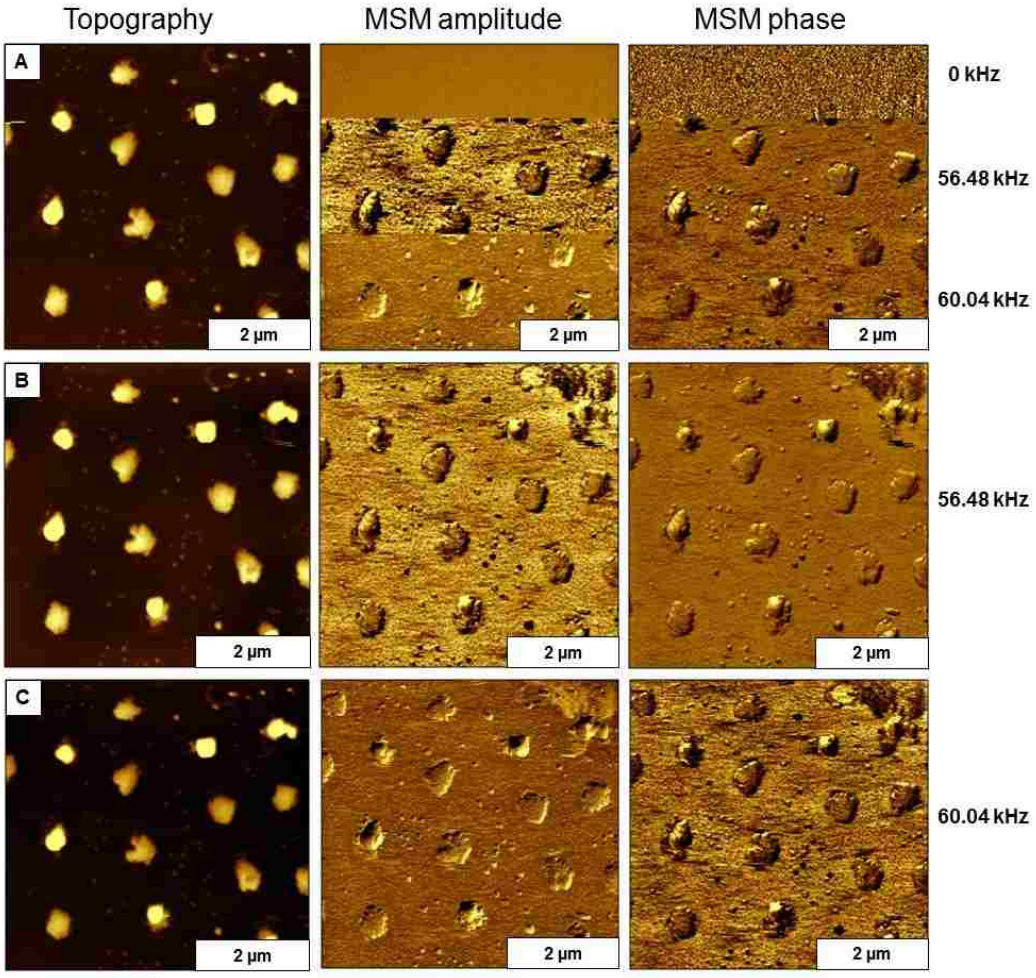

Figure 4.6 Magnetic nanoparticle clusters of Fe_3O_4 prepared on glass imaged at selected frequencies. [A] The top row indicates changes for images as the frequency was changed in situ. From left to right, topography, amplitude and phase channels are presented. [B] Frames in the center row were acquired at a frequency of 56.48 kHz; [C] Images in the bottom row were acquired at the resonance frequency of 60.04 kHz.

Images of the sample of Fe_3O_4 nanoparticle clusters acquired with the magnetic field actuated at a single frequency throughout the entire scan are shown in Figures 4.6B-4.6C. Note that the topography frames (left images) are indistinguishable at the selected frequency parameters. The tip is driven to vibrate when it encounters vibrating Fe_3O_4 nanoparticle clusters. Changes in the motion of the tip-surface contact are compared to the driving signal and are plotted in amplitude and phase channels to generate surface maps of magnetic response (Figures 4.6B and 4.6C), which demonstrates the mapping capabilities of the MSM-AFM imaging mode. Amplitude and phase channels are compared side-by-side for the chosen frequencies in the center and left hand columns, respectively. In these examples, the fine details of small adsorbates are revealed, to detect these features in the topography frames would require image processing with saturated color scales.

4.3.4 Effect of Field Strength for MSM-AFM Images

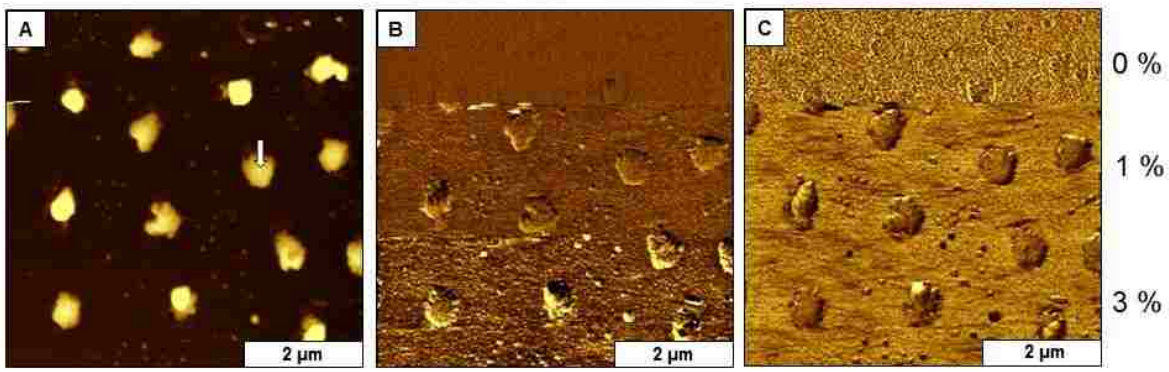

Figure 4.7 Changes in MSM frequency spectra as the strengths of the applied electromagnetic field varied. A) White arrow in topography image showing the AFM tip placed on a Fe_3O_4nanoparticle cluster; B) corresponding MSM amplitude and; C) MSM phase channels.

Example topography, amplitude, and phase images acquired concurrently with the magnetic field turned on are presented in Figure 4.7. The tip-sample resonance frequency was maintained at 60.04 kHz during acquisition. Within a single scan, the magnetic field strength was changed from 0 T, 0.05 T, and 0.12 T respectively, without halting data acquisition (Figure 4.7A). The topography frame in Figure 4.7A, does not reveal significant changes with increasing field strengths. The

MSM amplitude (Figure 4.7B) and MSM phase (Figure 4.7C) channels sensitively reveal the location of Fe_3O_4 nanoparticles and clusters relative to the glass substrate. When the field strength was 0 T, no vibrations were detected by the tip shown in the upper region of Figures 4.7B and 7C. However, as the field strength was increased to 0.05 T, the locations of vibrating nanoparticles become apparent. As the field strength was further increased to 0.12 T, the amplitude of the vibrating nanoparticle clusters increases to show sharper contrast in the lower part of the MSM amplitude and MSM phase images. As the magnetic field strength was increased, smaller individual nanoparticles surrounding the clusters are detected in the MSM amplitude and phase channels.

We observed that as nanoparticles decrease in size, a larger field strength is required to induce vibration. Smaller nanoparticles may not be detected at the lower field strengths, depending on the nature of surface attachment. For strongly bonded nanoparticles or samples with embedded nanoparticles, vibration cannot be detected with MSM-AFM. Interestingly, nanoparticles that are barely discernable in the topography image are readily visualized in the MSM amplitude and phase frames.

The capability of MSM to map magnetic domains with dynamic parameters is demonstrated in Figure 4.7. Information about the location and relative vibrational response of the magnetic domains can be acquired. As the magnetic field strength is ramped particles can be shaken loose from the substrate and displaced with the scanning motion of the tip as it is operated in contact-mode. Therefore, in conducting experiments we begin with lower field strengths and increase the parameter to evaluate an optimum setting. Phase images present the fine details of surface shapes, such as for defining the boundaries and lateral dimensions of nanoparticle cluster.

Depending on the size of the nanoparticles, smaller nanomaterials can be detected at higher field strengths, as revealed in the MSM-amplitude and MSM-phase channels.

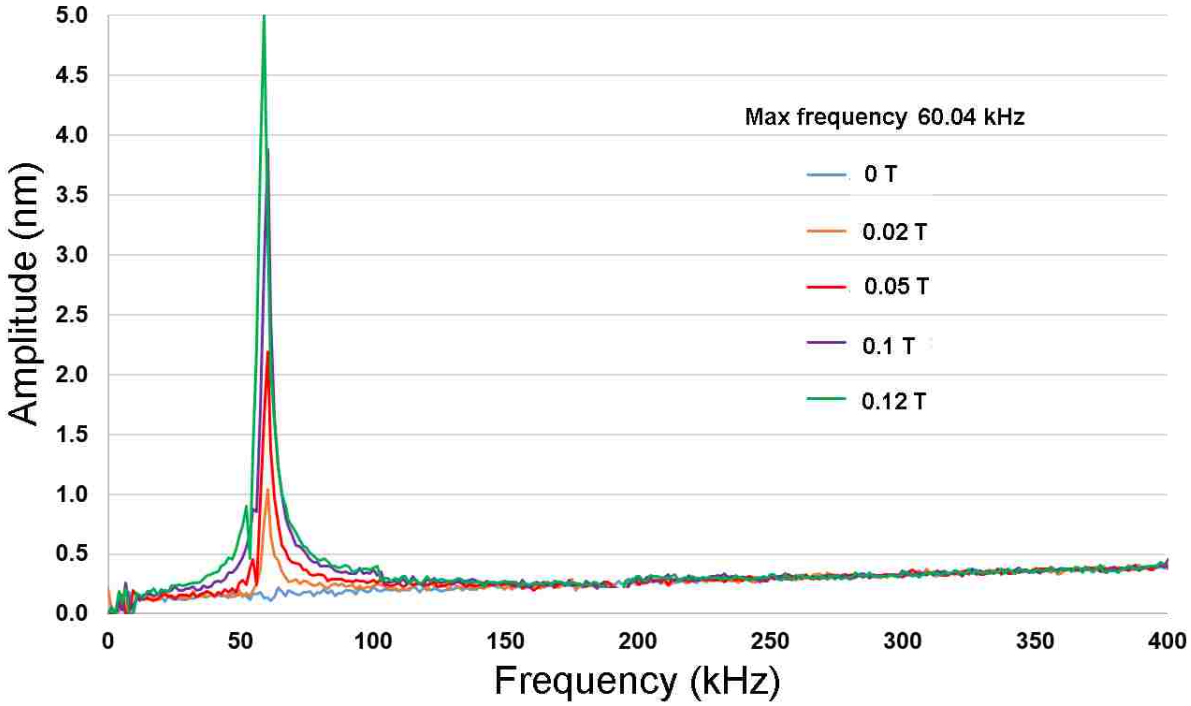

Figure 4.8 Overlay of MSM frequency spectra as the field strength was increased.

A comparison of frequency profiles acquired in a selected sample location when the probe was placed directly on top of a nanoparticle cluster is shown in Figure 4.8. Essentially, the AFM tip was parked on a single nanoparticle cluster and frequency spectra were acquired at selected field strengths. An overlay of the amplitude vs frequency spectra with incremental changes in the field strength with neatly symmetric peak profiles demonstrate that the primary resonance frequency. A prominent resonance peak was observed between 50 and 70 kHz. (The peak location is 60 kHz) does not shift. The amplitude axis corresponds to the z displacement of the AFM tip, and was ranged from 0 to 5.0 nm for this experiment. Typically, the spectra will reveal a prominent resonance peak and multiple smaller peaks, depending on the complexity of the sample. The amplitude peak height increased proportionately as the field strength was ramped. An amplitude

response of 2.3 nm was observed when the applied field was set at 0.05 T and a higher amplitude response of 5.0 nm was obtained when the magnetic strength was increased to 0.12 T. Sufficient force must be applied to the tip to hold the probe in contact with the vibrating nanoparticle.

4.4 Conclusion

Clusters of magnetic Fe_3O_4 nanoparticles were patterned on glass substrates and studied with MSM-AFM. Information of the location of individual magnetic domains can be detected with MSM-AFM, the nanoparticles vibrate in response to the flux of an AC generated electromagnetic field generated below the sample stage. Spectra of the characteristic resonance frequencies of the Fe_3O_4 nanoparticle clusters can be acquired. Dynamic studies with MSM-AFM show an increase in the vibration amplitude with an increase in the magnetic field strength. The resonance profiles of the frequency spectra are not identical for nanoparticles of different sizes, further experiments are being designed to systematically evaluate the size-dependent resonance profiles for nanoparticles according to changes in size and composition. Future studies include imaging mixtures of Fe_3O_4 nanoparticles with differences in composition and size to evaluate the resonance signatures in response to an applied magnetic field. These studies will lead to new information about how individual and clusters of magnetic nanoparticles respond to the flux of an AC electromagnetic field.

CHAPTER 5: CONCLUSIONS AND FUTURE PROSPECTUS

Chemically patterned surfaces were fabricated using a combination of molecular self-assembly and particle lithography to generate billions of nanopatterns of organosilane self-assembled monolayers (SAMs). The nanoscale patterns can be tailored to attach nanoscale materials by selecting the designed surface chemistry. Investigations of the solvent responsive properties of OTS multilayers was achieved using contact mode AFM imaging in liquid. Studies of surface properties such as wettability or swelling that change upon stimulation by heat, light, pH, electric field, temperature, or solvents are helpful in development of responsive materials. Responsive surfaces are commonly prepared using SAMs or polymer thin films.

Chemically functionalized surfaces prepared with OTS multilayers provide a well-defined 3D interface of spatially confined nanostructures with nanoscale dimensions for studying the effect of solvents for producing changes in surface morphology. High-resolution images acquired with AFM provided a means to measure and quantify the swelling of nanopatterned surfaces at nanoscale dimensions. Future studies will be designed for *in-situ* investigation of the stimuli-responsive nature of nanostructures in response to pH, light and temperature. Measurements with AFM provide a framework for *in situ* studies of stimuli responsive behavior of organic thin film materials.

Magnetic nanoparticles have potential as building blocks of the future nanoscale devices, however, development of strategies for processing nanoparticles has become a challenge. Application of self-assembly for patterning nanoparticles is a practical approach for high-throughput manufacturing. Magnetic properties and structural effects can be studied at the level of individual nanoparticles using advanced modes of AFM.

Magnetic sample modulation AFM (MSM-AFM) provides capabilities for imaging magnetic nanoparticles. Magnetic nanoparticles with a dimensions as small as 0.8 nm to as large as magnetic clusters of 100 nm nanoparticles have been detected with MSM-AFM. Periodic arrays of magnetic iron oxide nanoparticles prepared using an approach of "two-particle" lithography method were used as test platforms for dynamic experiments with MSM-AFM. Protocols were developed to observe and quantify the vibrational response of the magnetic nanoparticles with *in-situ* modulation of parameters such as the frequency and magnetic field strength of the applied electromagnetic field. Sensitively mapping the distribution and locations of magnetic nanoparticles provided a detection mechanism using the MSM-AFM mode. Dynamic measurements with MSM-AFM showed an increase in the vibration amplitude of magnetic iron oxide nanoparticle clusters with increases in the magnetic field strength within the patterned Fe_3O_4 nanoparticles. Future studies include imaging mixtures of magnetic nanoparticles with mixed compositions and sizes to test the differences in resonance signatures in response to an applied magnetic field. Studies with MSM-AFM will provide information about how magnetic nanoparticles respond to an externally applied AC electromagnetic field.

REFERENCES

1. Rosi, N. L.; Mirkin, C. A., Nanostructures in biodiagnostics. *Chemical Reviews* **2005,** *105* (4), 1547-1562.

2. Barth, J. V.; Costantini, G.; Kern, K., Engineering atomic and molecular nanostructures at surfaces. *Nature* **2005,** *437* (7059), 671-679.

3. Theobald, J. A.; Oxtoby, N. S.; Phillips, M. A.; Champness, N. R.; Beton, P. H., Controlling molecular deposition and layer structure with supramolecular surface assemblies. *Nature* **2003,** *424* (6952), 1029-1031.

4. Link, S.; El-Sayed, M. A., Spectral properties and relaxation dynamics of surface plasmon electronic oscillations in gold and silver nanodots and nanorods. *The Journal of Physical Chemistry B* **1999,** *103* (40), 8410-8426.

5. Gimzewski, J. K.; Joachim, C., Nanoscale science of single molecules using local probes. *Science* **1999,** *283* (5408), 1683-1688.

6. Alivisatos, A. P., Semiconductor clusters, nanocrystals, and quantum dots. *Science* **1996,** *271* (5251), 933-937.

7. Cui, Y.; Wei, Q.; Park, H.; Lieber, C. M., Nanowire nanosensors for highly sensitive and selective detection of biological and chemical species. *Science* **2001,** *293* (5533), 1289-1292.

8. Lu, A.-H.; Salabas, E. L.; Schüth, F., Magnetic nanoparticles: Synthesis, protection, functionalization, and application. *Angewandte Chemie International Edition* **2007,** *46* (8), 1222-1244.

9. Haes, A. J.; Van Duyne, R. P., A nanoscale optical biosensor: Sensitivity and selectivity of an approach based on the localized surface plasmon resonance spectroscopy of triangular silver nanoparticles. *Journal of the American Chemical Society* **2002,** *124* (35), 10596-10604.

10. McFarland, A. D.; Van Duyne, R. P., Single silver nanoparticles as real-time optical sensors with zeptomole sensitivity. *Nano Letters* **2003,** *3* (8), 1057-1062.

11. Kempa, K.; Kimball, B.; Rybczynski, J.; Huang, Z. P.; Wu, P. F.; Steeves, D.; Sennett, M.; Giersig, M.; Rao, D. V. G. L. N.; Carnahan, D. L.; Wang, D. Z.; Lao, J. Y.; Li, W. Z.; Ren, Z. F., Photonic crystals based on periodic arrays of aligned carbon nanotubes. *Nano Letters* **2003,** *3* (1), 13-18.

12. Han, J.; Craighead, H. G., Separation of long dna molecules in a microfabricated entropic trap array. *Science* **2000,** *288* (5468), 1026-1029.

13. Landskron, K.; Hatton, B. D.; Perovic, D. D.; Ozin, G. A., Periodic mesoporous organosilicas containing interconnected [si(ch2)]3 rings. *Science* **2003,** *302* (5643), 266-269.

14. Orisaka, S.; Minobe, T.; Uchihashi, T.; Sugawara, Y.; Morita, S., The atomic resolution imaging of metallic Ag(111) surface by noncontact atomic force microscope. *Applied Surface Science* **1999,** *140* (3–4), 243-246.

15. Drake, B.; Prater, C.; Weisenhorn, A.; Gould, S.; Albrecht, T.; Quate, C.; Cannell, D.; Hansma, H.; Hansma, P., Imaging crystals, polymers, and processes in water with the atomic force microscope. *Science* **1989,** *243* (4898), 1586-1589.

16. Hansma, H. G.; Vesenka, J.; Siegerist, C.; Kelderman, G.; Morrett, H.; Sinsheimer, R. L.; Elings, V.; Bustamante, C.; Hansma, P. K., Reproducible imaging and dissection of plasmid dna under liquid with the atomic force microscope. *Science* **1992,** *256* (5060), 1180-1184.

17. Lyubchenko, Y. L.; Shlyakhtenko, L. S., Visualization of supercoiled DNA with atomic force microscopy in situ. *Proceedings of the National Academy of Sciences* **1997,** *94* (2), 496-501.

18. Kasas, S.; Thomson, N. H.; Smith, B. L.; Hansma, H. G.; Zhu, X.; Guthold, M.; Bustamante, C.; Kool, E. T.; Kashlev, M.; Hansma, P. K., Escherichia coli rna polymerase activity observed using atomic force microscopy. *Biochemistry* **1997,** *36* (3), 461-468.

19. Fritz, J.; Anselmetti, D.; Jarchow, J.; Fernàndez-Busquets, X., Probing single biomolecules with atomic force microscopy. *Journal of Structural Biology* **1997,** *119* (2), 165-171.

20. A-Hassan, E.; Heinz, W. F.; Antonik, M. D.; D'Costa, N. P.; Nageswaran, S.; Schoenenberger, C. A.; Hoh, J. H., Relative microelastic mapping of living cells by atomic force microscopy. *Biophysical Journal* **1998,** *74* (3), 1564-1578.

21. Andrea, A.; Paolo, F., AFM: a versatile tool in biophysics. *Measurement Science and Technology* **2005,** *16* (6), R65.

22. van der Vegte, E. W.; Hadziioannou, G., Scanning force microscopy with chemical specificity: An extensive study of chemically specific tip−surface interactions and the chemical imaging of surface functional groups. *Langmuir* **1997,** *13* (16), 4357-4368.

23. Hamers, R. J., Scanned probe microscopies in chemistry. *The Journal of Physical Chemistry* **1996,** *100* (31), 13103-13120.

24. Hansma, P.; Elings, V.; Marti, O.; Bracker, C., Scanning tunneling microscopy and atomic force microscopy: application to biology and technology. *Science* **1988,** *242* (4876), 209-216.

25. Hörber, J. K. H.; Miles, M. J., Scanning probe evolution in biology. *Science* **2003,** *302* (5647), 1002-1005.

26. Leclère, P.; Lazzaroni, R.; Brédas, J. L.; Yu, J. M.; Dubois, P.; Jérôme, R., Microdomain morphology analysis of block copolymers by atomic force microscopy with phase detection imaging. *Langmuir* **1996,** *12* (18), 4317-4320.

27. Loos, J., The art of spm: Scanning probe microscopy in materials science. *Advanced Materials* **2005,** *17* (15), 1821-1833.

28. Samori, P., Scanning probe microscopies beyond imaging. *Journal of Materials Chemistry* **2004,** *14* (9), 1353-1366.

29. Binnig, G.; Rohrer, H.; Gerber, C.; Weibel, E., Tunneling through a controllable vacuum gap. *Applied Physics Letters* **1982,** *40* (2), 178-180.

30. Binnig, G.; Quate, C. F.; Gerber, C., Atomic Force Microscope. *Physical Review Letters* **1986,** *56* (9), 930-933.

31. Radmacher, M.; Tillamnn, R.; Fritz, M.; Gaub, H., From molecules to cells: imaging soft samples with the atomic force microscope. *Science* **1992,** *257* (5078), 1900-1905.

32. Döppenschmidt, A.; Kappl, M.; Butt, H.-J., Surface properties of ice studied by atomic force microscopy. *The Journal of Physical Chemistry B* **1998,** *102* (40), 7813-7819.

33. Hansma, H. G.; Revenko, I.; Kim, K.; Laney, D. E., Atomic force microscopy of long and short double-stranded, single-stranded and triple-stranded nucleic acids. *Nucleic Acids Research* **1996,** *24* (4), 713-720.

34. Le Grimellec, C.; Lesniewska, E.; Giocondi, M. C.; Finot, E.; Vié, V.; Goudonnet, J. P., Imaging of the surface of living cells by low-force contact-mode atomic force microscopy. *Biophysical Journal* **1998,** *75* (2), 695-703.

35. Franz, V.; Butt, H.-J., Confined liquids: Solvation forces in liquid alcohols between solid surfaces. *The Journal of Physical Chemistry B* **2002,** *106* (7), 1703-1708.

36. Hartley, P. G.; Scales, P. J., Electrostatic properties of polyelectrolyte modified surfaces studied by direct force measurement. *Langmuir* **1998,** *14* (24), 6948-6955.

37. Miklavcic, S. J.; Thulin, E.; Jönsson, B., Forces between macroscopic surfaces in solutions of calcium binding proteins. *The Journal of Physical Chemistry* **1996,** *100* (13), 5554-5561.

38. Biggs, S., Non-equilibrium interaction forces between adsorbed polymer layers. *Journal of the Chemical Society, Faraday Transactions* **1996,** *92* (15), 2783-2789.

39. Braithwaite, G. J. C.; Howe, A.; Luckham, P. F., Interactions between poly(ethylene oxide) layers adsorbed to glass surfaces probed by using a modified atomic force microscope. *Langmuir* **1996,** *12* (17), 4224-4237.

40. Florin, E. L.; Moy, V. T.; Gaub, H. E., Adhesion forces between individual ligand-receptor pairs. *Science (New York, N.Y.)* **1994,** *264* (5157), 415-417.

41. Hinterdorfer, P.; Baumgartner, W.; Gruber, H. J.; Schilcher, K.; Schindler, H., Detection and localization of individual antibody-antigen recognition events by atomic force microscopy. *Proceedings of the National Academy of Sciences of the United States of America* **1996,** *93* (8), 3477-3481.

42. Binnig, G.; Rohrer, H.; Gerber, C.; Weibel, E., 7 \ifmmode\times\else\texttimes\fi{} 7 Reconstruction on Si(111) Resolved in Real Space. *Physical Review Letters* **1983,** *50* (2), 120-123.

43. Skomski, D.; Abb, S.; Tait, S. L., Robust surface nano-architecture by alkali–carboxylate ionic bonding. *Journal of the American Chemical Society* **2012,** *134* (34), 14165-14171.

44. Besenbacher, F.; Thostrup, P.; Salmeron, M., The structure and reactivity of surfaces revealed by scanning tunneling microscopy. *MRS Bulletin* **2012,** *37* (07), 677-681.

45. Goksu, E. I.; Vanegas, J. M.; Blanchette, C. D.; Lin, W.-C.; Longo, M. L., AFM for structure and dynamics of biomembranes. *Biochimica et Biophysica Acta (BBA) - Biomembranes* **2009,** *1788* (1), 254-266.

46. Hilal, N.; Johnson, D.; Bowen, W. R.; Williams, P. M., Measurement of particle and surface interactions using force microscopy. In *Atomic Force Microscopy in Process Engineering*, Bowen, W. R.; Hilal, N., Eds. Butterworth-Heinemann: Oxford, 2009; pp 31-80.

47. Hilal, N.; Bowen, W. R.; Johnson, D.; Yin, H., AFM and development of (bio)fouling-resistant membranes. In *Atomic Force Microscopy in Process Engineering*, Bowen, W. R.; Hilal, N., Eds. Butterworth-Heinemann: Oxford, 2009; pp 139-171.

48. Koutsos, V., Atomic force microscopy and polymers on surfaces. In *Atomic Force Microscopy in Process Engineering*, Bowen, W. R.; Hilal, N., Eds. Butterworth-Heinemann: Oxford, 2009; pp 225-244.

49. Albrecht, T. R.; Akamine, S.; Carver, T. E.; Quate, C. F., Microfabrication of cantilever styli for the atomic force microscope. *Journal of Vacuum Science & Technology A* **1990,** *8* (4), 3386-3396.

50. Hafner, J. H.; Cheung, C. L.; Woolley, A. T.; Lieber, C. M., Structural and functional imaging with carbon nanotube AFM probes. *Progress in Biophysics and Molecular Biology* **2001,** *77* (1), 73-110.

51. Devasia, S.; Eleftheriou, E.; Moheimani, S. O. R., A survey of control issues in nanopositioning. *Control Systems Technology, IEEE Transactions on* **2007,** *15* (5), 802-823.

52. Moheimani, S. O. R., Invited Review Article: Accurate and fast nanopositioning with piezoelectric tube scanners: Emerging trends and future challenges. *Review of Scientific Instruments* **2008,** *79* (7), 071101.

53. Allen, M. J.; Hud, N. V.; Balooch, M.; Tench, R. J.; Siekhaus, W. J.; Balhorn, R., Tip-radius-induced artifacts in AFM images of protamine-complexed DNA fibers. *Ultramicroscopy* **1992,** *42–44, Part 2* (0), 1095-1100.

54. Tabet, M. F.; Urban, F. K., Deconvolution of tip affected atomic force microscope images and comparison to Rutherford backscattering spectrometry. *Journal of Vacuum Science & Technology B* **1997,** *15* (4), 800-804.

55. Markiewicz, P.; Goh, M. C., Simulation of atomic force microscope tip–sample/sample–tip reconstruction. *Journal of Vacuum Science & Technology B* **1995,** *13* (3), 1115-1118.

56. Martin, Y.; Wickramasinghe, H. K., Magnetic imaging by ‘‘force microscopy’’ with 1000 Å resolution. *Applied Physics Letters* **1987,** *50* (20), 1455-1457.

57. Mate, C. M.; McClelland, G. M.; Erlandsson, R.; Chiang, S., Atomic-scale friction of a tungsten tip on a graphite surface. *Physical Review Letters* **1987,** *59* (17), 1942-1945.

58. Maivald, P.; Butt, H. J.; Gould, S. A. C.; Prater, C. B.; Drake, B.; Gurley, J. A.; Elings, V. B.; Hansma, P. K., Using force modulation to image surface elasticities with the atomic force microscope. *Nanotechnology* **1991,** *2* (2), 103.

59. Kelley, T. W.; Granstrom, E.; Frisbie, C. D., Conducting probe atomic force microscopy: A characterization tool for molecular electronics. *Advanced Materials* **1999,** *11* (3), 261-264.

60. Martin, Y.; Williams, C. C.; Wickramasinghe, H. K., Atomic force microscope–force mapping and profiling on a sub 100-Å scale. *Journal of Applied Physics* **1987,** *61* (10), 4723-4729.

61. Güthner, P.; Dransfeld, K., Local poling of ferroelectric polymers by scanning force microscopy. *Applied Physics Letters* **1992,** *61* (9), 1137-1139.

62. Zhong, Q.; Inniss, D.; Kjoller, K.; Elings, V. B., Fractured polymer/silica fiber surface studied by tapping mode atomic force microscopy. *Surface Science* **1993,** *290* (1–2), L688-L692.

63. Tseng, A. A.; Notargiacomo, A.; Chen, T. P., Nanofabrication by scanning probe microscope lithography: A review. *Journal of Vacuum Science & Technology B* **2005,** *23* (3), 877-894.

64. Gewirth, A. A.; Niece, B. K., Electrochemical applications of in situ scanning probe microscopy. *Chemical Reviews* **1997,** *97* (4), 1129-1162.

65. Dunn, R. C., Near-field scanning optical microscopy. *Chemical Reviews* **1999,** *99* (10), 2891-2928.

66. Takano, H.; Kenseth, J. R.; Wong, S.-S.; O'Brie, J. C.; Porter, M. D., Chemical and biochemical analysis using scanning force microscopy. *Chemical Reviews* **1999,** *99* (10), 2845-2890.

67. Ascoli, C.; Dinelli, F.; Frediani, C.; Petracchi, D.; Salerno, M.; Labardi, M.; Allegrini, M.; Fuso, F., Normal and lateral forces in scanning force microscopy. *Journal of Vacuum Science & Technology B* **1994,** *12* (3), 1642-1645.

68. Albrecht, T. R.; Quate, C. F., Atomic resolution imaging of a nonconductor by atomic force microscopy. *Journal of Applied Physics* **1987,** *62* (7), 2599-2602.

69. Binnig, G.; Ch, G.; Stoll, E.; Albrecht, T. R.; Quate, C. F., Atomic resolution with atomic force microscope. *EPL (Europhysics Letters)* **1987,** *3* (12), 1281.

70. Marti, O.; Drake, B.; Hansma, P. K., Atomic force microscopy of liquid covered surfaces: Atomic resolution images. *Applied Physics Letters* **1987,** *51* (7), 484-486.

71. Scheuring, S.; Müller, D.; Stahlberg, H.; Engel, H.-A.; Engel, A., Sampling the conformational space of membrane protein surfaces with the AFM. *Eur Biophys J* **2002,** *31* (3), 172-178.

72. Amro, N. A.; Kotra, L. P.; Wadu-Mesthrige, K.; Bulychev, A.; Mobashery, S.; Liu, G.-y., High-resolution atomic force microscopy studies of the escherichia coli outer membrane: Structural basis for permeability. *Langmuir* **2000,** *16* (6), 2789-2796.

73. Weisenhorn, A. L.; Hansma, P. K.; Albrecht, T. R.; Quate, C. F., Forces in atomic force microscopy in air and water. *Applied Physics Letters* **1989,** *54* (26), 2651-2653.

74. Weisenhorn, A. L.; Maivald, P.; Butt, H. J.; Hansma, P. K., Measuring adhesion, attraction, and repulsion between surfaces in liquids with an atomic-force microscope. *Physical Review B* **1992,** *45* (19), 11226-11232.

75. Lyles, V.; Serem, W.; Yu, J.-J.; Garno, J., Surface characterization using atomic force microscopy (afm) in liquid environments. In *Surface Science Techniques*, Bracco, G.; Holst, B., Eds. Springer Berlin Heidelberg: 2013; Vol. 51, pp 599-620.

76. Hansma, H. G.; Sinsheimer, R. L.; Groppe, J.; Bruice, T. C.; Elings, V.; Gurley, G.; Bezanilla, M.; Mastrangelo, I. A.; Hough, P. V. C.; Hansma, P. K., Recent advances in atomic force microscopy of DNA. *Scanning* **1993,** *15* (5), 296-299.

77. Vié, V.; Giocondi, M.-C.; Lesniewska, E.; Finot, E.; Goudonnet, J.-P.; Le Grimellec, C., Tapping-mode atomic force microscopy on intact cells: optimal adjustment of tapping conditions by using the deflection signal. *Ultramicroscopy* **2000,** *82* (1–4), 279-288.

78. Betley, T. A.; Banaszak Holl, M. M.; Orr, B. G.; Swanson, D. R.; Tomalia, D. A.; Baker, J. R., Tapping mode atomic force microscopy investigation of poly(amidoamine) dendrimers: Effects of substrate and ph on dendrimer deformation. *Langmuir* **2001,** *17* (9), 2768-2773.

79. Putman, C. A. J.; Van der Werf, K. O.; De Grooth, B. G.; Van Hulst, N. F.; Greve, J., Tapping mode atomic force microscopy in liquid. *Applied Physics Letters* **1994,** *64* (18), 2454-2456.

80. Kienberger, F.; Stroh, C.; Kada, G.; Moser, R.; Baumgartner, W.; Pastushenko, V.; Rankl, C.; Schmidt, U.; Müller, H.; Orlova, E.; LeGrimellec, C.; Drenckhahn, D.; Blaas, D.; Hinterdorfer, P., Dynamic force microscopy imaging of native membranes. *Ultramicroscopy* **2003,** *97* (1–4), 229-237.

81. Legleiter, J.; Park, M.; Cusick, B.; Kowalewski, T., Scanning probe acceleration microscopy (SPAM) in fluids: Mapping mechanical properties of surfaces at the nanoscale. *Proceedings of the National Academy of Sciences of the United States of America* **2006,** *103* (13), 4813-4818.

82. Tamayo, J.; García, R., Deformation, contact time, and phase contrast in tapping mode scanning force microscopy. *Langmuir* **1996,** *12* (18), 4430-4435.

83. Gotsmann, B.; Seidel, C.; Anczykowski, B.; Fuchs, H., Conservative and dissipative tip-sample interaction forces probed with dynamic AFM. *Physical Review B* **1999,** *60* (15), 11051-11061.

84. Sulchek, T.; Yaralioglu, G. G.; Quate, C. F.; Minne, S. C., Characterization and optimization of scan speed for tapping-mode atomic force microscopy. *Review of Scientific Instruments* **2002,** *73* (8), 2928-2936.

85. Hierlemann, A.; Campbell, J. K.; Baker, L. A.; Crooks, R. M.; Ricco, A. J., Structural distortion of dendrimers on gold surfaces: A tapping-mode afm investigation. *Journal of the American Chemical Society* **1998,** *120* (21), 5323-5324.

86. Raghavan, D.; Gu, X.; Nguyen, T.; VanLandingham, M.; Karim, A., Mapping polymer heterogeneity using atomic force microscopy phase imaging and nanoscale indentation. *Macromolecules* **2000,** *33* (7), 2573-2583.

87. Dong, R.; Yu, L. E., Investigation of surface changes of nanoparticles using tm-afm phase imaging. *Environmental Science & Technology* **2003,** *37* (12), 2813-2819.

88. Aytun, T.; Mutaf, O. F.; el-Atwani, O. J.; Ow-Yang, C. W., Nanoscale composition mapping of segregation in micelles with tapping-mode atomic force microscopy. *Langmuir* **2008,** *24* (24), 14183-14187.

89. Ogoshi, T.; Fujiwara, T.; Bertolucci, M.; Galli, G.; Chiellini, E.; Chujo, Y.; Wynne, K. J., Tapping mode afm evidence for an amorphous reticular phase in a condensation-cured hybrid elastomer: A,ω-dihydroxypoly(dimethylsiloxane)/poly(diethoxysiloxane)/fumed silica nanoparticles. *Journal of the American Chemical Society* **2004,** *126* (39), 12284-12285.

90. Chen, X.; McGurk, S. L.; Davies, M. C.; Roberts, C. J.; Shakesheff, K. M.; Tendler, S. J. B.; Williams, P. M.; Davies, J.; Dawkes, A. C.; Domb, A., Chemical and morphological analysis of surface enrichment in a biodegradable polymer blend by phase-detection imaging atomic force microscopy. *Macromolecules* **1998,** *31* (7), 2278-2283.

91. Stark, M.; Möller, C.; Müller, D. J.; Guckenberger, R., From images to interactions: high-resolution phase imaging in tapping-mode atomic force microscopy. *Biophysical Journal* **2001,** *80* (6), 3009-3018.

92. Li, J.-R.; Lewandowski, B. R.; Xu, S.; Garno, J. C., Detecting the magnetic response of iron oxide capped organosilane nanostructures using magnetic sample modulation and atomic force microscopy. *Analytical Chemistry* **2009,** *81* (12), 4792-4802.

93. Kelley, A. T.; Serem, W. K.; Daniels, S. L.; Englade-Franklin, L. E.; Morrison, G.; Flurry, N.; Chan, J. Y.; Garno, J. C., Vibrational response of feni3 nanoparticles to the flux of a modulated electromagnetic field detected by contact-mode atomic force microscopy. *The Journal of Physical Chemistry C* **2013,** *117* (36), 18768-18776.

94. Daniels, S.; Ngunjiri, J.; Garno, J., Investigation of the magnetic properties of ferritin by AFM imaging with magnetic sample modulation. *Anal Bioanal Chem* **2009,** *394* (1), 215-223.

95. Van Hove, M. A., From surface science to nanotechnology. *Catalysis Today* **2006,** *113* (3–4), 133-140.

96. Whitesides, G.; Mathias, J.; Seto, C., Molecular self-assembly and nanochemistry: a chemical strategy for the synthesis of nanostructures. *Science* **1991,** *254* (5036), 1312-1319.

97. Santos, A.; Deen, M. J.; Marsal, L. F., Low-cost fabrication technologies for nanostructures: state-of-the-art and potential. *Nanotechnology* **2015,** *26* (4), 042001.

98. Ringsdorf, H.; Schlarb, B.; Venzmer, J., Molecular architecture and function of polymeric oriented systems: Models for the study of organization, surface recognition, and dynamics of biomembranes. *Angewandte Chemie International Edition in English* **1988,** *27* (1), 113-158.

99. Douglas, K.; Clark, N. A.; Rothschild, K. J., Biomolecular/solid state nanoheterostructures. *Applied Physics Letters* **1990,** *56* (7), 692-694.

100. Pileni, M. P., Nanosized particles made in colloidal assemblies. *Langmuir* **1997,** *13* (13), 3266-3276.

101. Fasolka, M. J.; Mayes, A. M., Block copolymer thin films: Physics and applications1. *Annual Review of Materials Research* **2001,** *31* (1), 323-355.

102. Krausch, G.; Magerle, R., Nanostructured thin films via self-assembly of block copolymers. *Advanced Materials* **2002,** *14* (21), 1579-1583.

103. Ulman, A., Formation and structure of self-assembled monolayers. *Chemical Reviews* **1996,** *96* (4), 1533-1554.

104. Pires, M. M.; Chmielewski, J., Self-assembly of collagen peptides into microflorettes via metal coordination. *Journal of the American Chemical Society* **2009,** *131* (7), 2706-2712.

105. Morkved, T. L.; Wiltzius, P.; Jaeger, H. M.; Grier, D. G.; Witten, T. A., Mesoscopic self-assembly of gold islands on diblock-copolymer films. *Applied Physics Letters* **1994,** *64* (4), 422-424.

106. Flink, S.; van Veggel, F. C. J. M.; Reinhoudt, D. N., Sensor functionalities in self-assembled monolayers. *Advanced Materials* **2000,** *12* (18), 1315-1328.

107. Finklea, H. O., Self-assembled monolayers on electrodes. In *Encyclopedia of Analytical Chemistry*, John Wiley & Sons, Ltd: 2006.

108. Schreiber, F., Structure and growth of self-assembling monolayers. *Progress in Surface Science* **2000,** *65* (5–8), 151-257.

109. Vericat, C.; Vela, M. E.; Corthey, G.; Pensa, E.; Cortes, E.; Fonticelli, M. H.; Ibanez, F.; Benitez, G. E.; Carro, P.; Salvarezza, R. C., Self-assembled monolayers of thiolates on metals: a review article on sulfur-metal chemistry and surface structures. *RSC Advances* **2014,** *4* (53), 27730-27754.

110. Love, J. C.; Estroff, L. A.; Kriebel, J. K.; Nuzzo, R. G.; Whitesides, G. M., Self-assembled monolayers of thiolates on metals as a form of nanotechnology. *Chemical Reviews* **2005,** *105* (4), 1103-1170.

111. Nuzzo, R. G.; Allara, D. L., Adsorption of bifunctional organic disulfides on gold surfaces. *Journal of the American Chemical Society* **1983,** *105* (13), 4481-4483.

112. Duwez, A.-S., Exploiting electron spectroscopies to probe the structure and organization of self-assembled monolayers: a review. *Journal of Electron Spectroscopy and Related Phenomena* **2004,** *134* (2–3), 97-138.

113. Garno, J. N.; Jayne, C., Afm-based lithography for nanoscale protein assays. *Analytical Chemistry* **2008,** *80* (5), 1361-1369.

114. Garno, J. C.; Zangmeister, C. D.; Batteas, J. D., Directed electroless growth of metal nanostructures on patterned self-assembled monolayers. *Langmuir* **2007,** *23* (14), 7874-7879.

115. Kane, R. S.; Takayama, S.; Ostuni, E.; Ingber, D. E.; Whitesides, G. M., Patterning proteins and cells using soft lithography. *Biomaterials* **1999,** *20* (23–24), 2363-2376.

116. Reed, M. A.; Zhou, C.; Muller, C. J.; Burgin, T. P.; Tour, J. M., Conductance of a molecular junction. *Science* **1997,** *278* (5336), 252-254.

117. Cui, X. D.; Primak, A.; Zarate, X.; Tomfohr, J.; Sankey, O. F.; Moore, A. L.; Moore, T. A.; Gust, D.; Harris, G.; Lindsay, S. M., Reproducible measurement of single-molecule conductivity. *Science* **2001,** *294* (5542), 571-574.

118. Liang, W.; Shores, M. P.; Bockrath, M.; Long, J. R.; Park, H., Kondo resonance in a single-molecule transistor. *Nature* **2002,** *417* (6890), 725-729.

119. Sagiv, J., Organized monolayers by adsorption. 1. Formation and structure of oleophobic mixed monolayers on solid surfaces. *Journal of the American Chemical Society* **1980,** *102* (1), 92-98.

120. Maoz, R.; Sagiv, J., On the formation and structure of self-assembling monolayers. I. A comparative atr-wettability study of Langmuir—Blodgett and adsorbed films on flat substrates and glass microbeads. *Journal of Colloid and Interface Science* **1984,** *100* (2), 465-496.

121. Allara, D. L.; Parikh, A. N.; Rondelez, F., Evidence for a unique chain organization in long chain silane monolayers deposited on two widely different solid substrates. *Langmuir* **1995,** *11* (7), 2357-2360.

122. Hozumi, A.; Yokogawa, Y.; Kameyama, T.; Sugimura, H.; Hayashi, K.; Shirayama, H.; Takai, O., Amino-terminated self-assembled monolayer on a SiO2 surface formed by chemical vapor deposition. *Journal of Vacuum Science & Technology A* **2001,** *19* (4), 1812-1816.

123. Dong, J.; Wang, A.; Ng, K. Y. S.; Mao, G., Self-assembly of octadecyltrichlorosilane monolayers on silicon-based substrates by chemical vapor deposition. *Thin Solid Films* **2006,** *515* (4), 2116-2122.

124. Tripp, C. P.; Hair, M. L., An infrared study of the reaction of octadecyltrichlorosilane with silica. *Langmuir* **1992,** *8* (4), 1120-1126.

125. Wen, K.; Maoz, R.; Cohen, H.; Sagiv, J.; Gibaud, A.; Desert, A.; Ocko, B. M., Postassembly chemical modification of a highly ordered organosilane multilayer: New insights into the structure, bonding, and dynamics of self-assembling silane monolayers. *ACS Nano* **2008,** *2* (3), 579-599.

126. Brzoska, J. B.; Shahidzadeh, N.; Rondelez, F., Evidence of a transition temperature for the optimum deposition of grafted monolayer coatings. *Nature* **1992,** *360* (6406), 719-721.

127. Parikh, A. N.; Allara, D. L.; Azouz, I. B.; Rondelez, F., An intrinsic relationship between molecular structure in self-assembled n-alkylsiloxane monolayers and deposition temperature. *The Journal of Physical Chemistry* **1994,** *98* (31), 7577-7590.

128. McGovern, M. E.; Kallury, K. M. R.; Thompson, M., Role of solvent on the silanization of glass with octadecyltrichlorosilane. *Langmuir* **1994,** *10* (10), 3607-3614.

129. Tripp, C. P.; Hair, M. L., Direct observation of the surface bonds between self-assembled monolayers of octadecyltrichlorosilane and silica surfaces: A low-frequency ir study at the solid/liquid interface. *Langmuir* **1995,** *11* (4), 1215-1219.

130. Tillman, N.; Ulman, A.; Schildkraut, J. S.; Penner, T. L., Incorporation of phenoxy groups in self-assembled monolayers of trichlorosilane derivatives. Effects on film thickness, wettability, and molecular orientation. *Journal of the American Chemical Society* **1988,** *110* (18), 6136-6144.

131. Kim, J. H.; Cotton, T. M.; Uphaus, R. A., Electrochemical and Raman characterization of molecular recognition sites in self-assembled monolayers. *The Journal of Physical Chemistry* **1988,** *92* (20), 5575-5578.

132. Vuillaume, D.; Boulas, C.; Collet, J.; Allan, G.; Delerue, C., Electronic structure of a heterostructure of an alkylsiloxane self-assembled monolayer on silicon. *Physical Review B* **1998,** *58* (24), 16491-16498.

133. Xiao, X.; Hu, J.; Charych, D. H.; Salmeron, M., Chain length dependence of the frictional properties of alkylsilane molecules self-assembled on mica studied by atomic force microscopy. *Langmuir* **1996,** *12* (2), 235-237.

134. Angst, D. L.; Simmons, G. W., Moisture absorption characteristics of organosiloxane self-assembled monolayers. *Langmuir* **1991,** *7* (10), 2236-2242.

135. Li, J.-R.; Garno, J. C., Elucidating the role of surface hydrolysis in preparing organosilane nanostructures via particle lithography. *Nano Letters* **2008,** *8* (7), 1916-1922.

136. Wasserman, S. R.; Tao, Y. T.; Whitesides, G. M., Structure and reactivity of alkylsiloxane monolayers formed by reaction of alkyltrichlorosilanes on silicon substrates. *Langmuir* **1989,** *5* (4), 1074-1087.

137. Trens, P.; Denoyel, R., Adsorption of (γ-aminopropyl)triethoxysilane and related molecules at the silica/heptane interface. *Langmuir* **1996,** *12* (11), 2781-2784.

138. Krasnoslobodtsev, A. V.; Smirnov, S. N., Effect of water on silanization of silica by trimethoxysilanes. *Langmuir* **2002,** *18* (8), 3181-3184.

139. Yu, H.-D.; Regulacio, M. D.; Ye, E.; Han, M.-Y., Chemical routes to top-down nanofabrication. *Chemical Society Reviews* **2013,** *42* (14), 6006-6018.

140. Lu, C.; Lipson, R. H., Interference lithography: a powerful tool for fabricating periodic structures. *Laser & Photonics Reviews* **2010,** *4* (4), 568-580.

141. Altissimo, M., E-beam lithography for micro-/nanofabrication. *Biomicrofluidics* **2010,** *4* (2), 026503.

142. Wang, X.; Xie, S.; Liu, J.; Kucheyev, S. O.; Wang, Y. M., Focused-ion-beam assisted growth, patterning, and narrowing the size distributions of zno nanowires for variable optical properties and enhanced nonmechanical energy conversion. *Chemistry of Materials* **2013,** *25* (14), 2819-2827.

143. Feridun, A.; Kerstin, W.; René, M. d. R.; Markus, P., Focused-ion-beam nanostructuring of Al 2 O 3 dielectric layers for photonic applications. *Journal of Micromechanics and Microengineering* **2012,** *22* (10), 105008.

144. Haynes, C. L.; McFarland, A. D.; Smith, M. T.; Hulteen, J. C.; Van Duyne, R. P., Angle-resolved nanosphere lithography: Manipulation of nanoparticle size, shape, and interparticle spacing. *The Journal of Physical Chemistry B* **2002,** *106* (8), 1898-1902.

145. Xia, Y.; Whitesides, G. M., Soft lithography. *Angewandte Chemie International Edition* **1998,** *37* (5), 550-575.

146. Colson, P.; Henrist, C.; Cloots, R., Nanosphere lithography: A powerful method for the controlled manufacturing of nanomaterials. *Journal of Nanomaterials* **2013,** *2013*, 19.

147. Denis, F. A.; Hanarp, P.; Sutherland, D. S.; Gold, J.; Mustin, C.; Rouxhet, P. G.; Dufrêne, Y. F., Protein adsorption on model surfaces with controlled nanotopography and chemistry. *Langmuir* **2002,** *18* (3), 819-828.

148. Hulteen, J. C.; Van Duyne, R. P., Nanosphere lithography: A materials general fabrication process for periodic particle array surfaces. *Journal of Vacuum Science & Technology A* **1995,** *13* (3), 1553-1558.

149. Deckman, H. W.; Dunsmuir, J. H., Natural lithography. *Applied Physics Letters* **1982,** *41* (4), 377-379.

150. Lewandowski, B. R.; Kelley, A. T.; Singleton, R.; Li, J.-R.; Lowry, M.; Warner, I. M.; Garno, J. C., Nanostructures of cysteine-coated cds nanoparticles produced with "two-particle" lithography. *The Journal of Physical Chemistry C* **2009,** *113* (15), 5933-5940.

151. Batra, D.; Vogt, S.; Laible, P. D.; Firestone, M. A., Self-assembled, mesoporous polymeric networks for patterned protein arrays. *Langmuir* **2005,** *21* (23), 10301-10306.

152. Li, J.-R.; Garno, J. C., Nanostructures of octadecyltrisiloxane self-assembled monolayers produced on au(111) using particle lithography. *ACS Applied Materials & Interfaces* **2009,** *1* (4), 969-976.

153. Lusker, K. L.; Yu, J.-J.; Garno, J. C., Particle lithography with vapor deposition of organosilanes: A molecular toolkit for studying confined surface reactions in nanoscale liquid volumes. *Thin Solid Films* **2011,** *519* (15), 5223-5229.

154. Haynes, C. L.; Van Duyne, R. P., Dichroic optical properties of extended nanostructures fabricated using angle-resolved nanosphere lithography. *Nano Letters* **2003,** *3* (7), 939-943.

155. Haynes, C. L.; Van Duyne, R. P., Nanosphere lithography: A versatile nanofabrication tool for studies of size-dependent nanoparticle optics. *The Journal of Physical Chemistry B* **2001,** *105* (24), 5599-5611.

156. Scheuring, S.; Müller, D.; Stahlberg, H.; Engel, H.-A.; Engel, A., Sampling the conformational space of membrane protein surfaces with the AFM. *Eur. Biophys. J.* **2002,** *31* (3), 172-178.

157. Kenseth, J. R.; Harnisch, J. A.; Jones, V. W.; Porter, M. D., Investigation of approaches for the fabrication of protein patterns by scanning probe lithography. *Langmuir* **2001,** *17* (13), 4105-4112.

158. Muller, D. J.; Fotiadis, D.; Scheuring, S.; Muller, S. A.; Engel, A., Electrostatically balanced subnanometer imaging of biological specimens by atomic force microscope. *Biophys J.* **1999,** *76* (2), 1101-11.

159. Lyubchenko, Y. L.; Shlyakhtenko, L. S., Visualization of supercoiled DNA with atomic force microscopy in situ. *Proc. Natl. Acad. Sci. U. S. A.* **1997,** *94* (2), 496-501.

160. Senden, T. J.; Drummond, C. J., Surface chemistry and tip-sample interactions in atomic force microscopy. *Colloids Surf., A* **1995,** *94* (1), 29-51.

161. Rynders, R. M.; Alkire, R. C., Use of in situ atomic force microscopy to image copper electrodeposits on platinum. *J. Electrochem. Soc.* **1994,** *141* (5), 1166-1173.

162. Lee, Y.; Ding, Z.; Bard, A. J., Combined scanning electrochemical/optical microscopy with shear force and current feedback. *Anal. Chem.* **2002,** *74* (15), 3634-3643.

163. Manne, X.; Hansma, P. K.; Massie, J.; Elings, V. B.; Gewirth, A. A., Atomic-resolution electrochemistry with the atomic force microscope: Copper deposition on gold. *Science* **1991,** *251* (4990), 183-186.

164. Xu, S.; Cruchon-Dupeyrat, S. J. N.; Garno, J. C.; Liu, G.-Y.; Jennings, G. K.; Yong, T.-H.; Laibinis, P. E., In situ studies of thiol self-assembly on gold from solution using atomic force microscopy. *J. Chem. Phys.* **1998,** *108* (12), 5002-5012.

165. Liu, J.-F.; Cruchon-Dupeyrat, S.; Garno, J. C.; Frommer, J.; Liu, G.-Y., Three-dimensional nanostructure construction via nanografting: Positive and negative pattern transfer. *Nano Lett.* **2002,** *2* (9), 937-940.

166. Xu, S.; Liu, G.-y., Nanometer-scale fabrication by simultaneous nanoshaving and molecular self-assembly. *Langmuir* **1997,** *13* (2), 127-129.

167. Seemann, R.; Brinkmann, M.; Kramer, E. J.; Lange, F. F.; Lipowsky, R., Wetting morphologies at microstructured surfaces. *Proc. Natl. Acad. Sci. U. S. A.* **2005,** *102* (6), 1848-1852.

168. Bain, C. D.; Whitesides, G. M., Correlations between wettability and structure in monolayers of alkanethiols adsorbed on gold. *J. Am. Chem. Soc.* **1988,** *110* (11), 3665-3666.

169. Atre, S. V.; Liedberg, B.; Allara, D. L., Chain length dependence of the structure and wetting properties in binary composition monolayers of oh- and ch3-terminated alkanethiolates on gold. *Langmuir* **1995,** *11* (10), 3882-3893.

170. Ulman, A.; Evans, S. D.; Shnidman, Y.; Sharma, R.; Eilers, J. E.; Chang, J. C., Concentration-driven surface transition in the wetting of mixed alkanethiol monolayers on gold. *J. Am. Chem. Soc.* **1991,** *113* (5), 1499-1506.

171. Miranda, P. B.; Pflumio, V.; Saijo, H.; Shen, Y. R., Chain−chain interaction between surfactant monolayers and alkanes or alcohols at solid/liquid interfaces. *J. Am. Chem. Soc.* **1998,** *120* (46), 12092-12099.

172. Weir, M. P.; Parnell, A. J., Water soluble responsive polymer brushes. *Polymers* **2011,** *3*, 2107-2132.

173. Islam, M. R.; Lu, Z.; Li, X.; Sarker, A. K.; Hu, L.; Choi, P.; Li, X.; Hakobyan, N.; Serpe, M. J., Responsive polymers for analytical applications: A review. *Anal. Chim. Acta.* **2013,** *789*, 17-32.

174. Stuart, M. A. C.; Huck, W. T. S.; Genzer, J.; Müller, M.; Ober, C.; Stamm, M.; Sukhorukov, G. B.; Szleifer, I.; Tsukruk, V. V.; Urban, M.; Winnik, F.; Zauscher, S.; Luzinov, I.; Minko, S., Emerging applications of stimuli-responsive polymer materials. *Nat. Mater.* **2010,** *9*, 101-113.

175. Bunsow, J.; Kelby, T. S.; Huck, W. T. S., Polymer brushes: Routes toward mechanosensitive surfaces. *Acc. Chem. Res.* **2010,** *43*, 466-474.

176. Kim, E.; Lee, J.; Kim, D.; Lee, K. E.; Han, S. S.; Lim, N.; Kang, J.; Park, C. G.; Kim, K., Solvent-responsive polymer nanocapsules with controlled permeability: encapsulation and release of a fluorescent dye by swelling and deswelling. *Chem. Commun.* **2009**, 1472-1474.

177. Roiter, Y.; Minko, I.; Nykypanchuk, D.; Tokarev, I.; Minko, S., Mechanism of nanoparticle actuation by responsive polymer brushes: from reconfigurable composite surfaces to plasmonic effects. *Nanoscale* **2012,** *4*, 284-292.

178. Gupta, S.; Agrawal, M.; Uhlmann, P.; Simon, F.; Oertel, U.; Stamm, M., Gold nanoparticles immobilized on stimuli responsive polymer brushes as nanosensors. *Macromol.* **2008,** *41*, 8152-8158.

179. Chen, J.-K.; Zhuang, A.-L., Fabrication of a highly dense line patterned polystyrene brush on silicon surfaces using very large scale integration processing. *J. Phys. Chem. C* **2010,** *114*, 11801-11809.

180. Parnell, A. J.; Martin, S. J.; Jones, R. A. L.; Vasilev, C.; Crook, C. J.; Ryan, A. J., Direct visualization of the real time swelling and collapse of a poly(methacrylic acid) brush using atomic force microscopy. *Soft Matter* **2009,** *5*, 296-299.

181. Alswieleh, A. M.; Cheng, N.; Leggett, G. J.; Armes, S. P., Spatial control over cross-linking dictates the ph-responsive behavior of poly(2-(tert-butylamino)ethyl methacrylate) brushes. *Langmuir* **2014,** *30*, 1391-1400.

182. Ayres, N.; Cyrus, C. D.; Brittain, W. J., Stimuli-responsive surfaces using polyampholyte polymer brushes prepared via atom transfer radical polymerization. *Langmuir* **2007,** *23*, 3744-3749.

183. Wang, M.; Zou, S.; Guerin, G.; Shen, L.; Deng, K.; Jones, M.; Walker, G. C.; Scholes, G. D.; Winnik, M. A., A water-soluble pH-responsive molecular brush of poly(n,n-dimethylaminoethyl methacrylate) grafted polythiophene. *Macromol.* **2008,** *41*, 6993-7002.

184. Xu, C.; Wayland, B. B.; Fryd, M.; Winey, K. I.; Composto, R. J., pH-responsive nanostructures assembled from amphiphilic block copolymers. *Macromol.* **2006,** *39*, 6063-6070.

185. Itano, K.; Choi, J.; Rubner, M. F., Mechanism of the ph-induced discontinuous swelling/deswelling transitions of poly(allylamine hydrochloride)-containing polyelectrolyte multilayer films. *Macromol.* **2005,** *38*, 3450-3460.

186. Nunes, S. P.; Behzad, A. R.; Hooghan, B.; Sougrat, R.; Karunakaran, M.; Pradeep, N.; Vainio, U.; Peinemann, K.-V., Switchable ph-responsive polymeric membranes prepared via block copolymer micelle assembly. *ACS Nano* **2011,** *5*, 3516-3522.

187. Schuwer, N.; Klok, H.-A., Tuning the pH sensitivity of poly(methacrylic acid) brushes. *Langmuir* **2011,** *27*, 4789-4796.

188. Bittrich, E.; Kuntzsch, M.; Eichhorn, K.-J.; Uhlmann, P., Complex ph- and temperature-sensitive swelling behavior of mixed polymer brushes. *J Polym. Sci. B* **2010,** *48*, 1606-1615.

189. Zhang, L.; Wang, H., Photografted poly(acrylic acid) thin layers with ultra-high swelling ratios and high swelling and pH response rates. *Polymer* **2011,** *52*, 3146-3154.

190. Beaussart, A.; Ngo, T. C.; Derclaye, S.; Kalinova, R.; Mincheva, R.; Dubois, P.; Leclere, P.; Dufrene, Y. F., Chemical force microscopy of stimuli-responsive adhesive copolymers. *Nanoscale* **2014,** *6*, 565-571.

191. Yim, H.; Kent, M. S.; Hall, J. S.; Benkoski, J. J.; Kramer, E. J., Probing the structure of organosilane films by solvent swelling and neutron and x-ray reflection. *J. Phys. Chem. B* **2002,** *106* (10), 2474-2481.

192. Lee, J.; Orazbayev, A.; Govorov, A. O.; Kotov, N. A., Solvent effect in dynamic superstructures from au nanoparticles and cdte nanowires: Experimental observation and theoretical description. *J. Phys. Chem. C* **2010,** *114*, 1404-1410.

193. (a) Li, J.-R.; Garno, J. C., Elucidating the Role of Surface Hydrolysis in Preparing Organosilane Nanostructures via Particle Lithography. *Nano Lett.* **2008,** *8* (7), 1916-1922; (b) Li, J.-R.; Lusker, K. L.; Yu, J.-J.; Garno, J. C., Engineering the spatial selectivity of surfaces at the nanoscale using particle lithography combined with vapor deposition of organosilanes. *ACS Nano* **2009,** *3* (7), 2023-2035.

194. Nečas, D.; Klapetek, P., Gwyddion: an open-source software for SPM data analysis. *centr.eur.j.phys.* **2012,** *10* (1), 181-188.

195. Jeon, N. L.; Finnie, K.; Branshaw, K.; Nuzzo, R. G., Structure and stability of patterned self-assembled films of octadecyltrichlorosilane formed by contact printing. *Langmuir* **1997,** *13* (13), 3382-3391.

196. Tillman, N.; Ulman, A.; Schildkraut, J. S.; Penner, T. L., Incorporation of phenoxy groups in self-assembled monolayers of trichlorosilane derivatives. Effects on film thickness, wettability, and molecular orientation. *J. Am. Chem. Soc.* **1988,** *110* (18), 6136-6144.

197. Vallant, T.; Brunner, H.; Mayer, U.; Hoffmann, H.; Leitner, T.; Resch, R.; Friedbacher, G., Formation of self-assembled octadecylsiloxane monolayers on mica and silicon surfaces studied by atomic force microscopy and infrared spectroscopy. *J. Phys. Chem. B* **1998,** *102* (37), 7190-7197.

198. Calistri-Yeh, M.; Kramer, E. J.; Sharma, R.; Zhao, W.; Rafailovich, M. H.; Sokolov, J.; Brock, J. D., Thermal stability of self-assembled monolayers from alkylchlorosilanes. *Langmuir* **1996,** *12* (11), 2747-2755.

199. Kim, H. K.; Lee, J. P.; Park, C. R.; Kwak, H. T.; Sung, M. M., Thermal decomposition of alkylsiloxane self-assembled monolayers in air. *J. Phys. Chem. B* **2003,** *107* (18), 4348-4351.

200. Cohen, S. R.; Naaman, R.; Sagiv, J., Thermally induced disorder in organized organic monolayers on solid substrates. *J. Phys. Chem.* **1986,** *90* (14), 3054-3056.

201. Chen, Y. L.; Xu, Z.; Israelachvili, J., Structure and interactions of surfactant-covered surfaces in nonaqueous (oil-surfactant-water) media. *Langmuir* **1992,** *8* (12), 2966-2975.

202. Martın, J.; Nogues, J.; Liu, K.; Vicent, J.; Schuller, I. K., Ordered magnetic nanostructures: fabrication and properties. *Journal of magnetism and magnetic materials* **2003,** *256* (1), 449-501.

203. Terris, B. D.; Thomson, T., Nanofabricated and self-assembled magnetic structures as data storage media. *Journal of Physics D: Applied Physics* **2005,** *38* (12), R199.

204. Sun, S.; Murray, C. B.; Weller, D.; Folks, L.; Moser, A., Monodisperse FePt nanoparticles and ferromagnetic FePt nanocrystal superlattices. *Science* **2000,** *287* (5460), 1989-1992.

205. Yu, B.; Meyyappan, M., Nanotechnology: Role in emerging nanoelectronics. *Solid-State Electronics* **2006,** *50* (4), 536-544.

206. Shipway, A. N.; Katz, E.; Willner, I., Nanoparticle arrays on surfaces for electronic, optical, and sensor applications. *ChemPhysChem* **2000,** *1* (1), 18-52.

207. Bedanta, S.; Barman, A.; Kleemann, W.; Petracic, O.; Seki, T., Magnetic nanoparticles: A subject for both fundamental research and applications. *Journal of Nanomaterials* **2013,** *2013*, 22.

208. Mørup, S., Superferromagnetic nanostructures. *Hyperfine Interact* **1994,** *90* (1), 171-185.

209. Gao, J.; Gu, H.; Xu, B., Multifunctional magnetic nanoparticles: Design, synthesis, and biomedical applications. *Accounts of Chemical Research* **2009,** *42* (8), 1097-1107.

210. Gupta, A. K.; Gupta, M., Synthesis and surface engineering of iron oxide nanoparticles for biomedical applications. *Biomaterials* **2005,** *26* (18), 3995-4021.

211. Jun, Y.-w.; Seo, J.-w.; Cheon, J., Nanoscaling laws of magnetic nanoparticles and their applicabilities in biomedical sciences. *Accounts of Chemical Research* **2008,** *41* (2), 179-189.

212. Pedro, T.; María del Puerto, M.; Sabino, V.-V.; Teresita, G.-C.; Carlos, J. S., The preparation of magnetic nanoparticles for applications in biomedicine. *Journal of Physics D: Applied Physics* **2003,** *36* (13), R182.

213. Banerjee, R.; Katsenovich, Y.; Lagos, L.; McIintosh, M.; Zhang, X.; Li, C. Z., Nanomedicine: Magnetic nanoparticles and their biomedical applications. *Current Medicinal Chemistry* **2010,** *17* (27), 3120-3141.

214. Laurent, S.; Forge, D.; Port, M.; Roch, A.; Robic, C.; Vander Elst, L.; Muller, R. N., Magnetic iron oxide nanoparticles: Synthesis, stabilization, vectorization, physicochemical characterizations, and biological applications. *Chemical Reviews* **2008,** *108* (6), 2064-2110.

215. Catherine, C. B.; Adam, S. G. C., Functionalisation of magnetic nanoparticles for applications in biomedicine. *Journal of Physics D: Applied Physics* **2003,** *36* (13), R198.

216. Kinge, S.; Crego-Calama, M.; Reinhoudt, D. N., Self-assembling nanoparticles at surfaces and interfaces. *ChemPhysChem* **2008,** *9* (1), 20-42.

217. Martín, J. I.; Nogués, J.; Liu, K.; Vicent, J. L.; Schuller, I. K., Ordered magnetic nanostructures: fabrication and properties. *Journal of Magnetism and Magnetic Materials* **2003,** *256* (1–3), 449-501.

218. Hao, E.; Lian, T., Layer-by-layer assembly of cdse nanoparticles based on hydrogen bonding. *Langmuir* **2000,** *16* (21), 7879-7881.

219. Lu, C.; Wu, N.; Jiao, X.; Luo, C.; Cao, W., Micropatterns constructed from Au nanoparticles. *Chemical Communications* **2003,** (9), 1056-1057.

220. Disch, S.; Wetterskog, E.; Hermann, R. P.; Salazar-Alvarez, G.; Busch, P.; Brückel, T.; Bergström, L.; Kamali, S., Shape induced symmetry in self-assembled mesocrystals of iron oxide nanocubes. *Nano Letters* **2011,** *11* (4), 1651-1656.

221. Binder, W. H., Supramolecular assembly of nanoparticles at liquid–liquid interfaces. *Angewandte Chemie International Edition* **2005,** *44* (33), 5172-5175.

222. Binns, C.; Trohidou, K. N.; Bansmann, J.; Baker, S. H.; Blackman, J. A.; Bucher, J. P.; Kechrakos, D.; Kleibert, A.; Louch, S.; Meiwes-Broer, K. H.; Pastor, G. M.; Perez, A.; Xie, Y., The behaviour of nanostructured magnetic materials produced by depositing gas-phase nanoparticles. *Journal of Physics D: Applied Physics* **2005,** *38* (22), R357.

223. Grigoriev, D.; Gorin, D.; Sukhorukov, G. B.; Yashchenok, A.; Maltseva, E.; Möhwald, H., Polyelectrolyte/magnetite nanoparticle multilayers: Preparation and structure characterization. *Langmuir* **2007,** *23* (24), 12388-12396.

224. Pauly, M.; Pichon, B. P.; Albouy, P.-A.; Fleutot, S.; Leuvrey, C.; Trassin, M.; Gallani, J.-L.; Begin-Colin, S., Monolayer and multilayer assemblies of spherically and cubic-shaped iron oxide nanoparticles. *Journal of Materials Chemistry* **2011,** *21* (40), 16018-16027.

225. Mammeri, F.; Bras, Y. L.; Daou, T. J.; Gallani, J.-L.; Colis, S.; Pourroy, G.; Donnio, B.; Guillon, D.; Bégin-Colin, S., Formation of ferrimagnetic films with functionalized magnetite nanoparticles using the langmuir−blodgett technique. *The Journal of Physical Chemistry B* **2009,** *113* (3), 734-738.

226. Liu, C.; Shan, Y.; Zhu, Y.; Chen, K., Magnetic monolayer film of oleic acid-stabilized Fe3O4 particles fabricated via Langmuir-Blodgett technique. *Thin Solid Films* **2009,** *518* (1), 324-327.

227. Palacin, S.; Hidber, P. C.; Bourgoin, J.-P.; Miramond, C.; Fermon, C.; Whitesides, G. M., Patterning with magnetic materials at the micron scale. *Chemistry of Materials* **1996,** *8* (6), 1316-1325.

228. Dong, A.; Chen, J.; Vora, P. M.; Kikkawa, J. M.; Murray, C. B., Binary nanocrystal superlattice membranes self-assembled at the liquid-air interface. *Nature* **2010,** *466* (7305), 474-477.

229. Yellen, B. B.; Friedman, G., Programmable assembly of colloidal particles using magnetic microwell templates. *Langmuir* **2004,** *20* (7), 2553-2559.

230. Snezhko, A.; Aranson, I. S., Magnetic manipulation of self-assembled colloidal asters. *Nat Mater* **2011,** *10* (9), 698-703.

231. Mirica, K. A.; Ilievski, F.; Ellerbee, A. K.; Shevkoplyas, S. S.; Whitesides, G. M., Using magnetic levitation for three dimensional self-assembly. *Advanced Materials* **2011,** *23* (36), 4134-4140.

232. Joseph, A.; Mathew, S., Ferrofluids: Synthetic strategies, stabilization, physicochemical features, characterization, and applications. *ChemPlusChem* **2014,** *79* (10), 1382-1420.

233. Chou, S. Y.; Wei, M.; Krauss, P. R.; Fischer, P. B., Study of nanoscale magnetic structures fabricated using electron beam lithography and quantum magnetic disk. *Journal of Vacuum Science & Technology B* **1994,** *12* (6), 3695-3698.

234. O'Barr, R.; Lederman, M.; Schultz, S.; Xu, W.; Scherer, A.; Tonucci, R. J., Preparation and quantitative magnetic studies of single-domain nickel cylinders. *Journal of Applied Physics* **1996,** *79* (8), 5303-5305.

235. Rousseaux, F.; Decanini, D.; Carcenac, F.; Cambril, E.; Ravet, M. F.; Chappert, C.; Bardou, N.; Bartenlian, B.; Veillet, P., Study of large area high density magnetic dot arrays fabricated using synchrotron radiation based x-ray lithography. *Journal of Vacuum Science & Technology B* **1995,** *13* (6), 2787-2791.

236. Thielen, M.; Kirsch, S.; Weinforth, H.; Carl, A.; Wassermann, E. F., Magnetization reversal in nanostructured Co/Pt multilayer dots and films. *Magnetics, IEEE Transactions on* **1998,** *34* (4), 1009-1011.

237. Ross, C. A.; Smith, H. I.; Savas, T.; Schattenburg, M.; Farhoud, M.; Hwang, M.; Walsh, M.; Abraham, M. C.; Ram, R. J., Fabrication of patterned media for high density magnetic storage. *Journal of Vacuum Science & Technology B* **1999,** *17* (6), 3168-3176.

238. Garno, J. C.; Yang, Y.; Amro, N. A.; Cruchon-Dupeyrat, S.; Chen, S.; Liu, G.-Y., Precise positioning of nanoparticles on surfaces using scanning probe lithography. *Nano Letters* **2003,** *3* (3), 389-395.

239. Fu, L.; Liu, X.; Zhang, Y.; Dravid, V. P.; Mirkin, C. A., Nanopatterning of "hard" magnetic nanostructures via dip-pen nanolithography and a sol-based ink. *Nano Letters* **2003,** *3* (6), 757-760.

240. Choi, D.-G.; Yu, H. K.; Jang, S. G.; Yang, S.-M., Arrays of binary and ternary particles and their replica pores on patterned microchannels. *Chemistry of Materials* **2003,** *15* (22), 4169-4171.

241. Sun, Z.; Li, Y.; Wang, Y.; Chen, X.; Zhang, J.; Zhang, K.; Wang, Z.; Bao, C.; Zeng, J.; Zhao, B.; Yang, B., Three-dimensional colloidal crystal-assisted lithography for two-dimensional patterned arrays. *Langmuir* **2007,** *23* (21), 10725-10731.

242. Cai, Y.; Ocko, B. M., Large-scale fabrication of protein nanoarrays based on nanosphere lithography. *Langmuir* **2005,** *21* (20), 9274-9279.

243. Englade-Franklin, L. E.; Saner, C. K.; Garno, J. C., Spatially selective surface platforms for binding fibrinogen prepared by particle lithography with organosilanes. *Interface Focus* **2013,** *3* (3).

244. Sun, F.; Cai, W.; Li, Y.; Duan, G.; Nichols, W. T.; Liang, C.; Koshizaki, N.; Fang, Q.; Boyd, I. W., Laser morphological manipulation of gold nanoparticles periodically arranged on solid supports. *Appl. Phys. B* **2005,** *81* (6), 765-768.

245. Tan, B. J. Y.; Sow, C. H.; Koh, T. S.; Chin, K. C.; Wee, A. T. S.; Ong, C. K., Fabrication of size-tunable gold nanoparticles array with nanosphere lithography, reactive ion etching, and thermal annealing. *The Journal of Physical Chemistry B* **2005,** *109* (22), 11100-11109.

246. Weekes, S. M.; Ogrin, F. Y.; Murray, W. A.; Keatley, P. S., Macroscopic arrays of magnetic nanostructures from self-assembled nanosphere templates. *Langmuir* **2007,** *23* (3), 1057-1060.

247. Weekes, S. M.; Ogrin, F. Y.; Murray, W. A., Fabrication of large-area ferromagnetic arrays using etched nanosphere lithography. *Langmuir* **2004,** *20* (25), 11208-11212.

248. Rybczynski, J.; Ebels, U.; Giersig, M., Large-scale, 2D arrays of magnetic nanoparticles. *Colloids and Surfaces A: Physicochemical and Engineering Aspects* **2003,** *219* (1–3), 1-6.

249. Zheng, Y. B.; Chua, S. J.; Huan, C. H. A.; Miao, Z. L., Selective growth of GaAs quantum dots on the triangle nanocavities bounded by SiO2 mask on Si substrate by MBE. *Journal of Crystal Growth* **2004,** *268* (3–4), 369-374.

250. Chen, J.; Liao, W.-S.; Chen, X.; Yang, T.; Wark, S. E.; Son, D. H.; Batteas, J. D.; Cremer, P. S., Evaporation-induced assembly of quantum dots into nanorings. *ACS Nano* **2009,** *3* (1), 173-180.

251. Saner, C. K.; Lusker, K. L.; LeJeune, Z. M.; Serem, W. K.; Garno, J. C., Self-assembly of octadecyltrichlorosilane: Surface structures formed using different protocols of particle lithography. *Beilstein Journal of Nanotechnology* **2012,** *3*, 114-122.

252. Geissler, M.; McLellan, J. M.; Chen, J.; Xia, Y., Side-by-side patterning of multiple alkanethiolate monolayers on gold by edge-spreading lithography. *Angewandte Chemie International Edition* **2005,** *44* (23), 3596-3600.

253. Deng, H.; Li, X.; Peng, Q.; Wang, X.; Chen, J.; Li, Y., Monodisperse magnetic single-crystal ferrite microspheres. *Angewandte Chemie International Edition* **2005,** *44* (18), 2782-2785.

APPENDIX A: LETTER OF PERMISSION

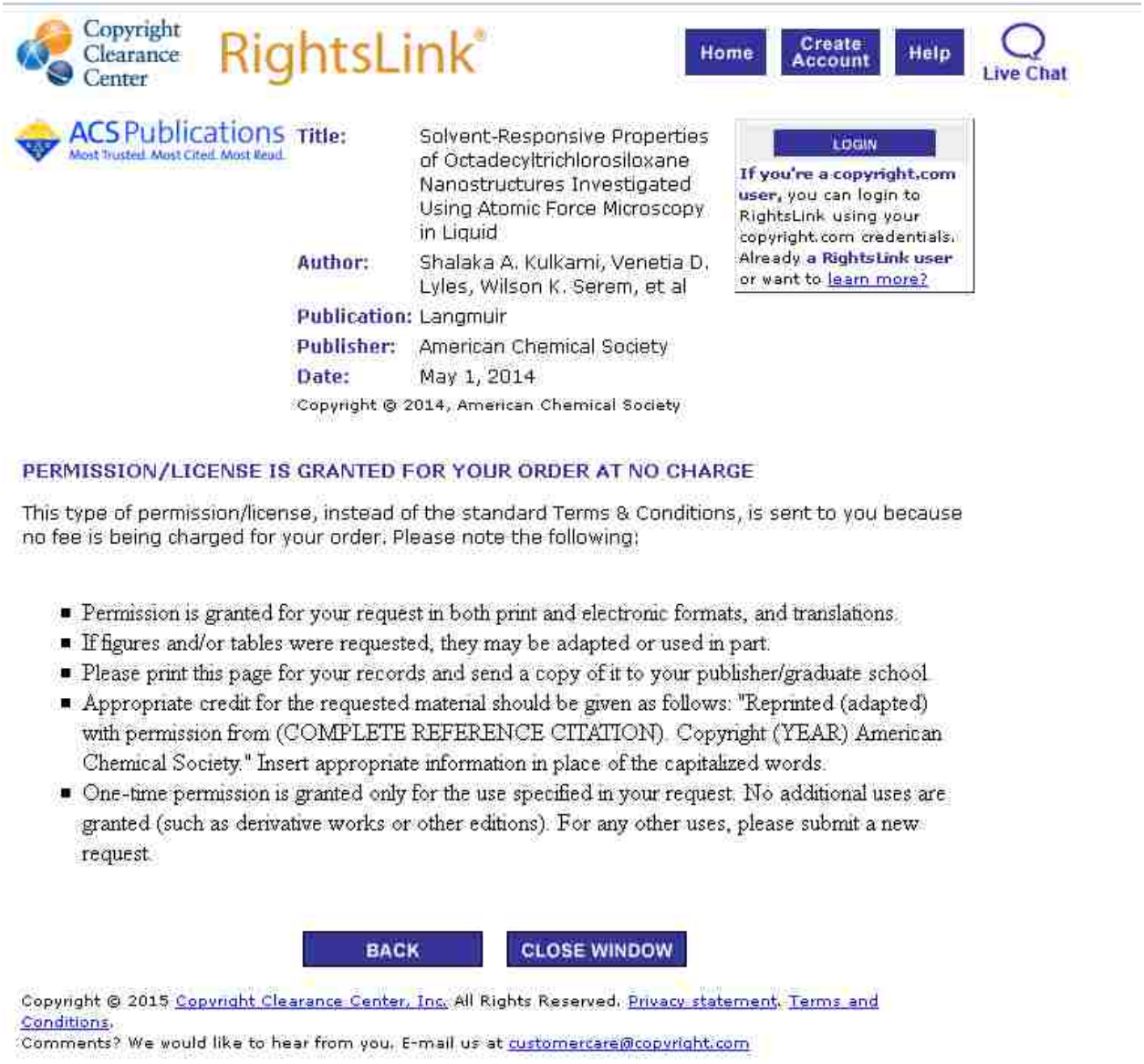

Copyright Clearance Center RightsLink®

Home | Create Account | Help | Live Chat

ACS Publications
Most Trusted. Most Cited. Most Read.

Title: Solvent-Responsive Properties of Octadecyltrichlorosiloxane Nanostructures Investigated Using Atomic Force Microscopy in Liquid

Author: Shalaka A. Kulkarni, Venetia D. Lyles, Wilson K. Serem, et al

Publication: Langmuir

Publisher: American Chemical Society

Date: May 1, 2014

Copyright © 2014, American Chemical Society

LOGIN

If you're a copyright.com user, you can login to RightsLink using your copyright.com credentials. Already a **RightsLink user** or want to learn more?

PERMISSION/LICENSE IS GRANTED FOR YOUR ORDER AT NO CHARGE

This type of permission/license, instead of the standard Terms & Conditions, is sent to you because no fee is being charged for your order. Please note the following:

- Permission is granted for your request in both print and electronic formats, and translations.
- If figures and/or tables were requested, they may be adapted or used in part.
- Please print this page for your records and send a copy of it to your publisher/graduate school.
- Appropriate credit for the requested material should be given as follows: "Reprinted (adapted) with permission from (COMPLETE REFERENCE CITATION). Copyright (YEAR) American Chemical Society." Insert appropriate information in place of the capitalized words.
- One-time permission is granted only for the use specified in your request. No additional uses are granted (such as derivative works or other editions). For any other uses, please submit a new request.

BACK | CLOSE WINDOW

Copyright © 2015 Copyright Clearance Center, Inc. All Rights Reserved. Privacy statement. Terms and Conditions.
Comments? We would like to hear from you. E-mail us at customercare@copyright.com

APPENDIX B: SUPPLEMENTAL INFORMATION FOR SOLVENT-RESPONSIVE PROPERTIES OF OCTADECYLTRICHLOROSILOXANE NANOSTRUCTURES INVESTIGATED USING ATOMIC FORCE MICROSCOPY IN LIQUID

Supporting Information is provided with AFM images for a control experiment with a sample prepared using a surface mask of 300 nm diameter mesospheres (Figure B1).

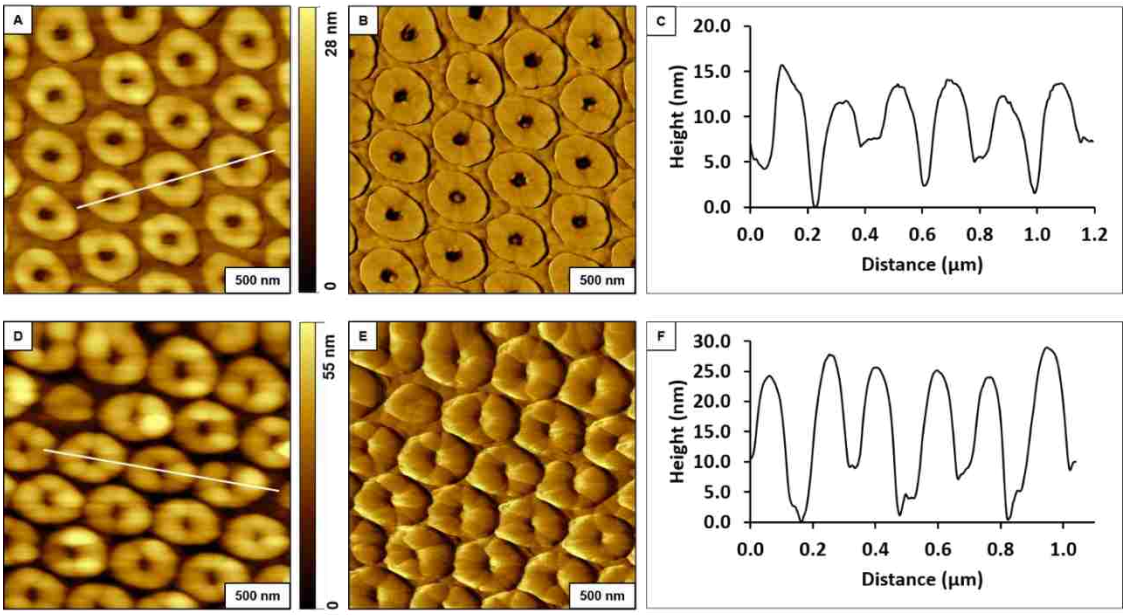

Figure B.1 Side-by-side comparison of OTS nanostructures prepared with 300 nm latex spheres imaged in air (top row) and with immersion in liquid media (bottom row). (A) Zoom-in topography frame; (B) simultaneously-acquired lateral force image; (C) Height profile for the white line shown in A. (D) Zoom in topography frame of the same sample subsequently acquired in ethanol using the same AFM probe; (E) corresponding lateral force image; (F) Line profile for white line shown in D.

Calculations for estimated changes in the nanopattern volume in ethanol are provided in Figure B2

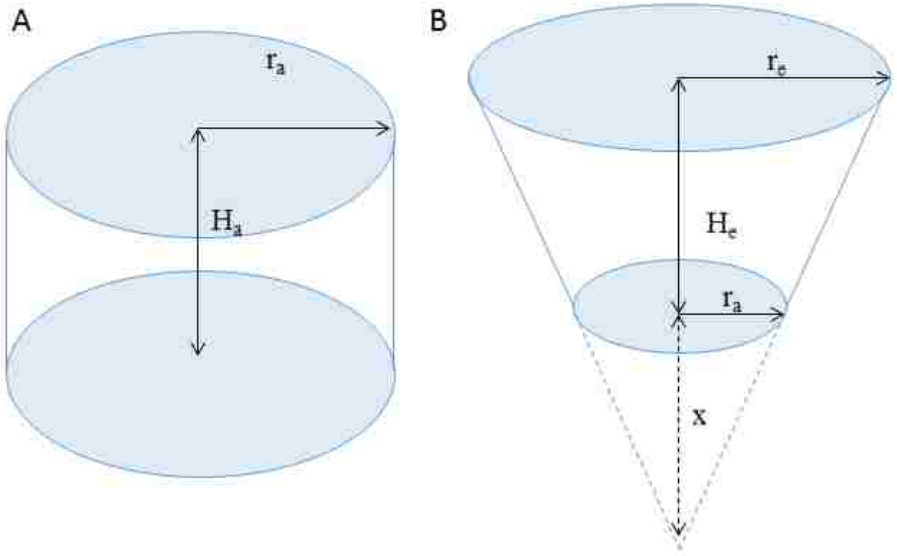

Figure B.2. (A) Representation of an OTS nanoring for a sample dried in air; (B) Representation of the 3D volume of the swelling of a nanoring in a sample exposed to ethanol.

Calculation of percent change in volume for OTS ring nanostructures

Each nanoring in the sample exposed to air can be described as a cylinder of radius r_a and height H_a (see Figure A2.A). The volume of this cylinder is given by $\rho r_a^2 H_a$

In the case of the nanoring exposed to ethanol, the base attached to the substrate remains the same but the top expands. If $2r_e$ is the width of the top layer and H_e the height, we can approximate this to a section of a right circular cone of radius r_e and height H_e+x, from which a right circular cone of radius r_a and height x has been subtracted (see Figure A2.B). We can obtain x by solving the following equation:

$$\frac{H_e + x}{r_e} = \frac{x}{r_a}$$

The total volume of the nanoring is then given by: $\frac{1}{3}\rho[r_e^2(H_e + x) - r_a^2 x]$

The percent increase in volume attributed to ring swelling:

Percent increase (%) = $\frac{volume\ of\ nanoring\ in\ ethanol - volume\ of\ nanoring\ in\ air}{volume\ of\ nanoring\ in\ air}$ x 100

Table B1 Calculation of percent change in volume for OTS ring nanostructures

Sample Description	**Volume increase in liquid (%)**
Freshly prepared OTS nanorings	730
Sample after annealing	240
Annealed sample after longer immersion in ethanol	246

VITA

Shalaka Amit Kulkarni was born in Mumbai, India, and was raised in the loving and caring family. Her interest in chemistry grew from her first undergrad chemistry lecture of Professor Pandit. She received her bachelor's degree in chemistry from University of Mumbai in 1999, followed by the master's degree in 2001. Upon graduation, she worked as a high school teacher in one of the largest public school systems in India. In the summer of 2011, she began doctoral studies at Louisiana State University under the guidance of Dr. Jayne C. Garno. Thus far at LSU, Shalaka has published a first author publication with three additional first author manuscripts in preparation. Shalaka presented her original research at both regional and national conferences. Shalaka has been a mentor for one undergraduate student. Shalaka has taught undergraduate laboratories at LSU for nine semesters. The degree of Doctor of Philosophy will be conferred at the Fall 2015 Commencement, Louisiana State University, Baton Rouge, LA.